

Ratio of Pion Kaon Production in Proton Carbon Interactions

A dissertation presented

by

Andrey V Lebedev

to

The Department of Physics

in partial fulfillment of the requirements

for the degree of

Doctor of Philosophy

in the subject of

Physics

Harvard University

Cambridge, Massachusetts

May 2007

©2007 - Andrey V Lebedev

All rights reserved.

Thesis advisor
Gary Feldman

Author
Andrey V Lebedev

Ratio of Pion Kaon Production in Proton Carbon Interactions

Abstract

The ratio of pion kaon production by 120 GeV/ c protons incident on carbon target is presented. The data was recorded with the Main Injector Particle Production experiment at Fermi National Accelerator Laboratory. Production ratios of K^+/π^+ , K^-/π^- , K^-/K^+ , and π^-/π^+ are measured in 24 bins in longitudinal momentum from 20 to 90 GeV/ c and transverse momentum up to 2 GeV/ c . The measurement is compared to existing data sets, particle production Monte Carlo results from FLUKA-06, parametrization of proton-beryllium data at 400/450 GeV/ c , and ratios measured by the MINOS experiment on the NuMI target.

Contents

Title Page	i
Abstract	iii
Table of Contents	iv
List of Figures	vi
List of Tables	ix
Acknowledgments	x
Dedication	xi
1 Introduction	1
2 MIPP Detectors	5
2.1 Tracking	5
2.2 Particle Identification	10
2.3 Analysis Magnets	16
3 MIPP Trigger	18
3.1 Particle Identification	18
3.2 Beam Cherenkov Operation	19
3.3 Interaction Trigger	21
3.4 End of Spill and Calibration Triggers	23
3.5 Veto Counter	24
3.6 NuMI Trigger	24
4 Data Acquisition System	26
4.1 VME and CAMAC Interfaces	28
4.2 Online Software	31
4.3 Slow Controls	37
5 Beamline	39
5.1 Accelerator	39
5.2 Primary Beam	41
5.3 Secondary Beam	41

6	Event Reconstruction	48
6.1	Track Fitting	48
6.2	Wire Chambers	52
6.3	Time Projection Chamber	56
6.4	Global Tracking	57
6.5	Vertex Reconstruction	60
6.6	Particle Identification	66
7	Detector Calibration and Alignment	76
7.1	Event Time	76
7.2	Drift Chamber Time Offsets	82
7.3	Chamber Alignment	83
7.4	Tuning the Magnetic Field	88
7.5	TPC Electron Drift	92
7.6	RICH R_0	102
8	Monte Carlo Simulation	104
8.1	Time Projection Chamber Digitization	104
8.2	Wire Chamber Digitization	106
8.3	RICH Hits and Digits	107
9	Data Analysis	108
9.1	Data Binning	108
9.2	Pileup Removal	110
9.3	Primary Vertex Selection	114
9.4	Interaction Trigger Efficiency	117
9.5	Particle ID Variable	118
9.6	Corrections from Monte Carlo Simulation	123
9.7	Corrections and Errors	129
10	Results	134
10.1	Production Ratios	134
10.2	Comparison to Existing Data	134
10.3	Comparison to MINOS Measurements	142
10.4	Discussion and Outlook	144
	Bibliography	145

List of Figures

1.1	Summary of hadronic production data available in 2001	2
1.2	Uncertainties in neutrino flux prediction	3
1.3	MINOS neutrino flux from kaon decays	3
2.1	Schematic of the MIPP spectrometer	6
2.2	Schematic view of the TPC volume and pad plane	9
2.3	Schematic of T00 and T01 construction	12
2.4	Schematic of RICH electronics setup.	15
2.5	Projections of the JGG field map	17
2.6	Projections of the the Rosie field map	17
3.1	Time of flight of beam particles between the T00 and T01 counters	20
3.2	Summary of the upstream beam Cherenkov pressure curves with nitrogen .	21
3.3	Trigger particle tag purity as measured by the RICH	22
3.4	NuMI trigger logic	24
4.1	Schematic of data acquisition setup	27
5.1	Schematic of the FNAL accelerator complex	40
5.2	Analysis of the initial beamline setup	43
5.3	Simulation of tracking of particles through initial beamline setup	44
5.4	Solution for reversed beamline setup	46
5.5	Simulation of tracking of particles using reversed-beam solution	47
6.1	Sketch of wire plane geometry.	49
6.2	Matching of DC123 and DC4/PWC56 segments in the center of Rosie	56
6.3	χ^2 per degree of freedom and number of clusters in chamber track candidates	57
6.4	Selection of tracks for the TMiniut fitter and the resulting track momenta .	58
6.5	Matching of TPC tracks to chamber track candidates	60
6.6	Matching of tracks at the six chambers	61
6.7	Deterministic annealing filter weight functions for the vertex finder	62
6.8	Number of z scans required for a vertex constrained fit	64
6.9	Vertex resolution in z	66
6.10	Mean RICH ring radii and RMS of light distribution	68

6.11	CO ₂ refractive index and Hamamatsu PMT efficiency	68
6.12	Effect of signal region on RICH ring fits	70
6.13	Fitted RICH ring center shift from prediction	71
6.14	Ripples in RICH ring radius	72
6.15	Dependence of amplitude of RICH ring radius ripples	73
6.16	Improvement in RICH radius width from ripple correction	74
6.17	Distribution of fitted RICH ring radii and computed mass squared	75
7.1	Time of flight for particles from the target to the TOF wall	77
7.2	Cable delay drift in T0 counters	78
7.3	Time slewing due to charge on the T0 PMTs	80
7.4	T0 time resolution with and without time slewing correction	81
7.5	Chamber residuals before alignment	84
7.6	Chamber residuals after alignment	85
7.7	DC123 z -alignment results	86
7.8	DC123 alignment results with corrected DC3 angle	87
7.9	Dependence of DC123 alignment constants on beam momentum	89
7.10	Dependence of the DC4 and PWC56 alignment constants on beam momentum	90
7.11	B_x/B_z rotation using chambers	91
7.12	Ratios of B_x/B_y and B_z/B_y in the magnets	92
7.13	Alignment summary versus run after corrections	93
7.14	Alignment summary versus beam momentum after corrections	94
7.15	Dependence of TPC x -residual versus z slope on B_x/B_z rotation	95
7.16	B_x/B_z ratio in the magnets before and after correction	96
7.17	P10 drift velocity measurements	97
7.18	Measured TPC trigger time offset versus run number	98
7.19	Measured TPC drift velocity versus run number	99
7.20	Projections of 120 GeV/ c track hits	101
7.21	The angle between the vertical and horizontal field component in the JGG	102
7.22	RICH ring radius dependence on CO ₂ density	103
9.1	RICH geometric acceptance	109
9.2	Charged hadron fluxes simulated by FLUKA-06	109
9.3	Expected number of π^+ in bins selected for measurement	112
9.4	Momentum and dE/dx in the TPC of uninteracted protons	113
9.5	Distribution of variables used to remove pileup	115
9.6	Distribution of secondary track times on pileup events	116
9.7	Effect of pileup cuts on the TPC dE/dx and the hadron calorimeter energy	116
9.8	Vertex z of 2% carbon and target-out data	117
9.9	Interaction trigger efficiency	118
9.10	Momentum spectrum enhancement due to interaction trigger inefficiency	119
9.11	Computed mass squared versus p_z in different p_t bins	120
9.12	Computed Monte Carlo mass squared versus p_z in different p_t bins	121
9.13	Data-Monte Carlo comparison of particle ID variable α for positives	124
9.14	Data – Monte Carlo comparison of particle ID variable α for negatives	125

9.15	Monte Carlo signal and background in bin (0, 0)	126
9.16	Occupancy of positive pions and kaons in Monte Carlo	127
9.17	Occupancy of negative pions and kaons in Monte Carlo	128
9.18	Reconstructed Monte Carlo to true Monte Carlo comparison	129
9.19	Effect on the ratios from interaction trigger efficiency	130
9.20	Effect on the ratio from 5% change in target out scale factor	131
9.21	Data/Monte Carlo background ratio	132
9.22	Systematic error from background subtraction	133
10.1	Measured ratios versus FLUKA-06 prediction	135
10.2	Comparison to existing measurements	140
10.3	Comparison to existing measurements	141
10.4	Comparison of the ratios on the NuMI target and the 2% target	142
10.5	Comparison to Monte Carlo models and MINOS fitted ratios	143

List of Tables

2.1	Summary of multi-wire chamber parameters	7
2.2	Summary of chamber operation conditions	7
4.1	Message classes implemented in run control.	32
9.1	(p_z, p_T) bins selected for ratio measurement	111
9.2	Trigger efficiency using beryllium and carbon data	119
9.3	Coefficients for conversion from m^2 into particle ID variable α	122
10.1	π^-/π^+ production ratio and errors	136
10.2	K^-/K^+ production ratio and errors	137
10.3	K^+/π^+ production ratio and errors	138
10.4	K^-/π^- production ratio and errors	139

Acknowledgments

This work was made possible thanks to a large number of people. Particularly, I am indebted to my parents for educational and inspirational support in the course of my entire life.

Thanks to Mark Messier I got into the MIPP experiment, and without Mark as an exceptional resource of energy and motivation I would not have found the way out. Thanks to my adviser, Gary Feldman, I had the freedom to choose what I wanted to do. At times, this freedom of action translated into too much responsibility, but it enabled me to learn a lot about physics, working with people, and myself. As overwhelming as it was, I appreciate this experience, especially now that it is all behind me. I am grateful to Jon Paley who prodded me to answer questions which had to be answered but looked too difficult to be solved in a short amount of time. Special thanks to Holger Meyer for managing the data taking. It has been a pleasure to work with so many physicists from FNAL, LLNL, and other institutions in the USA and abroad. Thank you for helping me to grow.

Many thanks to John Oliver, Nathan Felt, Sarah Harder, Sten Hansen, and Terry Kiper for teaching me to work with the electronics. The world of experimental particle physics was a lot of fun when I had a chance to work with my hands and have someone in the room next door to help me.

Most importantly, these years would have been impossible without the continuing support from my wife Irina.

Chapter 1

Introduction

Particle production is one of the classic phenomena studied by many experiments over the twentieth century. While many experiments focused on production of exotic particles, there were few high statistics measurements of inclusive production of pions, kaons, and protons. Some cross sections were measured with bubble chambers, but most high statistics measurements were done with single arm spectrometers [2, 12, 1], and therefore did not provide complete coverage of space in longitudinal and transverse momentum (see Figure 1.1)¹. As a result, hadronic production models like MARS[35] and FLUKA[24, 25] have limited data to be tuned with, and in some cases give significantly different results.

Scarcity of hadronic production data affects every neutrino experiment[17, 33, 34, 26] as accelerator made and atmospheric neutrinos come from the decay of pions and kaons produced in interactions of protons with matter. In the case of NuMI²/MINOS³ experiment, 120 GeV/ c protons are incident on a carbon target which is two interaction lengths long. The uncertainties in particle production models largely cancel in comparison of the near and far detector data, but calculation of neutrino flux with various hadronic production models differ by up to 30% (Figure 1.2). Since the near detector sees a line source of neutrinos and the far detector sees a point source of neutrinos, these uncertainties do not cancel completely, and the near/far detector comparison depends on the hadronic production model.

Recently, the NA49 experiment at CERN published results of the measurement

¹We will refer to longitudinal momentum (along the direction of the incident particle) as p_z and to transverse momentum (perpendicular to the direction of the incident particle) as p_T .

²Neutrinos at the Main Injector

³Main Injector Neutrino Oscillation Search

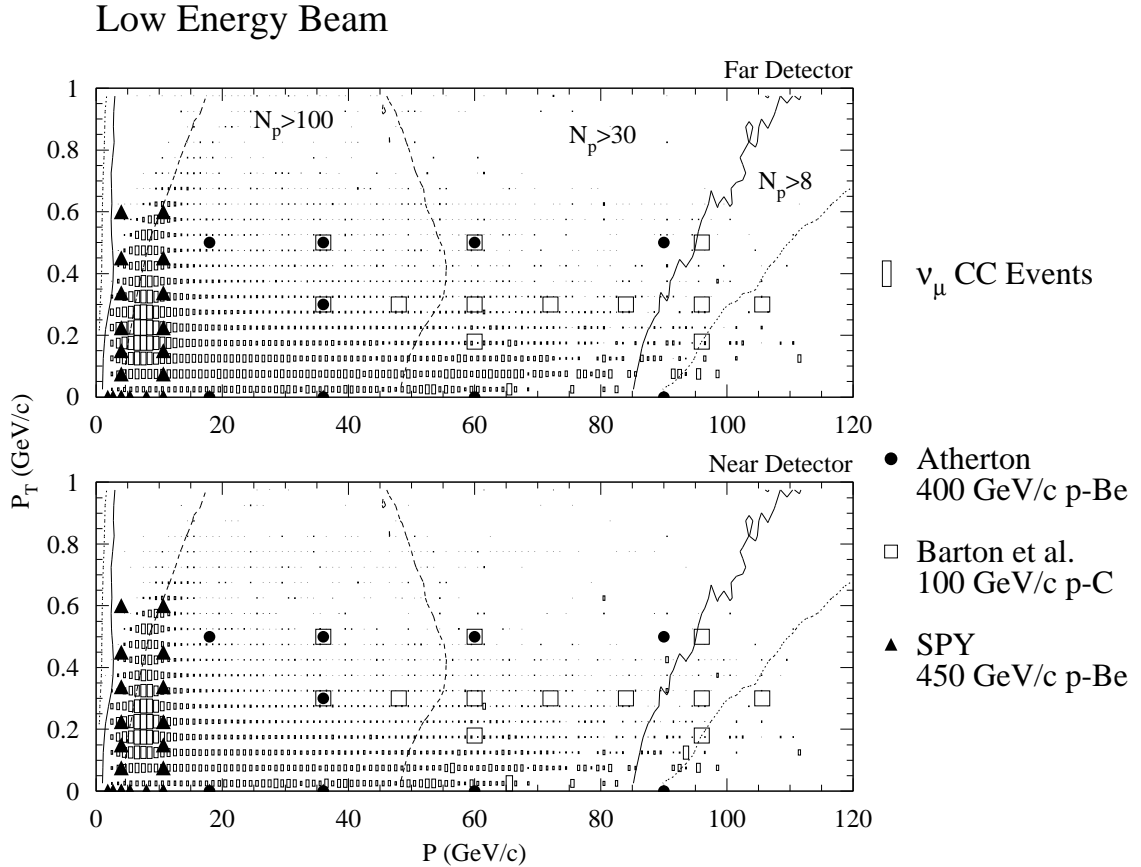


Figure 1.1: The plot from [9] shows the spectrum of pions which produce neutrinos in the MINOS far and near detectors. Superimposed are appropriately scaled data from single arm spectrometers[2, 12, 1].

of charged pion production in proton carbon collisions at 158 GeV/c [16], which is close to NuMI proton beam of 120 GeV/c. However, the secondary and tertiary particle production on the NuMI target is significant, so if one is to tune Monte Carlo models to better predict neutrino flux, it is essential to have the data of hadronic production of pions, kaons, and protons on carbon at lower momenta. Moreover, large fraction of high energy neutrinos come from decay of charged kaons (see Figure 1.3), so knowledge of kaon flux is necessary as well.

The Main Injector Particle Production (MIPP) experiment was designed to measure the total charged particle production of π^\pm , K^\pm , p , and \bar{p} by tagged beam of pions, kaons, and protons on nuclear targets. Experiment is capable of selecting beam momentum from 5 to 85 GeV/c, or run with 120 GeV/c proton beam from the Main Injector

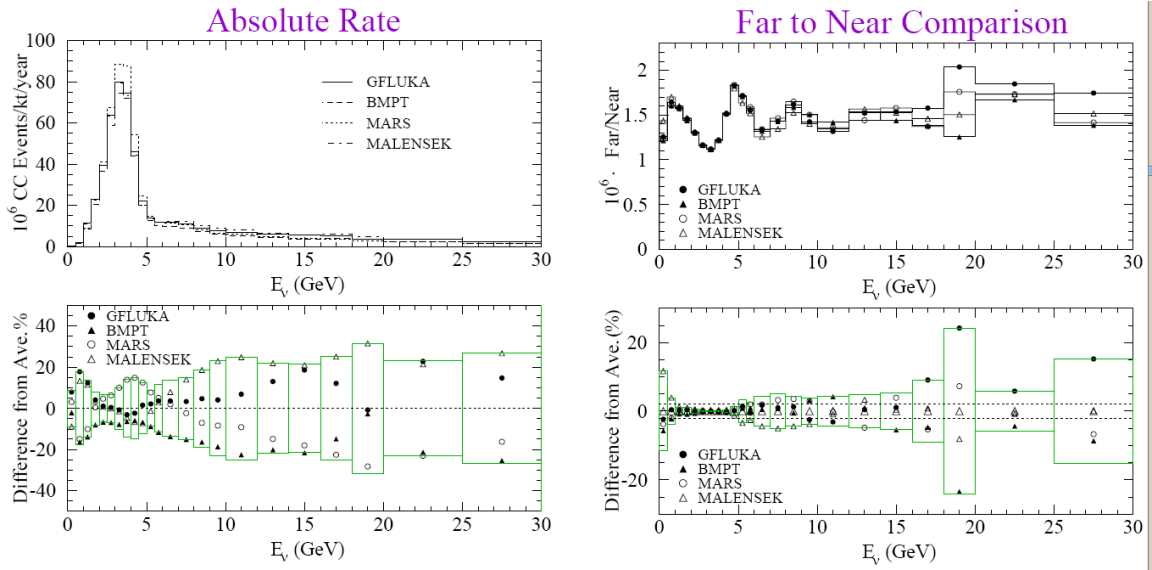


Figure 1.2: Uncertainties in neutrino flux calculation in NuMI beam. Since the MINOS near detector sees a line source of neutrino and far detector sees a point source, these uncertainties do not cancel for all momenta of interest, and having better understanding of hadronic production minimizes systematic error due to neutrino flux prediction.

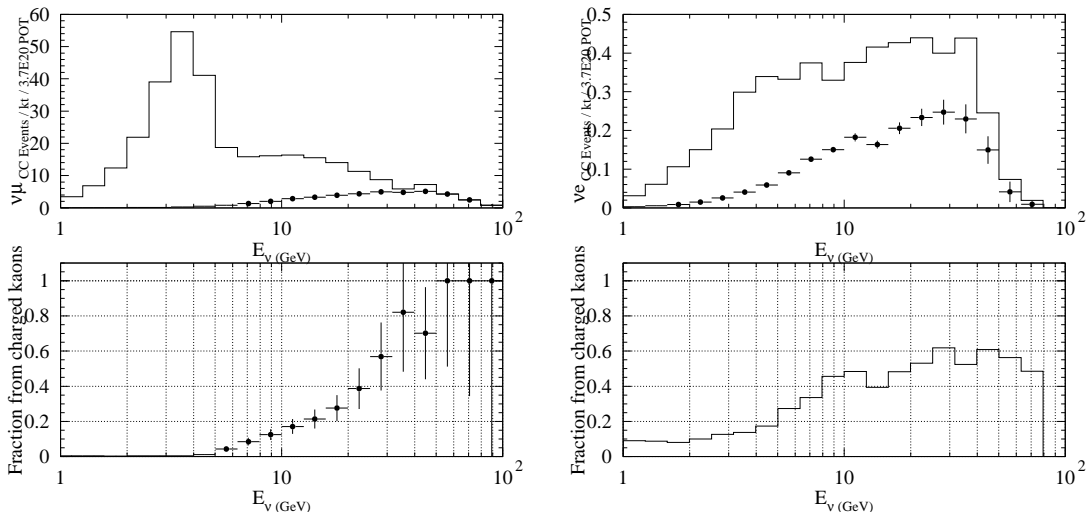


Figure 1.3: MINOS muon neutrino (left) and electron neutrino (right) fluxes and the fraction of neutrinos produced in kaon decays.

at Fermilab. A time projection chamber (TPC) provides nearly complete coverage for the forward-going particles, and wire chambers allow measurement of momentum up to 120 GeV/ c . Particle identification can be done for nearly all momenta of particles produced on the target using energy loss in the TPC, time of flight, threshold Cherenkov, and ring imaging Cherenkov counters.

In addition to taking data on thin nuclear target, MIPP experiment directly measured particle production on a replica of the NuMI target. Thus it is possible to cross check the understanding of NuMI hadron flux by comparing the spectrum from the actual target to the model of secondary production by using the proton carbon data at 120 GeV/ c and hadron carbon data at lower momenta. This improved understanding of hadronic flux will be useful to the MINOS collaboration when in a few years statistical errors improve to their current systematic error from particle production.

Measurement of the pion/kaon production ratio on a thin carbon target with $p_z > 20$ GeV/ c presented here is the first step towards better understanding of NuMI hadron flux using MIPP data.

Chapter 2

MIPP Detectors

The MIPP spectrometer, shown in Figure 2.1 consists of a number of subsystems designed to provide tracking and identification of charged particles. The experimental target is located within a few centimeters of the front of the TPC. The chamber allows the reconstruction of tracks in three dimensions and the momentum measurement of low momentum tracks. Two magnets, Jolly Green Giant (JGG) and Rosie, have vertical magnetic fields in opposite directions. The net effect of the two magnets is a transverse displacement of the track from the straight line in the xz -plane. Position measurement in the four drift chambers (DCs) and two proportional wire chambers (PWCs) make it possible to measure the momentum of high-momentum tracks. Charged particle identification is done by different detectors – TPC, time of flight wall (TOF), threshold Cherenkov (CKOV), and ring imaging Cherenkov (RICH) counters, depending on momentum of the particle. Finally, electromagnetic and hadron calorimeters make it possible to identify electrons, gamma rays, and neutral particles. All subsystems are described in detail below.

2.1 Tracking

The spectrometer provides data to reconstruct incoming beam particle and secondary particles from interactions on the target. Three small drift chambers upstream of the target (BCs) are able to reconstruct the incident particle trajectory (track). The TPC, four DCs, and two PWCs can reconstruct tracks coming out of an interaction. A summary of all wire chamber physical properties is given in Table 2.1 and operational conditions in Table 2.2.

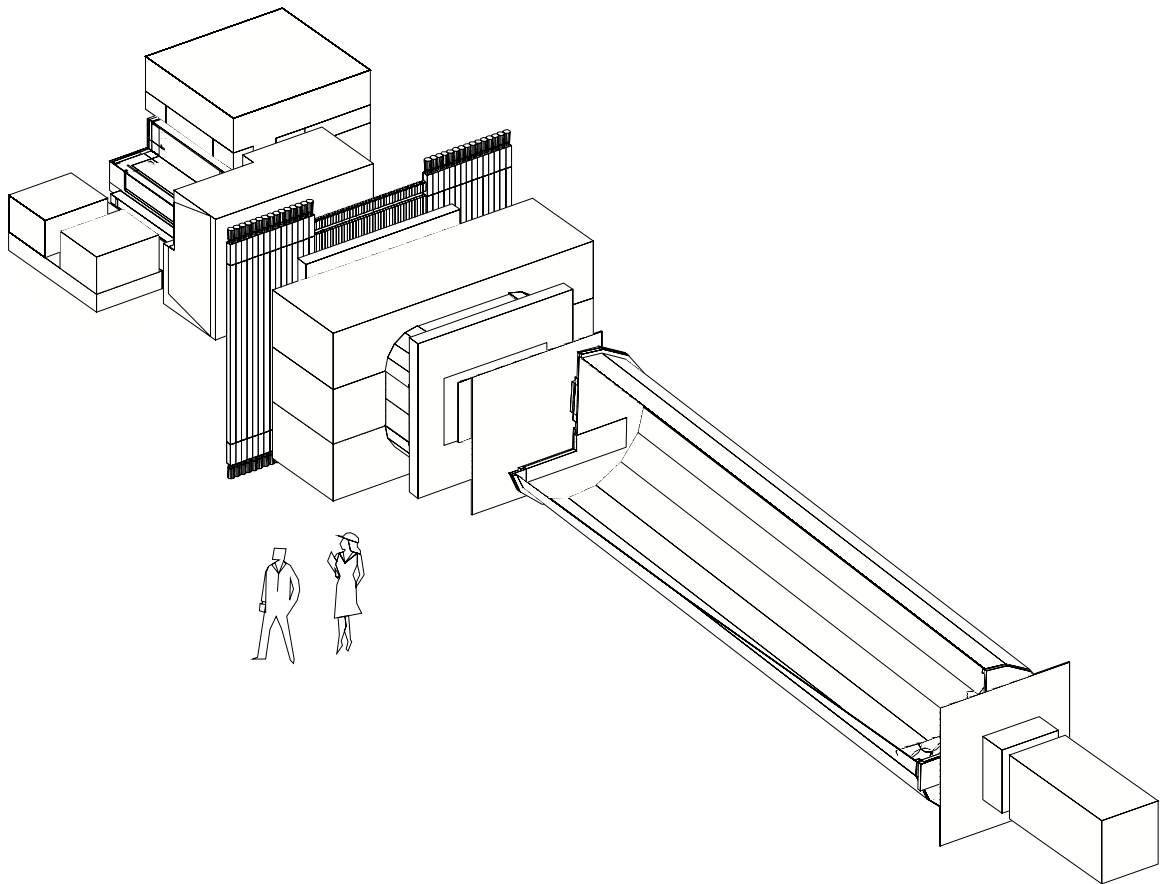


Figure 2.1: Schematic of the MIPP spectrometer. From upper left-hand corner shown are TPC inside the JGG magnet, threshold Cherenkov, time of flight wall, Rosie magnet, DC4, PWC5, RICH, PWC6, electromagnetic calorimeter, and hadron calorimeter.

	Wire spacing (mm)	Active area (cm)	Number of wires	Wire angles to vertical	z in MIPP geometry (cm)
BC1	1.016	15.24 × 10.16	160	±21.60°, ±7.93°	-4821.04
BC2	1.016	15.24 × 10.16	160	±21.60°, ±7.93°	-2465.86
BC3	1.016	15.24 × 10.16	160	±21.60°, ±7.93°	-1176.31
DC1	3.4925	182.88 × 121.92	512	±21.60°, ±7.93°	-586.83
DC2	3.175	152.40 × 101.60	512 (448)	±21.60°, ±7.93°	-427.99
DC3	3.175	152.40 × 101.60	512 (448)	±21.60°, ±7.93°	-352.62
DC4	3.175	152.40 × 101.60	512 (448)	±21.60°, ±7.93°	63.38
PWC5	3.000	200.00 × 200.00	640	0°, 90°, ±28.07°	132.99
PWC6	3.000	200.00 × 200.00	640	0°, 90°, ±28.07°	1415.92

Table 2.1: Summary of multi-wire chambers parameters. DC2-4 have 448 wires in the wide-angle planes and 512 in narrow-angle planes. Position along the beam axis is given in offline geometry coordinates, where $z = 0$ is inside the Rosie volume and the target is located at $z \approx -829$ cm.

	Cathode voltage (kV)	Gas
Beam chambers	1.4	82 : 15 : 3 Ar/C ₄ H ₁₀ /methylal
Drift chambers	1.85 – 2.05	69 : 28 : 3 Ar/C ₄ H ₁₀ /methylal
Proportional chambers	3.0	76.5 : 8.5 : 15 Ar/CH ₄ /CF ₄

Table 2.2: Summary of chamber operation conditions

2.1.1 Drift Chambers

The BCs and DCs were used by FNAL E690 experiment and the BCs are described in detail in [11]. The beam chambers span a distance of 37 m and provide 150 μm resolution of position and 5 μrad resolution of angle of the incoming particle when multiple scattering is negligible. Moreover, 1 mm wire spacing allows us to distinguish multiple particles and 1 μs range of the TDC allows one to measure the time of the track with respect to the trigger signal.

Chamber electronics consists of preamplifiers, Nevis discriminators, and a LeCroy 4290 CAMAC TDC system to measure drift time with 1 ns resolution. The LeCroy 4290 system consists of 32-channel TDC CAMAC modules, organized in a total of 15 CAMAC crates with 20-22 modules per crate. Each crate was read out by a dedicated CAMAC crate controller. When triggered, controllers zero suppress the data and send them out to a module located in a normal CAMAC crate.

2.1.2 Proportional Chambers

The two PWCs straddling the the RICH counter were used in the NA24 experiment at CERN and later at the SELEX experiment at FNAL. Chamber construction is documented in [14].

These chambers are read out with RMH electronics[32] designed at CERN in the 1970's. Preamplified signals from all 8 planes are discriminated and latched during 500 ns gate in eight crates, each filled with twenty 32-channel cards. Zero-suppressed read out consists of up to 4000 16-bit words indicating which channel of which module had a signal above threshold.

Unfortunately, only two of four planes in PWC5 could hold high voltage, which made the chamber less efficient and made it impossible to reduce combinatorial combinations of hit positions. However, these problems had a small effect on track reconstruction.

2.1.3 Time Projection Chamber

The TPC is the centerpiece of the MIPP spectrometer. With particle position measured at tens of points, the chamber is an excellent detector for pattern recognition of the tracks in an event. It was constructed in 1990 at the Lawrence Berkeley Laboratory

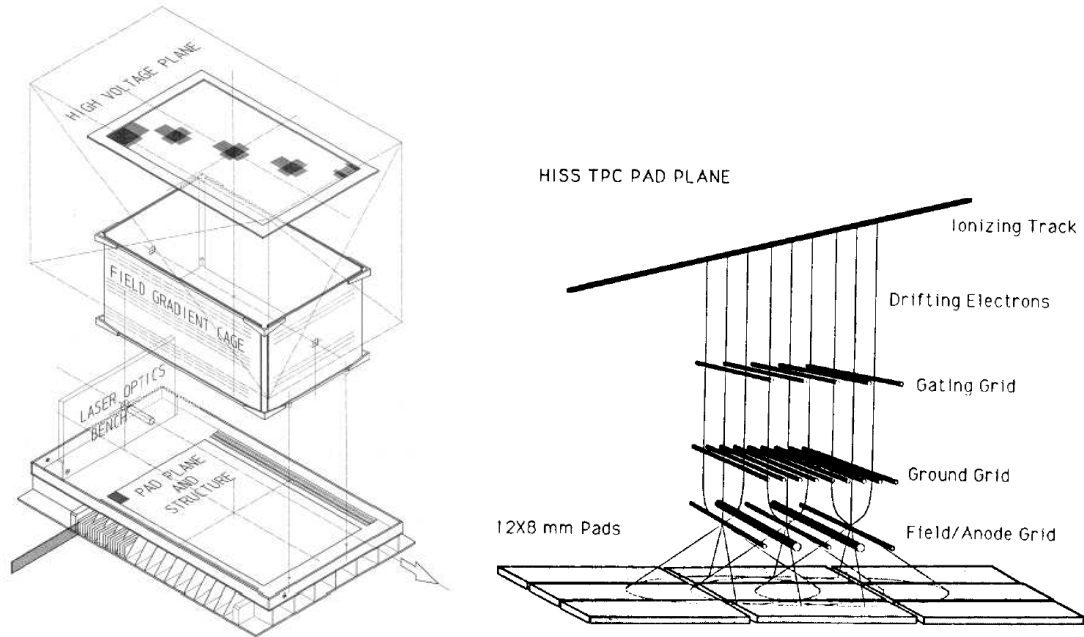


Figure 2.2: Schematic view of the TPC volume and pad plane with anode and ground wires, taken from [18].

BEVALAC facility for the EOS experiment[4, 23, 18, 28, 36, 43, 19]. Prior to being used by the MIPP experiment, it served the BNL E895 and E910 experiments.

Electrons ionized in the $96 \times 162 \times 81 \text{ cm}^3$ gas volume by charged particles drift down in a uniform vertical electric field of 125 V/cm . At the bottom of the drift volume (see Figure 2.2), in the region between ground and anode wires, an avalanche is created by the strong electric field ($> 3 \text{ kV/cm}$) near the anode wires, achieving gas gain of 3000. The image charge on the pad plane 4 mm below the anode wires is recorded by the electronics.

The pad plane is divided into 128 pad rows along the z -axis with 120 $0.8 \times 1.2 \text{ cm}$ pads per row along the x -axis. The pad rows record a slice of ionization energy in z . Each pad is digitized by 12-bit flash ADC at 10 MHz. With drift velocity of about $5 \text{ cm}/\mu\text{s}$, this gives 5 mm sampling along the vertical. A typical minimum ionizing track would leave signal on about 3 pads in a given row, with the amplified signal spread over seven 100 ns time buckets. The large number of measurement points (up to 128 per track), yields sub-millimeter position resolution on the track position.

The TPC is read out through dedicated VME boards organized into four crates. Fiber optics links connect the VME boards to the pre-amplifier/shaper “sticks” located

underneath the pad plane. A stick covers two half pad rows.

2.2 Particle Identification

The spectrometer allows us to identify the incident particle and secondary particles. Incident particles are identified using two differential Cherenkov counters: one for π/K and one for K/p separation. Secondary particles are identified by different detectors depending on their momentum. From low to high momentum the detectors are the TPC ($< 1 \text{ GeV}/c$), the TOF wall ($< 3 \text{ GeV}/c$), the CKOV ($< 17 \text{ GeV}/c$), and the RICH for particles with higher momenta.

2.2.1 Beam Cherenkov

Each beam Cherenkov counter consists of a long cylindrical radiator volume and a head at the downstream end, which contains two PMTs. The head contains a focusing mirror which reflects the light onto a photomultiplier tube (PMT) covered by a second mirror with a hole. The aperture of the hole is chosen in such a way that Cherenkov light emitted at angles below the cutoff would hit the PMT behind the second mirror (inner PMT) whereas light emitted at larger angles is reflected onto the outer PMT. The cutoff Cherenkov angles for the inner PMTs are 5 and 7 mrad respectively for the upstream and downstream counters. Radiator volume lengths are 22.9 m and 12.2 m so that statistically the same number of photo-electrons hit inner PMTs on both counters.

The density in the upstream counter is set to achieve the kaon Cherenkov angle of 5 mrad – focusing its light onto the inner PMT. Pions with identical momentum radiate light at a larger angle, missing the inner PMT and hitting the outer PMT. At the momenta of interest ($< 90 \text{ GeV}/c$), protons do not radiate at all under these conditions.

Similarly, the pressure in the downstream counter is set so that the proton Cherenkov light hits the inner PMT, but not the outer PMT. The outer PMT collects light emitted at angles less than 30 mrad. This is important since for momenta below $\approx 32 \text{ GeV}/c$ the pion Cherenkov angle is so large that the photons emitted by pions are no longer collected on the outer PMT. This property is independent of the gas that fills the radiator volume.

One of the challenges for identification of incident particles is the large span of momenta (5-90 $\text{ GeV}/c$). The counters are tuned to different beam momentum by establishing the desired gas density in each counter. The cylinders can only be pressurized to $\approx 1.5 \text{ atm}$,

therefore at low momenta a heavy non-flammable gas has to be used in order to obtain a positive tag for protons below 30 GeV/ c and for kaons below 20 GeV/ c . MIPP used C₄F₈O for this purpose. Nitrogen at different densities was used for all higher momenta. However, at 5 GeV/ c even the heavy gas is not dense enough for kaons or protons to radiate. But at that momentum we can take advantage of the measurable difference in time of flight of the three particle species between the front of the beamline and experimental target.

2.2.2 Threshold Cherenkov

The threshold Cherenkov consists of 96 toroidal mirrors at the downstream wall of the counter filled with heavy gas. Each mirror is positioned to focus Cherenkov light onto one of the 96 PMTs positioned at the top and bottom of the counter. The mirrors are positioned in such a way that each mirror reflects Cherenkov light onto one and only one PMT if the particle emanates from the target. In some instances, of course, light is shared by 2 or 3 mirrors, which can be taken into account once the track trajectory is known. The PMT windows are coated with wavelength shifter to make them sensitive to ultraviolet light. The charge off the PMTs is digitized with LeCroy 4300 ADC modules and discriminated signals are recorded with LeCroy 3377 multi-hit TDCs.

Historically, the CKOV was operated with Freon, but due to modern environmental regulations, we had to use a much more expensive alternative C₄F₁₀. At atmospheric pressure, this gas has pion threshold at 2.6 GeV/ c , kaon threshold at 8 GeV/ c and proton threshold at 17 GeV/ c .

2.2.3 Beam Time of Flight

Three scintillator counters are placed in the beamline: T01 about 3 m upstream of the target, TBD about 20 cm upstream of BC1, and T00 another 20 m upstream, almost immediately after the secondary beamline collimator. These detectors had to satisfy the following objectives:

1. Form a beam trigger signal,
2. Provide a reference start time for the TOF wall,
3. Resolve pileup,
4. Identify incoming beam particles at momentum of 5 GeV/ c .

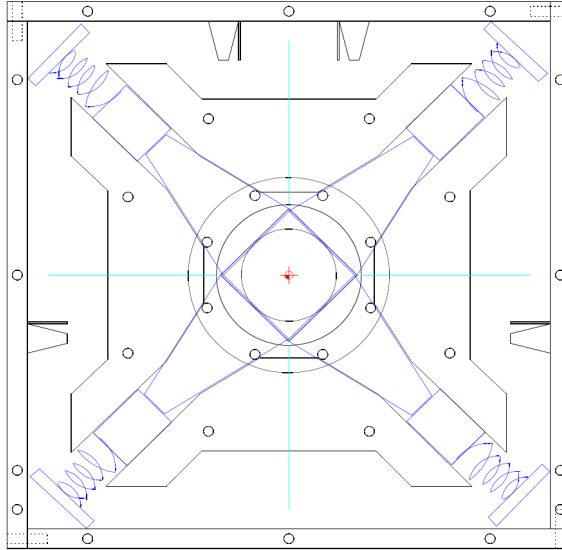


Figure 2.3: Schematic of T00 and T01 construction. Light from the scintillator is collected onto four PMTs by light guides. Phototubes are held in place by springs. TBD assembly is similar, except no light guides are used.

Each counter consists of a square piece of scintillator and four Hamamatsu R5900U PMTs, one on each side of the scintillator. Figure 2.3 shows schematic of the inside of the counters. The initial two counters T00 and T01 are equipped with light guides, which improve timing resolution. TBD counter, which was added at a later time to help form the beam trigger does not have the light guides, as we were not planning on using it to measure time of flight of beam particles. In practice, degradation of timing resolution is dominated by delay cables, so the resolution of TBD is comparable to that of the T01, and exceeds that of T00. The one sigma resolution of the TBD-T01 time difference for 120 GeV/ c protons is 120 ps.

Each PMT signal is split with 90% of the charge to a discriminator and TDC, and 10% to an ADC. Knowing the amount of charge on a given PMT allows for offline hit time corrections.

The temporal coincidence of TBD and T01 signals is used to form a beam trigger. Further discussion of the experimental trigger is presented in Chapter 3.

Two sets of CAMAC TDCs measure PMT hit times with respect to the experimental trigger time:

- LeCroy 3377 with 0.5 ns resolution and up to 16 hits in 512 ns window,
- LeCroy 2229 with 30 ns resolution, but only 1 hit in 60 ns window.

The first set of TDCs helps to determine presence of pileup (multiple incident particles in one event), while the second set of TDCs is used to reconstruct particle flight time and serves as the reference time for the time of flight wall.

2.2.4 Time of Flight Wall

Conceptually the TOF wall is straightforward: 54 3-m long vertical scintillator bars form a solid wall 3.5 m wide. The central 2 m are covered by 40 5×5 cm bars and the wings are covered by 10×10 cm bars. Both ends of each bar are capped with Winston cones to collect light onto Hamamatsu R5900U PMTs (identical tubes used in the beam counters).

The reference time of the incident particle is measured by beam counters (Section 2.2.3), and the time of arrival of resulting particles is measured on both ends of each scintillator bar. The segmentation of the wall is such that the probability of two particles hitting the same bar is small.

2.2.5 Ring Imaging Cherenkov

The ring Imaging Cherenkov (RICH) was built for the SELEX experiment [20, 22, 21] in the 1990's. We filled the 10 m long radiator volume with carbon dioxide to a total pressure of ≈ 1.03 atm. In the course of the run, the volume was slowly leaking, so CO_2 was added on a weekly basis keeping the pressure constant within 1%. The level of oxygen contamination in the vessel was less than 1000 ppm.

Sixteen hexagonal spherical focusing mirrors mounted at the downstream end reflect Cherenkov light onto an array of 1 inch PMTs located on the upstream flange of the cylinder above the beam window. The mirrors cover an area of approximately 2×1 m. The average focal radius of mirrors is 19.8 m with RMS spread of less than 3 cm. Prior to the run, mirrors were aligned with laser so that their foci were at the center of the PMT array.

A holder plate supports the PMTs in a hexagonally close-packed array of 89×32 tubes. The plate separates the array from radiator volume with 2848 individually glued quartz windows and holds aluminized mylar cones for each phototube. Essentially 100% of reflected Cherenkov light that reaches the front of the vessel gets to the phototubes.

Light is detected with two different types of phototubes:

- Hamamatsu R-760 with quartz windows and response down to 170 nm.
- FEU-60 with glass windows covered by wave-shifter so as to reach same wavelength range as the Hamamatsu tubes. These PMTs are about 42% as efficient, but they are 10 times as cheap.

Unfortunately, in March 2004 one of the FEU-60 PMT bases caught fire, resulting in a 30% loss in the number of PMTs. Fortunately, this accident had a negligible impact on the particle identification capability of the device because of the high index of refraction of CO₂ – the radius of a $\beta = 1$ ring is 29.5 cm and typical number of hit tubes per ring is over 20.

All photomultiplier tubes were powered with 6 high voltage supplies, each capable of delivering 200 mA at 3 kV. 32 PMTs with similar nominal high voltage were grouped together, and a number of different voltages in steps of 20 V were created with 6 Zener diode chains.

The signal is read out with custom electronics designed at FNAL, built and tested at Harvard University. The setup is shown schematically in Figure 2.4. 89 front-end cards are arranged into 3 crates (30, 30, and 29 cards), each crate controlled by one VME controller board.

Each of the 32 channels on the front-end cards contains a differential amplifier with a gain of ≈ 20 and an analog comparator. The threshold is programmable for each channel in steps of 0.8 mV. The discriminated signal is continuously pushed into a pipeline memory. When a controller board is triggered, the trigger is forwarded to front-end cards and the data that falls within the strobe gate is latched. RICH electronics can be strobed multiple times before a read out command must be issued. Pipeline delay is programmable for each front-end board and can be set as large as 128 clock ticks (2.4 μ s with 53 MHz clock). The programmable delay facilitated adjusting the timing of PMT signals to the trigger. Since the instantaneous rate at MIPP was quite low, we latched the signal with a fairly wide strobe gate of 100 ns. The electronics is capable of using gates as short as two clock cycles.

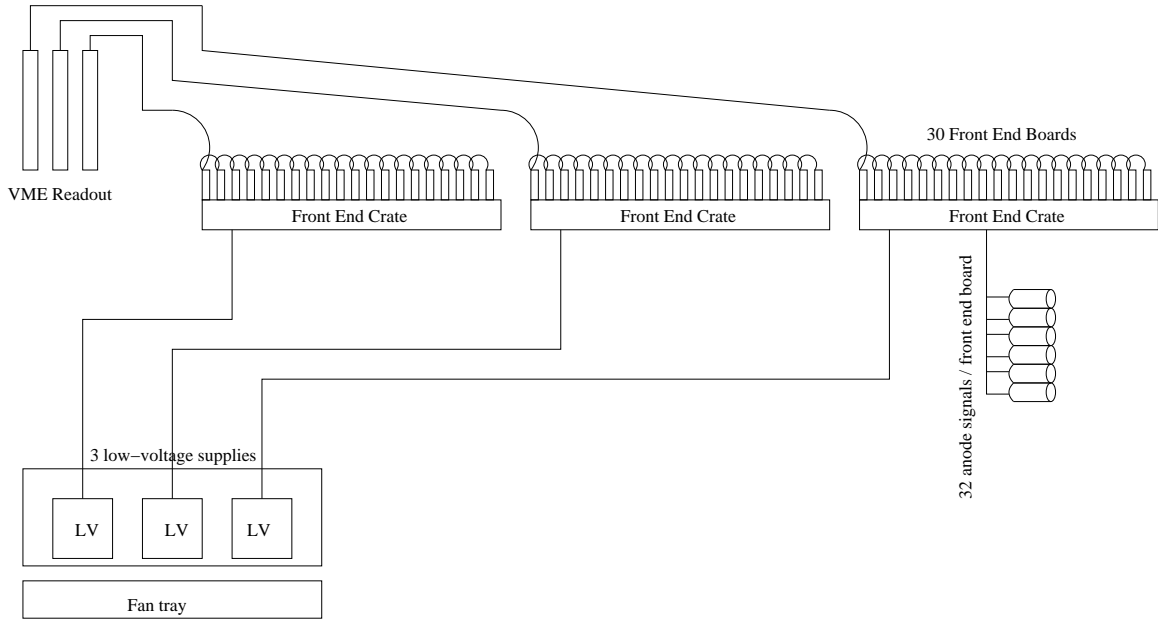


Figure 2.4: Schematic of RICH electronics setup.

2.2.6 Electromagnetic Calorimeter

The primary purpose of electromagnetic calorimeter is to measure the production of forward high energy photons. It consists of 10 planes of alternating horizontal and vertical wire planes sandwiched between 15 mm thick lead plates. Each active plane is comprised of eight 8-inch wide, 1-inch thick chambers with 8 wires per chamber.

The detector read out with custom ADC CAMAC units built by the University of Michigan group. Because 1970's ADC chips are used, the calorimeter is the second slowest detector after TPC in terms of read out speed.

2.2.7 Hadron Calorimeter

The hadron calorimeter is the last detector on the experiment, located directly behind the electromagnetic calorimeter. Its purpose is to measure the production of forward-going neutrons. It was previously used by the HyperCP[8] experiment. The active volume consists of four scintillator plates sandwiched between lead sheets. It is meant to determine the energy of hadrons by summing energy deposition of the resulting hadronic shower initiated in the lead sheets that comprise the majority of the interaction lengths of the detector. The scintillator plates are segmented into two cells symmetric about the beam axis with a

total of eight cells. Each cell is read out by one photomultiplier tube. The calorimeter also serves as the experiment's beam dump

The calorimeter read out through custom built electronics designed at the University of Virginia. PMT signal passes through ADC driver module and the amplified charge is then digitized by a 16-bit CAMAC ADC. With pedestal widths of 2 – 3 ADC counts, each cell has dynamic range of about 5000.

2.3 Analysis Magnets

MIPP uses two magnets for momentum measurement: Jolly Green Giant and Rosie. For safety, magnetic fields are set so that the kick angles are about equal and opposite ($\int B_y dl \approx 1 \text{ Tm}$). This way regardless of momentum, beam is absorbed by the beam dump.

While the experimental hall was still empty, all three magnet field components were mapped onto a 2-inch three dimensional grid using a Ziptrack field measuring device. The device consists of three Hall probes, one for each component of the magnetic field. As the probe holder glides along the track, the field is sampled every 2 inches, with the three components sampled in the same point at slightly different times. Complete field maps are used to compute trajectories of particles in the non-uniform field and to compute trajectories of electron drift in the TPC.

The Jolly Green Giant magnet was originally built at Harvard in the 1960's. Its aperture is sufficiently large for the TPC to fit, but its magnetic field is non-uniform towards the edges of the TPC drift volume, hence corrections of up to 7 cm in TPC hit positions have to be made. Rosie magnetic field is much more uniform, but unfortunately, its aperture is a few centimeters too small for the TPC to fit.

One of the coils in Jolly Green Giant was damaged and had been repaired prior to magnet being installed in the MIPP hall. In the course of the run, two coils shorted out, so the experiment ended up having 3 distinct field maps. Only the first map was measured with Ziptrack, but computer models of the magnetic field showed that the differences in field components due to different coil combination are small and can be neglected.

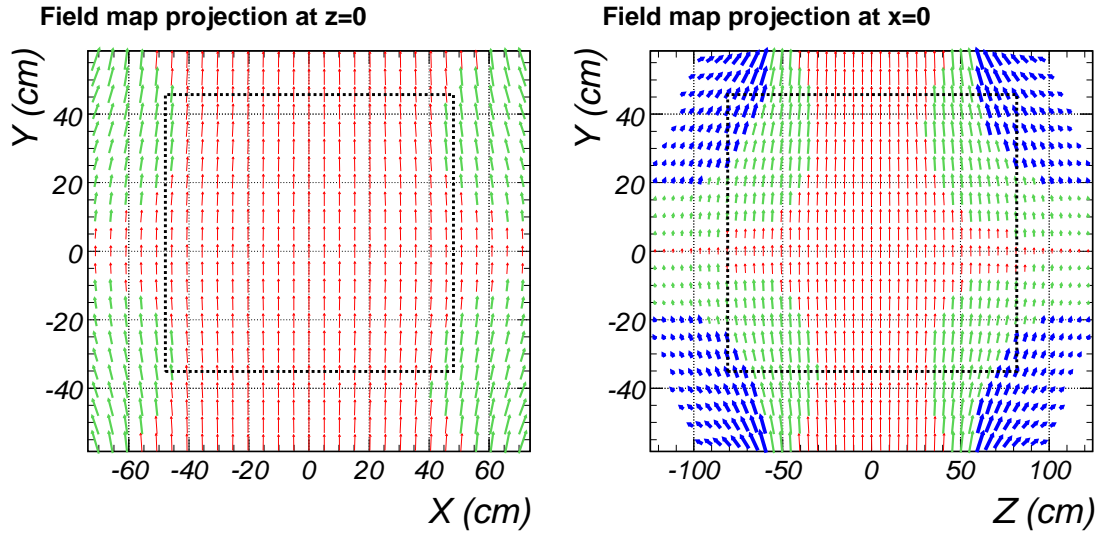


Figure 2.5: Projections of the JGG field map in slices along the center of the magnet. Regions of non-uniform field are highlighted with thicker arrows where $B_i/B_y > 0.1$ and thickest arrows where $B_i/B_y > 0.5$. The dashed line shows the boundary of the TPC drift volume.

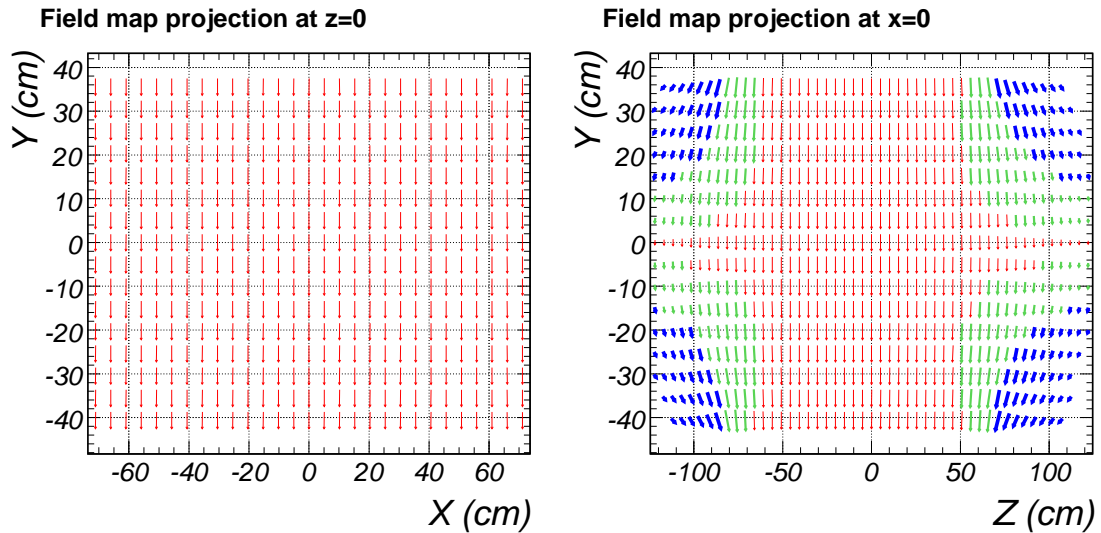


Figure 2.6: Projections of the Rosie field map in the same volume as those in Figure 2.5, using the same legend for thickness of arrows.

Chapter 3

MIPP Trigger

The experimental single-level trigger is fairly simple: the first stage of the trigger decides on the species of the particle and the second stage on whether or not the particle interacted in the target. Thus, 7 physics trigger bits are typically in use: untagged beam, three particle species, and three particle species with interaction. Different trigger bits are scaled down before a global OR is formed in order to achieve about a 20% minimum bias and 80% interaction trigger mix. Unless prohibitively high scale-down factors are required, the factors are chosen to record an even mix of protons, kaons, and pions.

Since the trigger has only one level and does not provide a fast clear, a decision has to be made in the shortest time possible so as not to degrade the resolution of the TOF system. In the final implementation, the trigger is formed about 250 ns after the incident particle passes through the target.

3.1 Particle Identification

3.1.1 Momentum Above 20 GeV/ c

As described in Section 2.2.1, at 20 GeV/ c and above, the pressure in the beam Cherenkov counters can be tuned so that all charged particles radiate light. The four PMTs are abbreviated as UI for upstream inner, UO for upstream outer, DI for downstream inner, and DO for downstream outer. Under these operating conditions, the particle trigger bits are defined as:

- $\pi : \overline{UI} \cdot UO$

- K: $UI \cdot \overline{UO}$
- p: $DI \cdot \overline{DO}$

At 35 GeV/c and above, pion and kaon Cherenkov angle in the downstream counter is below 30 mrad, so under those conditions, a more stringent trigger could be formed, based on all four PMTs:

- π : $\overline{UI} \cdot UO \cdot \overline{DI} \cdot DO$
- K: $UI \cdot \overline{UO} \cdot \overline{DI} \cdot DO$
- p: $\overline{UI} \cdot \overline{UO} \cdot DI \cdot \overline{DO}$

In the interest of saving trigger time, this momentum-dependent trigger was not implemented.

3.1.2 5 GeV/c Momentum

Using the beam Cherenkov counters, it is not possible to tag protons with momentum below about 20 GeV/c, and kaons cannot be tagged when their momentum is below 11 GeV/c, as a sufficiently high gas density could not be obtained. Even if it were possible to do that, the gas density would be so large that multiple scattering in the counters would degrade the knowledge of position and direction of the incoming particle. Instead, at 5 GeV/c, we rely on particle time of flight to distinguish kaons and protons offline. Figure 3.1 shows that the task is easily achieved at such a low momentum.

For the purpose of the trigger, both beam Cherenkov densities were tuned to radiate on pions, muons, and electrons. Then proton plus kaon trigger was the absence of signal in all beam Cherenkov PMTs. Both negative and positive beams of this momentum are primarily ($\approx 90\%$) composed of pions, with similar fractions of protons and kaons, so it was acceptable to accumulate equal fractions of protons and kaons, as long as they could be distinguished offline.

3.2 Beam Cherenkov Operation

Pressure scans were done in order to find the optimal operating gas densities of the beam Cherenkov counters. A stand-alone program read out latched discriminated

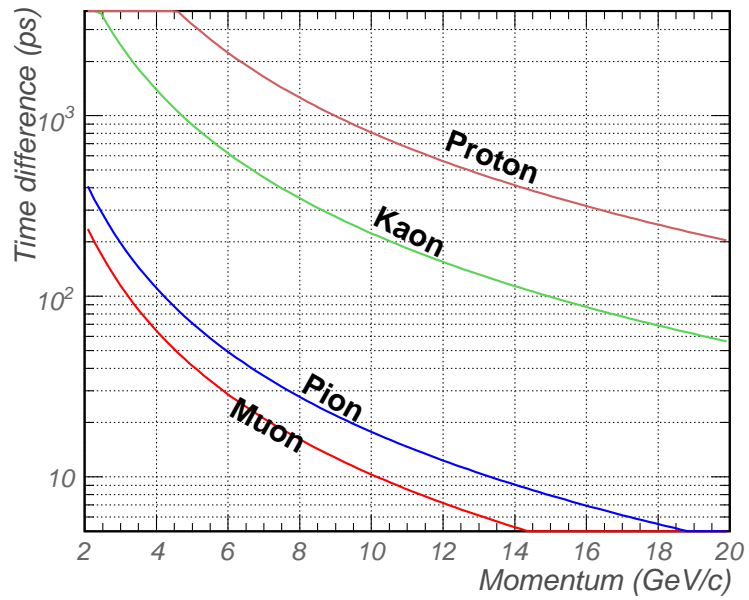


Figure 3.1: The difference in time of flight between the T00 and T01 counters for a $\beta = 1$ particle and muons, pions, kaons, and protons. With time resolution of 200 ps, it is possible to do a 3-sigma proton/kaon separation below 11 GeV/c , and kaon/pion separation below 6 GeV/c .

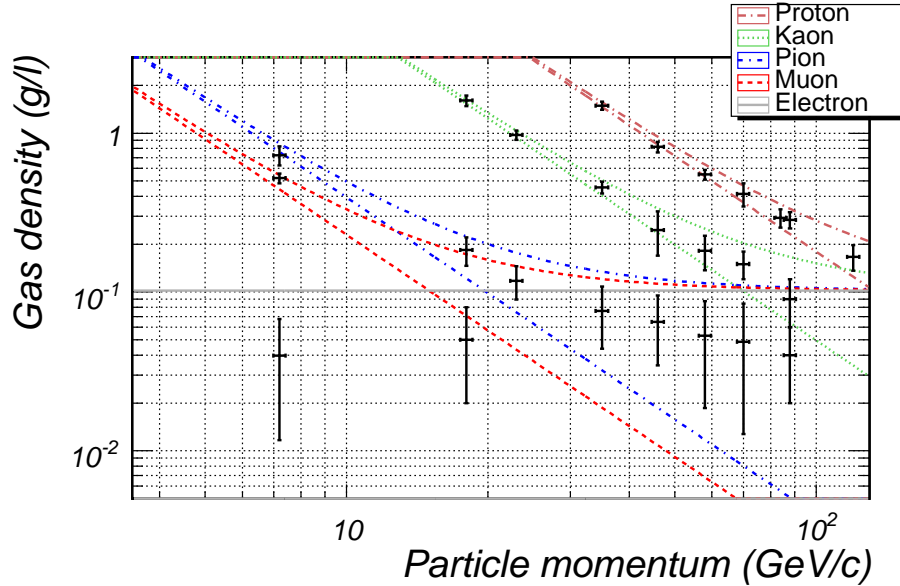


Figure 3.2: Summary of the upstream beam Cherenkov pressure curves with nitrogen. The two curves for each particle species are the threshold density and the density at which the Cherenkov angle is 5 mrad. Superimposed data are the centers of peaks of $UI \cdot \overline{UO}$ in pressure curves.

PMT signals at different pressures, recording 10000 triggers per pressure point. From the frequency of occurrence of the 16 different PMT combinations, one can find the peaks corresponding to the different particle species. Figure 3.2 shows the summary of all pressure scans data in nitrogen.

For momenta 20 GeV/ c and above, RICH rings can be used to measure the trigger purity. In a 20 GeV/ c beam, we can identify protons by the lack of a signal, but at 35 GeV/ c and above, all 3 particles radiate, so the purity measurements shown in Figure 3.3 are more reliable. Still, in most cases, the trigger purity is above 70%, and as one would expect, it is above 99% for the majority particle.

3.3 Interaction Trigger

The initial MIPP interaction trigger was based on the multiplicity of DC1, requiring 2 or more wire clusters in at least three of the four planes. This trigger has the following problems associated with it:

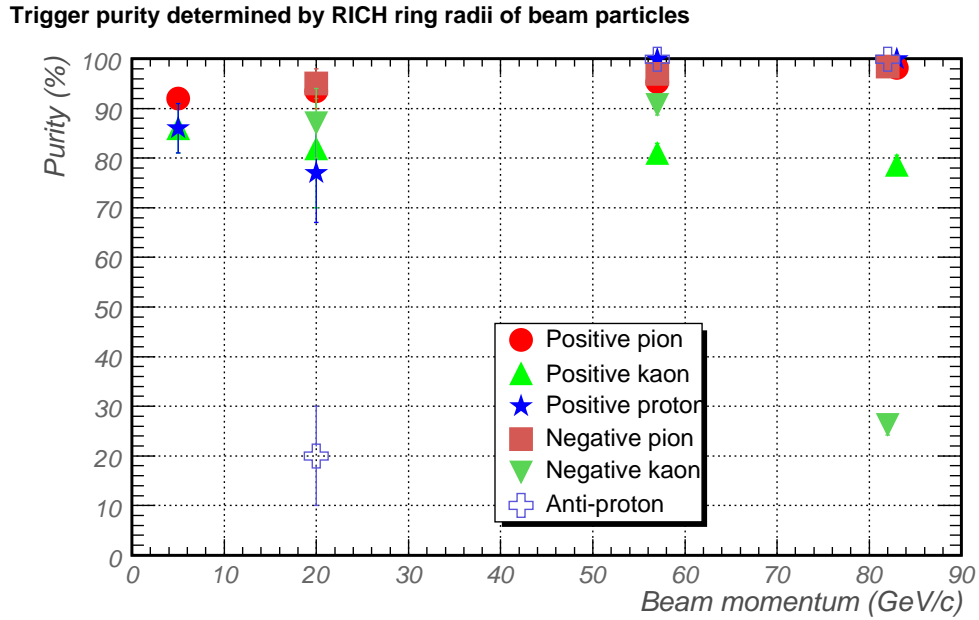


Figure 3.3: Trigger particle tag purity as measured by the RICH.

- a) The large chamber area made it highly susceptible to poor beam conditions,
- b) The chamber is sometimes noisy because of low discriminator thresholds,
- c) The small efficiency for two-particle final states where one particle is soft.

To address the problems of DC1 interaction trigger, a scintillator interaction trigger was built. Both triggers were used in order to measure systematic effects of each interaction trigger.

3.3.1 DC1 Trigger

Drift chamber preamplifier cards, each serving 8 wires, are mounted on the chamber. Four preamplifier cards are connected to one discriminator. Each discriminator outputs 32 ECL signals, one per wire, and 4 ECL OR signals, one for each cluster of 8 wires. The cluster OR signals are sent to majority logic units (LeCroy 4532 CAMAC module) to create a multiplicity interaction trigger, called iDC. The trigger fires if at least 2 different clusters fire in at least 3 out of 4 planes.

3.3.2 Scintillator Interaction Trigger

The scintillator interaction trigger (Scint)[7] is much simpler than the iDC. A 3.175 mm thick 5.40×7.62 cm piece of scintillator is placed ≈ 1.5 cm after the target. The scintillator has an interaction length of 81.9 g/cm^2 and density of 1.032 g/cm^3 , so its thickness is about 0.4% interaction length. Clear fibers collect light from the two shorter sides of the scintillator. The other ends of the fibers are closely packed onto the face of a Burle 83054H PMT. By safety rules, in order to operate the trigger with the liquid hydrogen target, all high voltages (i.e. PMT) had to be at least 3 m away from the target, hence calling for rather long fibers. Even with 3 m of fiber, the counter gets about 73 photoelectrons per minimum ionizing particle (mip).

The PMT charge is amplified with a LeCroy 612 AM PMT amplifier module, creating two copies of the signal. One copy goes directly to an ADC, the second copy goes to an analog splitter. The outputs of the splitter are discriminated with two different thresholds, creating **SciHi** (≈ 3 mip) and **SciLo** (≈ 1.5 mip) digital signals.

The problem with the **SciLo** signal is that the Landau tail of the single-particle energy deposition dominates the count rate from the 1% interaction length target. At the threshold level of **SciHi**, only $\approx 1\%$ of single-particle states deposit enough energy to create the trigger signal, thus yielding trigger purity of about 50%

3.4 End of Spill and Calibration Triggers

Each accelerator beam spill was followed by an end of spill trigger and a few pulser calibration triggers.

Upon receipt of the end of spill trigger, the detectors were not triggered, and only the following actions were taken:

1. Scalers for the entire spill were read out and cleared;
2. A record was written to the database with the number of different triggers recorded in the spill;
3. Buffered data were transferred from the PowerPCs to the DAQ server.

On calibration triggers, the detectors were triggered by a pulse generator. These triggers were used to calculate pedestals and to identify hot channels.

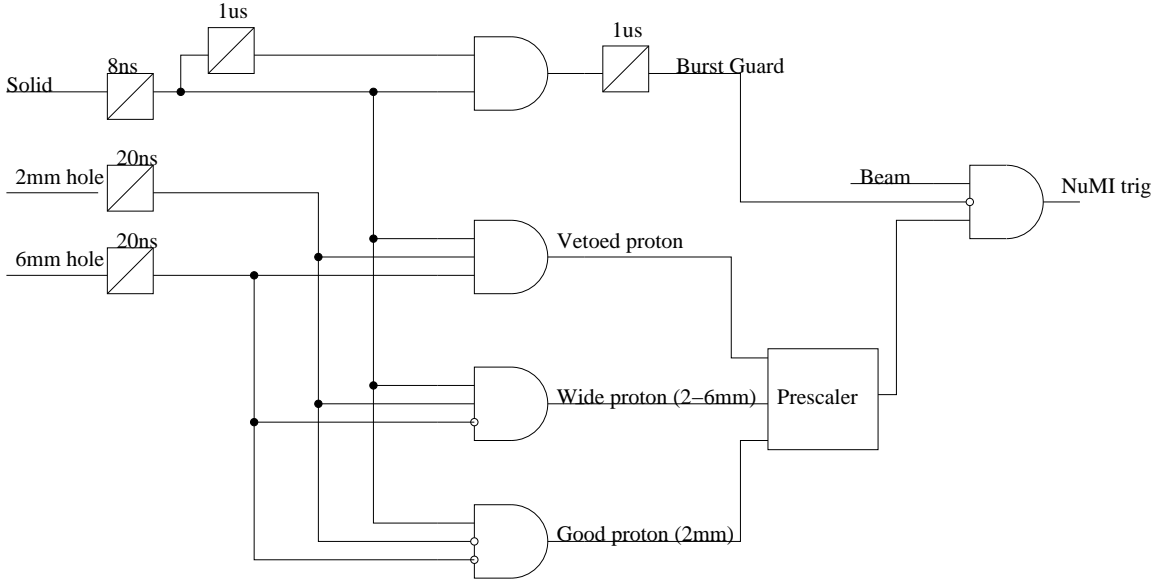


Figure 3.4: Logic for the NuMI trigger. The trigger rate in each of 3 different regions could be scaled down, so that even with a poorly tuned beam, we could ensure that most triggers were taken with protons on target.

3.5 Veto Counter

In order to limit the effect of beam halo coming from the primary target in secondary beam configurations, a $35 \text{ cm} \times 40 \text{ cm}$ scintillator paddle with a 4.32 cm diameter hole is mounted on a plate of aluminum 140 cm upstream of the target. Two PMTs are attached to the sides of the veto scintillator through light guides, and the logical AND of the two PMTs form an 80 ns veto signal to reject events with particles outside of the hole.

3.6 NuMI Trigger

When data were taken with the MINOS target, no interaction trigger was required since the target is 2 interaction lengths. However, the beam in MC7 was larger than the NuMI beam, so a dedicated trigger counter was built in order to make the beam phase space at MIPP similar to NuMI beam. The counter consisted of three pieces of scintillator: solid, with a 2-mm diameter hole in the center, and with a 6-mm hole. The paddles with holes were used to veto particles that were too far from the beam center, thus ensuring that most data are taken under conditions resembling the NuMI proton beam. The logic for this

trigger is shown in Figure 3.4

In addition to vetoing wide particles, the trigger had a $1 \mu\text{s}$ “burst guard” which prevented the trigger from firing if two protons were separated by less than $1 \mu\text{s}$. The burst guard was necessary in order to prevent pileup. Since almost all protons interact in the target with fairly large multiplicities, two events, on top of one another, would be very hard to reconstruct in the TPC.

Chapter 4

Data Acquisition System

The MIPP data acquisition system (DAQ) was designed for rather modest requirements. The trigger rate was limited to about 60 Hz due to the time it took to zero suppress TPC data. Around 90% of the data came from the size of the TPC event, 100 kB on average. The initial design specifications were to read out all of the detectors in a mode where beam was delivered in 1 s spills, 20 spills per minute, or 2 MB/s. The DAQ was able to keep up with the data rate, which did not exceed fifteen 600 ms spills per minute (see Chapter 5).

Figure 4.1 shows the overall schematic of the data acquisition system. Computers which made the experiment work included

- a DAQ server with two network cards, which was connected to the public net and to the private subnet.
- Six VME PowerPCs (PPC), connected to the DAQ server through 100 Mbit network with the ability to access the VME and CAMAC read out electronics and send data to the server.
- An online monitoring machine, which enabled monitoring of data in real time.
- A High Voltage machine, which was used to control and monitor all PMT and TPC high voltages (wire chamber high voltages were manually controlled).
- A database server, which ran a PostgreSQL database where all online information was stored.

This chapter describes all the online software that was running on all of these machines.

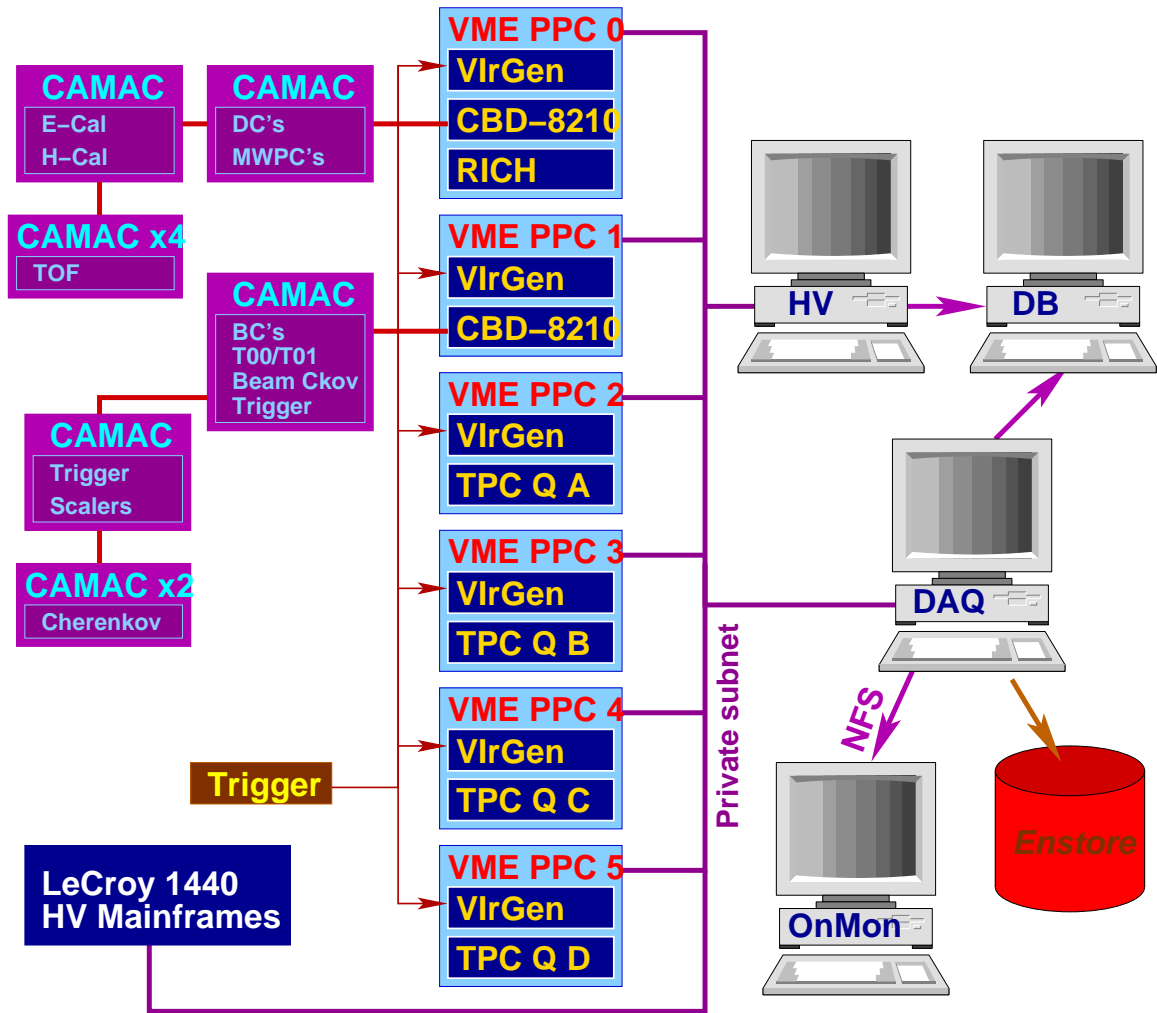


Figure 4.1: Schematic of data acquisition setup. Of the six VME PowerPCs, four were dedicated to control and read out of the TPC quadrants, and the other two read out the rest of the detectors, mainly CAMAC electronics. Read out processes were triggered through VME interrupts delivered by VlrGen boards. High voltage mainframes connected to private subnet as well, were controlled and monitored by HV machine. Detector data were written out to dedicated files, and online monitoring data were stored in a PostgreSQL database. Online monitoring was done by exporting data disks through NFS. Finally, data were regularly shipped to the FNAL robot tape storage (Enstore).

4.1 VME and CAMAC Interfaces

At the time when MIPP DAQ was designed, one of the most affordable ways to access VME bus was to run Linux on VME PowerPCs made by Motorola. MIPP required 6 MVME 2432 computers: four dedicated to TPC read out and 2 more to read out all other detectors. These machines had 350 MHz processors and 256 MB of memory. They were placed into 6U VME crates so as to have direct access to the VME bus. An on-board Tundra Universe II chip provided access to the VME bus. MIPP used a small subset of its capabilities for VME transactions: A24/D16, A16/D16, A32/D32 data transfers, and interrupt handling.

Most detectors were configured and read out through CAMAC electronics. Two CBD 8210 CAMAC branch drivers made by Creative Electronics Systems S.A. were used to drive two CAMAC branches with a total of 12 crates.

4.1.1 Linux on PowerPC

PowerPCs have two links to the outer world: a 9600-baud debug port and a 100-baseT ethernet connection. Having no hard drive, the computer had to be booted from a remote machine. The kernel, loaded through the TFTP protocol, would know the location of the file system mounted through NFS. On-board flash memory could be programmed to select the server and location of the kernel file on the server.

Linux kernel 2.2.12 and the file system based on glibc-2.2.5 was compiled from scratch using gcc-2.95.3. We inherited a file system compiled for kernel 2.1.24 with egcs. Since the compiler and kernel had significant changes and improvements, it was necessary to upgrade the operating system. I followed Linux From Scratch[27, 3] recipe to rebuild the file system.

At the time the file system was built, it seemed that having the RedHat Package Manager (RPM) on the operating system would be necessary to facilitate system administration. However, since PowerPCs were on the private subnet, security was not an issue, and system maintenance was much simpler than for computers exposed to the internet. The system had to be supported on 6 computers only, so most packages compiled from source were not re-installed or incorporated into the RPM database.

Even though the number of packages is not nearly as large as on most modern operating systems, having to serve 6 systems from the DAQ server required a significant

amount of disk space. To reduce the total size of the systems, debugging symbols were stripped from executables and system libraries. Furthermore, unlike system binaries and libraries, one common `/usr/share` directory was exported to the PPCs and MIPP online software resided in `/usr/local`, common to all 6 computers.

4.1.2 Handling interrupts in the kernel

The kernel module to drive the Tundra II chip, written by Gabriel Paubert, could handle I/O, but could not deliver interrupts into user space. In order to simplify debugging, we wanted to write all online software in user space. Performance loss due to this inefficiency could be tolerated because TPC electronics rather than VME read out was the bottleneck. In order to deliver interrupts into user space, a modification to the module was necessary.

Final design was implemented using semaphores. A user's program would increment the value of the semaphore, release `VIRGen` busy (see Section 4.1.4), and then block until the semaphore value was reset to zero by the kernel. This design avoided race condition where the program would miss an interrupt, but as we found out, had a different flaw. Since Linux is not a real-time operating system, in rare instances when the kernel was busy, it would fail to unblock the program through the semaphore. To circumvent this problem, `mdd` (see Section 4.2.4) had a dedicated thread which checked the status of the hardware busy for that VME crate and would signal the blocked thread if the kernel failed to unblock it. However, sustained trigger rates of multiple kHz would cause kernel panic and crash the PowerPC. For lack of need and shortage of time, that problem had not been resolved since production data acquisition rates did not exceed 100 triggers per second.

If time and manpower permitted, interrupt handling would be redone through the `poll()` system call rather than through semaphores. We are quite certain that a significant improvement in kernel stability could be achieved that way.

The DAQ system was configured to expect two interrupt types:

- Data trigger on VME interrupt 2;
- End of spill trigger on VME interrupt 3.

The difference between the two interrupts was that on end of spill trigger only scalars were read out in the trigger process and all other processes sent empty data messages.

4.1.3 CBD 8210

CBD 8210 is a double height VME card allowing a parallel CAMAC branch with up to 7 crates to be driven through VME. Presently, the boards are quite difficult to find, and MIPP was able to obtain only 3: two for active use and one spare. The board characteristics include

- 16 and 24-bit CAMAC transfers,
- Two external VME interrupts,
- Comprehensive LAM (look at me) handling,
- Addition of a DMA module.

Our primary objective of 16 and 24-bit transfers was easily accomplished as it is well documented in the manual [13]. Before the **VIrGen** boards were ready, we were also using the two interrupts to trigger the read out. Unfortunately, we were not able to get DMA transfers to work, although the primary reason was the lack of need to boost CAMAC transfer performance: the TPC was limiting data rates and it was read out directly through VME.

4.1.4 VME Interrupt Generator

VIrGen (**VME Interrupt Generator**) boards were developed at Harvard to

1. Convert trigger NIM signal into VME interrupt,
2. Time stamp each trigger to ensure that event pieces recorded on different PowerPCs corresponded to one physical event,
3. Ensure that the Linux kernel does not miss an interrupt,
4. Hold off further triggers until a process on the PPC signals that read out is complete.

The board was outfitted with four inputs for four different VME interrupts (1-4). All decisions were made by a XILINX FPGA.

The first objective was accomplished by feeding the NIM signal into a comparator, its output connected to an FPGA input. If that interrupt channel was not holding busy, then

VME interrupt on the corresponding channel was initiated and a handshake was completed with the PowerPC. All boards were running off the accelerator RF clock and a 32-bit time stamp was recorded on the clock cycle that fired the interrupt. Synchronization of timestamps across the 6 boards was achieved by resetting time stamp to 0 at the beginning of every run.

One of the issues that we encountered with Linux interrupts was that occasionally (apparently when the load was high), an interrupt would be missed. In order to solve that problem, `VIRGen` would keep resending VME interrupt until a process on the PowerPC would acknowledge receipt of the interrupt by writing to a register on the board. The frequency of repeating interrupts could be controlled through a register.

In order to synchronize all VME crates, once an interrupt was received, `VIRGen` set the corresponding TTL busy output high. Once the read out was complete, a process on the PowerPC had to clear the busy. Externally formed logical OR of all busy signals inhibited further experimental triggers.

4.2 Online Software

4.2.1 MippIo

From the start, it was decided that offline analysis would be done in ROOT, but it was suspected that ROOT I/O would not be fast enough to cope with TPC data volume, so a dedicated I/O library was written.

MippIo was designed to write data in a structured byte-packing format organized into blocks. Each block had a 12-byte header containing block ID, version, and total block size. A MIPP raw data file consisted of a file header block followed by any number of event blocks and concluded with an end of file block. In turn, each event block consisted of a number of detector blocks. Each detector block contained data as it was read from VME or CAMAC, without any pre-processing done on the PowerPCs or in the event builder.

4.2.2 Run Control and Message Passing System

The central part of the data acquisition system was the Run Control Daemon (`rcd`). The process had to perform the following tasks

- Maintain the overall state of the DAQ system;

Class name	Senders	Receivers	Description
RCMsgConnect	All	All	Message sent by a client to request new connection and response by <code>rcd</code> to acknowledge new connection
RCMsgControl	All	Detectors, event builder, <code>rcd</code>	Generic message sent to start and stop runs, and the primary way for GUI to make <code>rcd</code> act
RCMsgDataDir	<code>rcd</code>	GUI	List of directories to choose from for writing data
RCMsgEvBStatus	Event builder	<code>rcd</code>	Update <code>rcd</code> of event builder status
RCMsgMddStatus	<code>mdd</code>	<code>rcd</code>	Update <code>rcd</code> of <code>mdd</code> status
RCMsgPrescaleList	GUI, <code>rcd</code>	GUI, <code>rcd</code>	Changes and updates of prescale settings
RCMsgProcRel	Detectors, event builder, <code>mdd</code>	<code>rcd</code>	Inform <code>rcd</code> of the release used to compile a given binary
RCMsgRunConfig	GUI, <code>rcd</code>		Run configuration, including prescale settings, target, enabled detectors
RCMsgStatus	<code>rcd</code>	GUI	Update GUI of current status of the DAQ
RCMsgTarget	<code>rcd</code>	GUI	Pass a list of available targets to <code>rcd</code>

Table 4.1: Message classes implemented in run control.

- Process operator requests to start and stop data acquisition;
- Respond to exceptions and errors in the system.

These objectives were achieved by passing messages between different processes across the network.

A message passing system was implemented through stream sockets, allowing maximal flexibility and expansion of the DAQ system. A number of different messages were implemented (see Table 4.1), each having a 20-byte header containing message id, its number, size, second, and microsecond when the message was packed.

Upon start-up, `rcd` would open a socket to listen to incoming connections and would go into an infinite loop which polled all known sockets for activity. Once an event occurred on a socket, it would be processed by `rcd`. New connections were classified as event

builder, `mdd`, GUI, or detector process, and messages were processed sequentially. Since the number of connections was small (typically 8) and the response time to nearly all messages did not involve much CPU time, this simple architecture worked very well.

Once all the software on all machines was up and running in idle state, it was up to the operator to set the run conditions (trigger prescales, set of detectors, etc) through GUI and start a run. GUI would send run configuration to `rcd` and follow it up with control message to start a run. At that point, `rcd` would

1. Figure out the current target and beam momentum by reading the slow control devices;
2. Save run conditions to the database;
3. Send a start run message to the event builder;
4. Wait for the event builder to respond that the run has been started;
5. Send a start and pause run message to `mdd`'s;
6. Wait for every `mdd` to start up its detector processes;
7. Send a start run message to all `mdd`'s.

If any of the steps failed, run was terminated. In this process, only the first step would block the cycle of listening to incoming messages.

Requests to stop a run were processed in reverse:

1. Send a stop run message to all `mdd`'s;
2. Wait for all `mdd`'s to terminate child processes;
3. Send a stop run message to event builder;
4. Wait for event builder to finish writing data to disk;
5. Save run statistics to the database.

Unlike requests to start a run, any process could send a request to stop a run if it encountered an error. Alternatively, if any of the processes involved in the run would stop responding, run would be terminated by `rcd`.

4.2.3 Event Builder

Event builder is a FNAL Computing Division product that MIPP customized to our needs. It has to be able to receive parts of events (called subevents) from different sources, assemble them into an entire event, and write it to disk. At the beginning of the run, the process would be configured to expect a certain number of connections: one for each detector and one for each `mdd` involved. In order to synchronize parts of an event, each process had to be triggered to send a message to event builder even if there was no data read out. Events were assembled once all subevents were received.

Additional task of the event builder was to cut long runs into shorter subruns. A MIPP run was defined as a set of data with one system configuration (trigger scale down factors, high voltage, etc). A subrun was defined as a file with size less than 1 GB or not more than 30 minutes in duration if it contains at least 5000 events. Having multiple shorter files rather than one gigantic file facilitated data handling and expedited analysis on the batch farm.

4.2.4 MIPP DAQ Daemon

On each PowerPC, one process was

- Responding to `rcd` messages;
- Starting and stopping detector processes;
- Receiving and handling interrupts;
- Handling exceptions and errors during data taking.

It was named `mdd` because initially the DAQ was expected to rely on a different message passing system, and this would be the only “daemon” running. In a way, its functionality was similar to `rcd`: at the beginning of the run, all necessary processes were started, monitored during the run and terminated at the end of a run. The difference was that it responded to `rcd` and was not aware of the state of the entire DAQ system.

`mdd` was a multi-threaded program: one thread handled control messages and two “trigger” threads were handling interrupts on the two interrupt channels. As mentioned earlier, VME interrupts were handled by kernel and passed to user processes through semaphores. Once a trigger thread received an interrupt, it would lock a mutex, and one by

one get each of the detector processes to read data. Inter-process communication was also implemented through semaphores. It was necessary to have only one detector reading data at any given time because CAMAC operations were not done atomically: one VME operation transferred the data and a second operation read back the status of the last transfer. Hence if all detectors were read out simultaneously, a race condition was possible where a process would find out the status of a wrong data transfer.

An alternative design would be to link all detector libraries into `mdd` and avoid context switching. This approach was not pursued because we thought that better stability would be achieved if read out was done in a separate processes.

Trigger handling was done differently on the TPC crates than on the other two crates. The reason is that TPC events were interleaved, i.e. a trigger could proceed forward **before** the event was read out. Thus, on the TPC crates triggers were handled with the following sequence of events:

1. When triggered, a `VIrGen` board would set a busy and hold it;
2. Kernel would set respective semaphore to zero;
3. `mdd` would wake up and wake up TPC process;
4. TPC process would wait for the data to be ready for read out, switch the buffer where next event was written;
5. TPC process would increment the semaphore value, release `VIrGen` busy and then read data out.

The other two crates had a slightly different sequence of events: `mdd` would cycle through all detectors, increment semaphore, and then reset `VIrGen` busy. These sequences were safe against race conditions.

One of the features we found very useful was measuring read out time of every detector. This helped us to identify bottlenecks in the beginning and at a later stage was a useful debugging tool: if detector was taking much more or much less time than usual to read its data, it typically indicated a problem with the electronics, high voltage, or low voltage supplies.

4.2.5 Detector Processes

Detector processes had to fulfill a very specific role: connect to event builder, configure detector at the beginning of a run, read and buffer data for every trigger, send data to event builder on every end of spill trigger. Each process had two threads, one for each interrupt type.

4.2.6 Database Logger

In order to avoid building Postgres libraries on the PowerPC and most importantly to be able to host the database on a dedicated computer rather than the DAQ server, `dbLogger` interface was written so that executables running on the PowerPCs could add and modify entries in the database. The logger daemon, running on the DAQ server, listened to incoming connections from the PowerPCs and passed SQL commands to the Postgres server without parsing them.

The main use for `dbLogger` was to store the number of spills and triggers recorded in a given run.

4.2.7 Online Monitoring

An integral part of the data acquisition system, online monitoring was essential debugging tool and gave shifters the ability to verify in nearly real time that the data written to disk was meaningful. Having the program was also essential to debug issues in `MippIo` and detector read out code.

The monitoring was running on a dedicated computer which had the data disks mounted through NFS. The program was constantly scanning the disks for new data files and kept updating a number of histograms for all detectors. The executable was written using `ROOT` for both histograms and graphical user interface. An important part of online monitoring was writing files out at the end of each run so that histograms from different runs could be quickly compared at a later time.

4.2.8 Software Release System

The entire experiment depended on the DAQ system, therefore some order was brought into the software development cycle by compiling frozen releases. Rigorous testing was done before a release was made, and at any point in time, the most recent and the

previous stable releases were available to operators. Release of every DAQ executable for every run was stored in the database so that at a later time potential detector or data integrity problems could be easily linked to software release.

4.3 Slow Controls

The environment in the experimental hall as well as settings and readbacks of devices were controlled and continually monitored by computer. These included gas pressures, temperatures, magnet current settings, and high voltage settings.

4.3.1 iFix

The Intellusion iFix system was used as a front-end for APACS control. It was used to

1. Read air and gas pressures, multiple temperature sensors, humidity sensor;
2. Control the pressure in beam Cherenkov counters;
3. Control the flow of gas through threshold Cherenkov counter;
4. Act as an interlock on the RICH cooling system;
5. Monitor chamber gas flow;
6. Monitor gas mixing for drift chambers;
7. Monitor and control cryogenic target.

An XML-RPC server was running on the Windows PC where iFix was running to provide a way to store variables to the Postgres database and for DAQ to find out the status of the cryogenic target.

4.3.2 ACNET

ACNET is Accelerator Control NETWORK developed at and supported by FNAL. We relied upon ACNET to

1. Control and monitor secondary beamline dipole and quadrupole magnets;

2. Control momentum collimator slit width;
3. Monitor beam profiles;
4. Monitor spill structure;
5. Control and monitor analysis magnet currents;
6. Monitor Hall probes installed in the apertures of analysis magnets;
7. Control and monitor RICH high voltage supplies;
8. Control beam Cherenkov mirror positions;
9. Monitor wire chamber and EM calorimeter voltages and currents;
10. Monitor spill intensity;
11. Monitor hall and target temperature;
12. Control the target wheel position;

Similarly to iFix, we used the XML-RPC server provided by the FNAL Beams Division to control devices and record their state into the database.

4.3.3 High Voltage

High voltages on all the PMTs and the TPC anodes were controlled through two LeCroy Research Systems 1440 systems. In order to control the mainframes from the counting house 100 m away, an Equinox serial hub was connected to the private subnet. This device enabled access to serial devices over the 100 Mbit network.

Once high voltages were set, the system would continually cycle through all known channels, store the readback voltage to the database and verify that the channel did not trip. This was especially important for TPC anodes which did occasionally trip. Prompt detection of trips ensured that as little data as possible was lost.

Chapter 5

Beamline

5.1 Accelerator

The Beam for the MIPP experiment was extracted from the Main Injector. The LINAC followed by the Booster accelerate batches of protons to 8 GeV kinetic energy, and the Main Injector RF cavities accelerate protons to 119.7 GeV/ c . Up to 7 Booster batches can be injected into the Main Injector to be accelerated simultaneously. Protons for the MINOS experiment or for \bar{p} -production for the Tevatron collider are extracted in single turn. The MIPP spectrometer required resonant extraction out of the Main Injector to reduce the instantaneous rate. Proton beam extracted towards the Switchyard passed through the A-section of the Tevatron ring. At the Switchyard it could be split between the Meson Test area, the Meson Center (MC) area, and the beam dump. The MC7 hall was home to the MIPP spectrometer.

The experiment was approved under the condition that it would not impact the accelerator program by more than 5%. In practice that meant that we were not to slow down \bar{p} -production by more than 5%. At the beginning of the MIPP run, this translated into extracting all but one Booster batch to the \bar{p} -production, and slowly extracting the last batch to MIPP. Since resonant extraction increased the length of the Main Injector time cycle, while the \bar{p} stack was small and the stacking rate high, MIPP received about six 600 ms spills per minute. Once the \bar{p} stack grew and stacking rate slowed down, MIPP received up to 15 spills per minute.

In March 2005, the NuMI beamline started receiving proton beam for the MINOS experiment, and in April 2005, the accelerator complex operation was changed so that NuMI

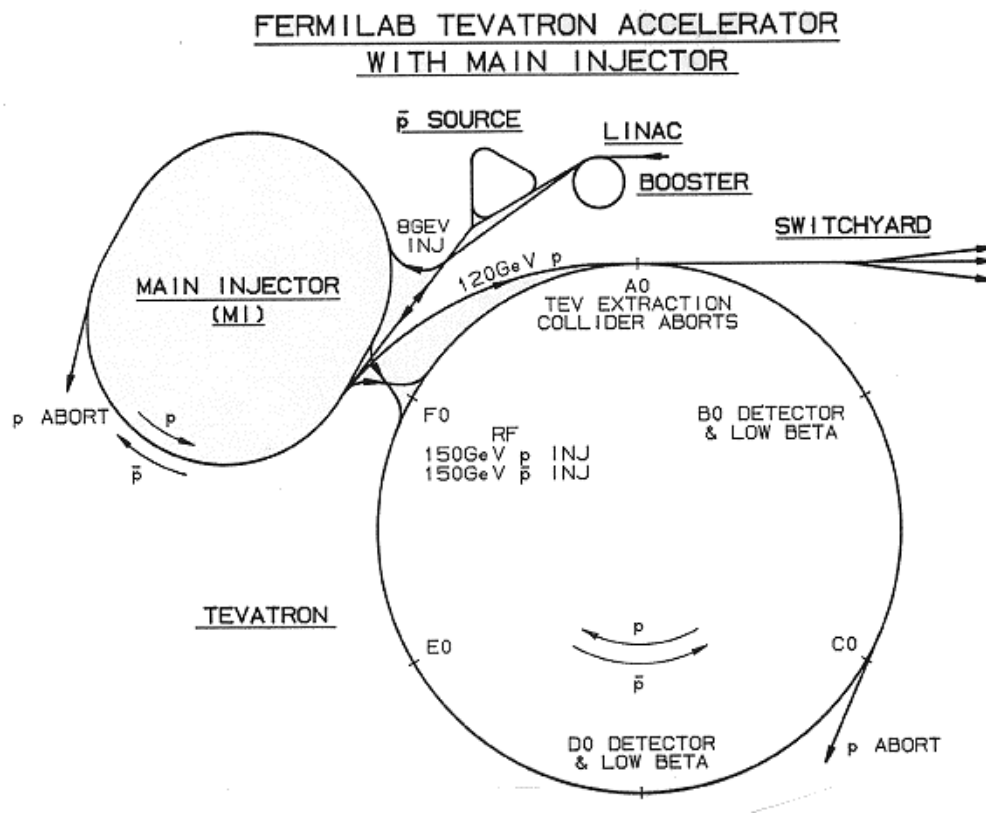


Figure 5.1: Schematic of the FNAL accelerator complex. The MIPP experiment was located in the beamline past Switchyard.

and \bar{p} -production co-existed with single-turn extraction to each destination, and a 4 second spill was extracted to the Switchyard once every 2 minutes. MIPP operated under these conditions through February 2006.

5.2 Primary Beam

The MIPP beamline was operated in two distinct modes:

- 120 GeV/ c primary protons
- 5 – 90 GeV/ c secondary particles produced on a copper target.

The minimum rate at which protons could be extracted from the Main Injector was about 10^8 particles per second. Radiation safety mandated that the experimental hall was to receive no more than 10^6 particles per second. Under normal circumstances this limitation did not affect data rates, since considerations of pileup and build up of space charge in the TPC made it impossible for the experiment to handle more than 10^5 particles per second, more realistically $3 - 5 \times 10^4$. In short, the primary proton intensity had to be reduced by at least 3 orders of magnitude in the beamline between the Main Injector and MC7 hall. This was achieved by blowing up the beam size before passing it through a pin-hole collimator, and then focusing the beam on the experimental target.

For the NuMI target running, beam intensity was further reduced to about 10^3 particles per 4 second spill. This was necessary because with a 2 interaction length target, nearly 90% of incident particles interact, hence higher rates would create unacceptable level of pileup.

5.3 Secondary Beam

At the entrance to the MC6 area, 120 GeV protons were focused onto a $0.5 \times 0.5 \times 20$ cm copper target, located 97 m upstream of the experimental target. The copper target is about 2 interaction lengths, hence a tenth of the primary beam was not interacting and was dumped into a series of concrete blocks. Beam was struck the target at 1.3° with respect to the horizontal, and 4 dipole kicks – two before and two after the slit collimator – brought a horizontal beam onto the experimental target.

In order to minimize dp/p , a large dispersion had to be achieved at the collimator. Six quadrupole magnets – three before and three after the collimator – enabled us to increase the dispersion of secondary particles and then focus the beam on the target.

A simulation of particle production on the copper target predicts RMS transverse momentum of about 400 MeV/ c . The physical transverse dimension of the target is ± 2.5 mm. Hence, the RMS emittance of the secondary beam ¹ varies from about 200 mm·mrad at 5 GeV/ c to 11 mm·mrad at 90 GeV/ c . The tails of the distribution make the total emittance roughly 4 times larger. The experimental target is 5 cm in diameter, and reliable beam Cherenkov operation requires less than 1 mrad divergence, so that the maximum total emittance needed by the experiment is 25 mm·mrad. Hence, for all beam momenta, we had to cut down emittance of the beam.

5.3.1 Optimizing Beam Quality

Once the MIPP detectors were up and running, we quickly realized that in order to take quality data with secondary beam, not only did we have to focus the beam on the target, but also reduce the amount of beam halo that results from secondary beam scraping beamline elements. There is an infinite number of quadrupole current settings that provide a well focused beam, but most of them result in significant scraping in the dipole beam pipes downstream of the collimator and degrade the data quality in two ways:

- Faking the interaction trigger, especially iDC trigger,
- Filling up the TPC volume and the wire chambers with so many tracks that event becomes unreconstructable.

The effect of beam halo on the interaction trigger was reduced by relying more heavily on the `Scint` trigger (see Section 3.3.2). The veto counter further helped to reduce the fraction of unwanted events. However, the right way to improve operating conditions was to address the source of the problem by altering the beamline settings.

A complete model of the secondary beamline was assembled and analyzed using OptiM software[31]. The model included the apertures of the beamline elements, and a realistic calculation of the magnetic field in the dipoles and quadrupoles based on mea-

¹The primary proton beam was larger than the dimensions of the target.

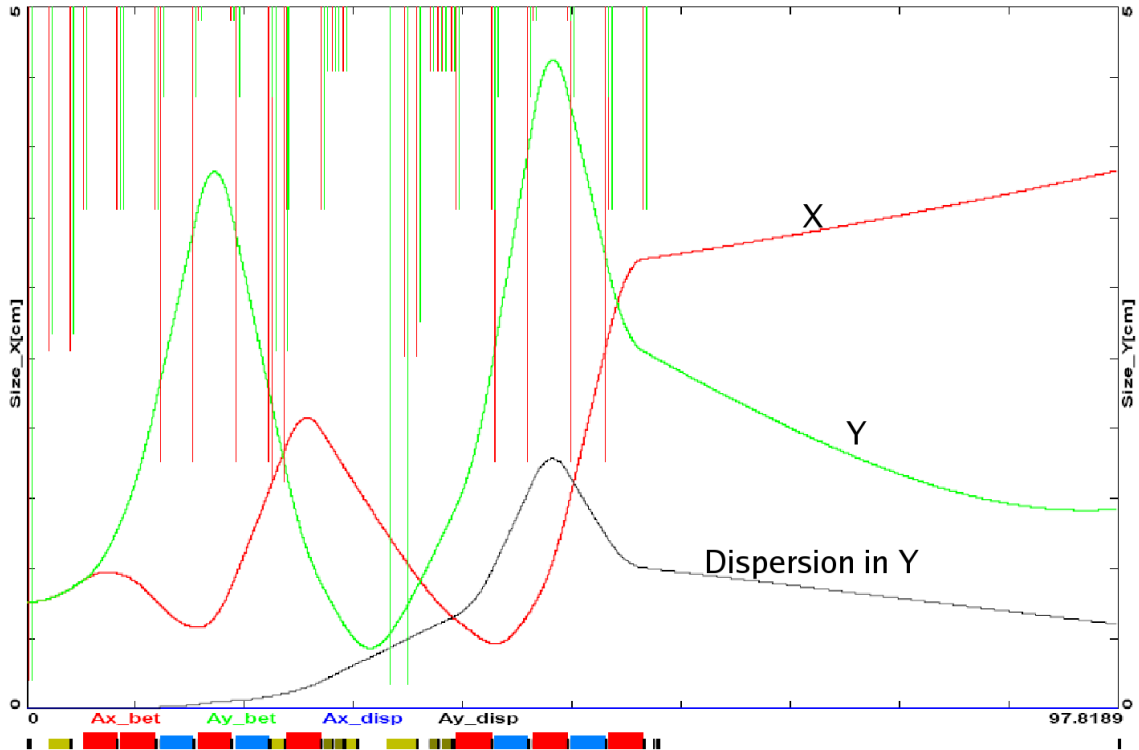


Figure 5.2: The plot shows beam sizes and dispersion superimposed on top of specified apertures (red for x and green for y). Apertures exist in the model as line objects (rather than as boxes), hence the aperture is specified at the front and at the back of every beamline element. Shown at the bottom are beamline elements: the tallest six red boxes are quads, the four medium blue boxes are dipoles, and khaki short boxes are scrapers and the collimator.

surements done at the FNAL Technical Division.² Once this model was complete, one could quickly understand what was happening. Significant scraping occurred in the last dipole magnet, well after the collimator, with only one quadrupole magnet behind it (see Figures 5.2 and 5.3). Of course, this is one of the worst places where scraping could occur.

While it was no longer feasible to move the beamline elements, the following approach helped select an acceptable solution leaving all the elements in their positions.

Instead of modeling the forward-going beam, beam parameters (emittance, β -function, and its derivative) were chosen at the **experimental target** and the beam was transported **backward**. The beamline settings were chosen so that the beam was far away

²The model assembled for use with Methodical Accelerator Design (MAD) Program lacked apertures, and hence was incapable of addressing the problems that MIPP experiment was facing.

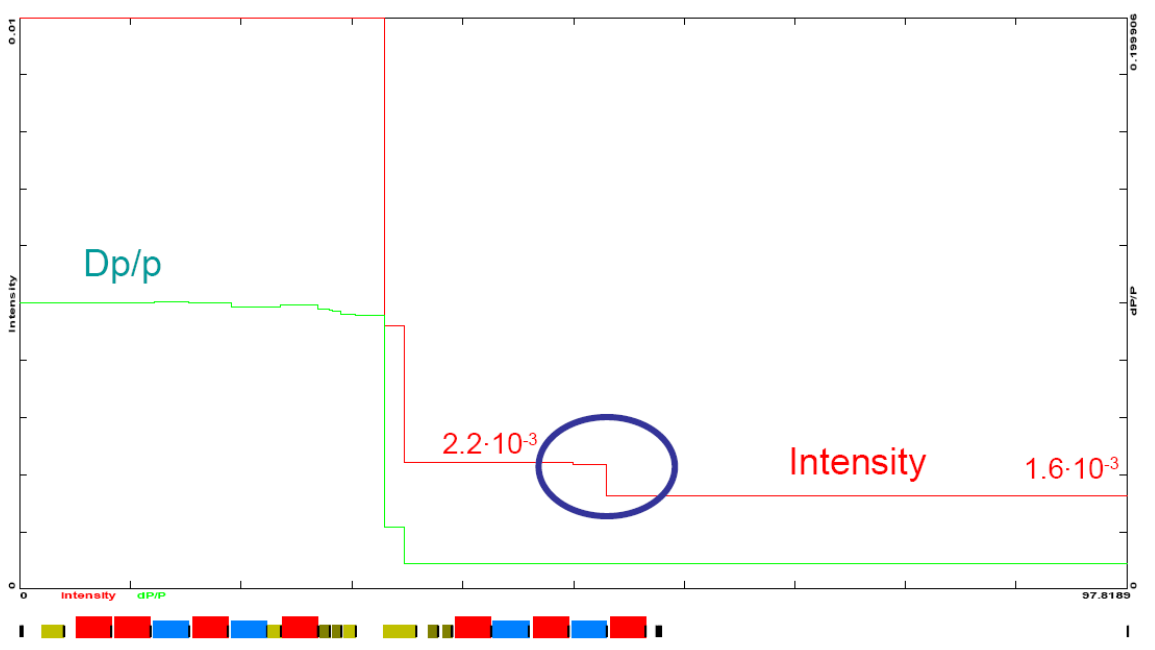


Figure 5.3: An intensity plot created by tracking a very wide (10% sigma dp/p) distribution of particles. OptiM tracking is very simple: a particle is lost if it hits an aperture, so intensity is a step-function. As expected, most particles are lost at the collimator, but a large number of particles that make it through the collimator hit the aperture of the last dipole (the loss highlighted by the oval).

from apertures downstream of the collimator (in the forward beamline), touching every aperture upstream of the collimator and focusing to a 0.25 cm spot at the location of the copper target with zero dispersion. The last 2 requirements are necessary to reflect the reality of particles being produced from a finite-size target. Note that one does not need to mimic angular divergence of the beam at the secondary target because we are intentionally selecting a small subset of secondary particles, cutting the full emittance at the secondary target.

Parameters which can be used to characterize a beam at some location in z are:

- Beam size (x_{max}, y_{max}) ,
- Beam divergence $(\theta_{x,max}, \theta_{y,max})$,
- Beam emittance (ϵ_x, ϵ_y) ,
- Beta functions (β_x, β_y) ,
- Derivative of beta function (α_x, α_y) ,
- Dispersion – only y -dispersion exists (δ_y) ,
- Derivative of dispersion $(d\delta_y/dz)$.

Of course, these parameters are not independent, since for each coordinate we have

$$x_{max}^2 = \epsilon\beta \tag{5.1}$$

$$\theta_{max}^2 = \frac{\epsilon}{\beta}(1 + \alpha^2) \tag{5.2}$$

The primary consideration for choosing the beam parameters at the experimental target was limiting divergence of the beam to 1 mrad, required by the beam Cherenkov counters, and the beam spot size of 2.5 cm – the size of the secondary target. A more subtle factor is that non-dispersive beam lines tend to be more forgiving to errors in the quadrupole gradients and therefore are more stable. Hence the dispersion was chosen to be 0 at the experimental target. Of these parameters, we can chose to vary $x_{x/y,max}, \theta_{x/y,max}, \alpha_{x/y}$, and $d\delta_y/dz$ and search for current settings to satisfy the specified requirements.

An acceptable solution was obtained with $x_{x/y,max} = 1.5$ cm, $\theta_{x,max} = 0.5$ mrad, $\theta_{y,max} = 0.1$ mrad, $\alpha_x = 2$, $\alpha_y = -0.9$, and $d\delta_y/dz = 5 \times 10^{-3}$. Figure 5.4 shows the beta functions and beam envelopes for this reversed beam line. This choice of magnet currents

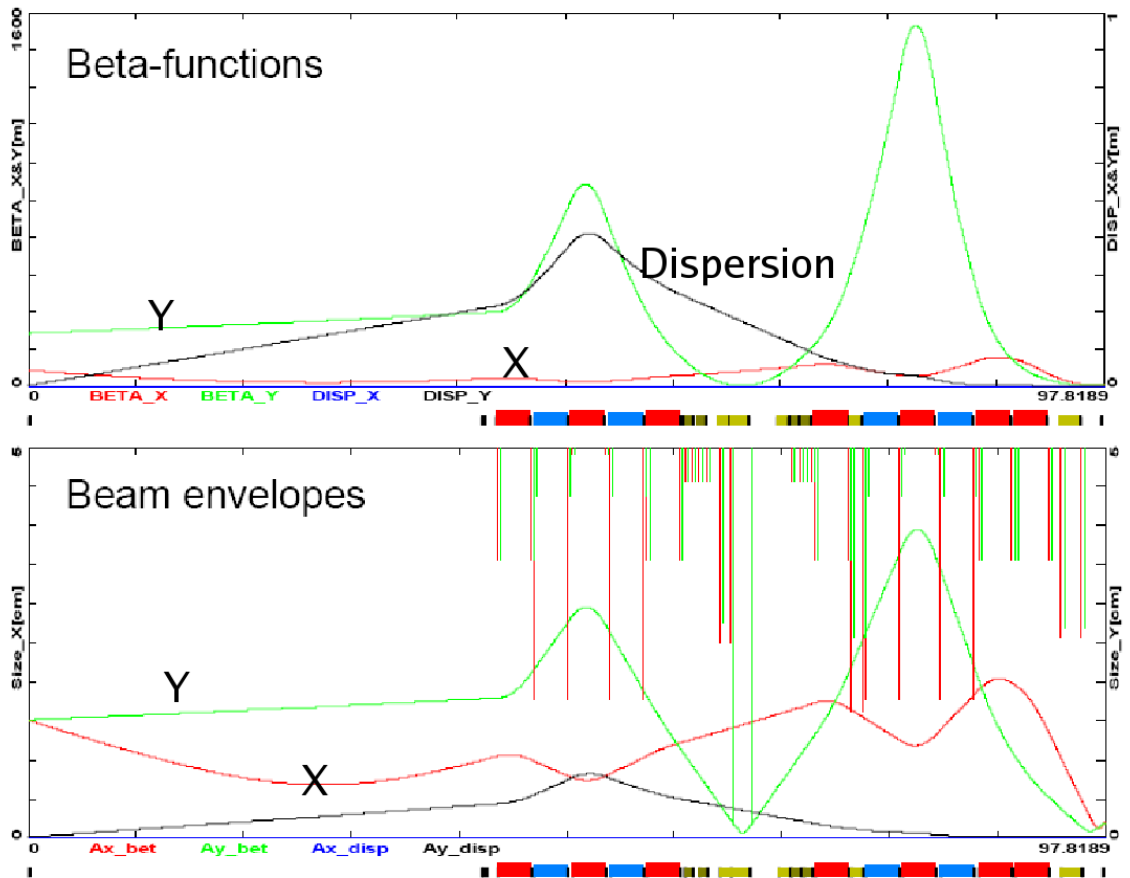


Figure 5.4: The beta functions and beam envelopes for a solution which satisfies the criterion of staying far away from the post-collimator apertures and touching the largest number of apertures upstream of the collimator.

keeps the beam at least 1 mm away from all beam pipes downstream of the collimator, and has the beam envelope “touch” the collimator.

When particles were tracked forward through this solution, not only scraping was greatly reduced, but more particles were getting through (see Figure 5.5). A clear improvement was observed in the quality of experimental data when quadrupole currents derived from this solution were set, and a somewhat refined solution inspired by this modeling was used to set the secondary beam.

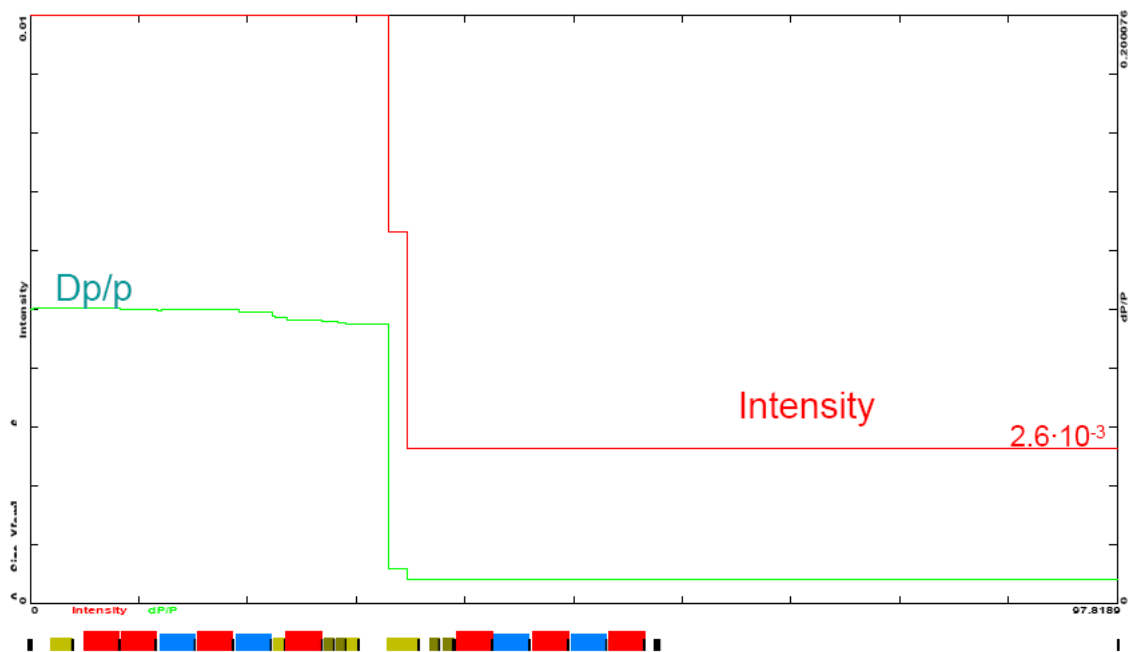


Figure 5.5: Tracking results for beamline settings obtained through the reversed beamline. Unlike the first solution, this one does not show scraping in the fourth dipole magnet.

Chapter 6

Event Reconstruction

6.1 Track Fitting

The overwhelming majority of particle trajectories (tracks) in MIPP are fit either to straight lines or track templates. The approach to both methods is presented in this section.

The task is to fit a 3-dimensional curve to a collection of measurements with different orientations in xy -plane (also referred to as views) at different z locations. Defining measurements this way allows one to easily combine 3-dimensional points computed in the TPC with the 2-dimensional chamber measurements: one simply splits the TPC point into two 2-dimensional measurements.

Our convention is to measure the angle between the wire orientation and the y -axis, so that x -measurements (vertical wires) have $\theta = 0$ and θ is increasing clockwise. To make coordinate u of a given view collinear with the x and y -axis when appropriate, $\theta = -90^\circ$ for y -measurements (horizontal wires). Figure 6.1 shows a diagram of this convention. Then a point (x, y) can be converted to u in a given view through

$$u = x \cos \theta - y \sin \theta. \tag{6.1}$$

6.1.1 Straight Line Fitting

Fitting a straight line to a collection of measurements is easily done through a generalized least squares method. A line in space is described by 6 parameters. We choose to represent the line through the two points at the smallest and the largest z : (x_1, y_1, z_1) and

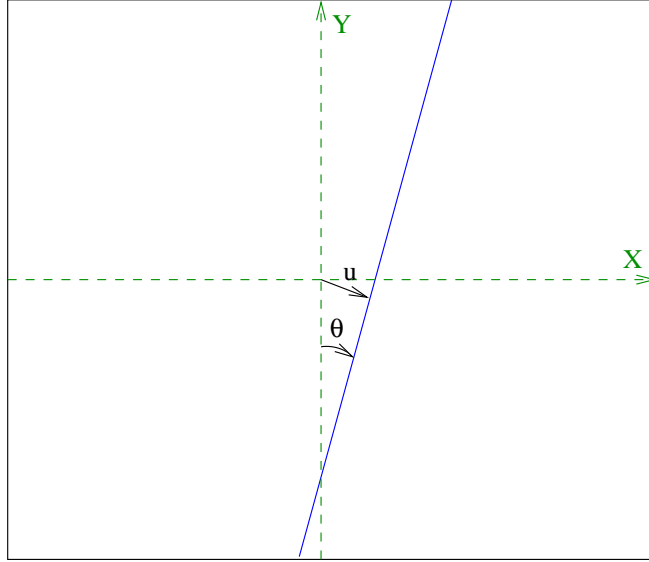


Figure 6.1: Sketch of wire plane geometry.

(x_2, y_2, z_2) . Once the choice of z_1 and z_2 is made, we need to determine the four parameters $\vec{p} = (x_1, y_1, x_2, y_2)$.

At any z , we have

$$\begin{cases} x(z) = \frac{x_1(z - z_2) - x_2(z - z_1)}{z_1 - z_2} \\ y(z) = \frac{y_1(z - z_2) - y_2(z - z_1)}{z_1 - z_2} \end{cases} \quad (6.2)$$

Then using Equation 6.1 we can predict u in a given view at z through

$$u(z; i) = \sum_{j=1,4} c_{ij} p_j, \quad (6.3)$$

where

$$\vec{c}_i = \begin{pmatrix} \frac{z - z_2}{z_1 - z_2} \cos \theta_i \\ \frac{z - z_2}{z_1 - z_2} \sin \theta_i \\ -\frac{z_1 - z_2}{z - z_1} \cos \theta_i \\ -\frac{z_1 - z_2}{z - z_1} \sin \theta_i \end{pmatrix}$$

With N measurements, we write the least squares equation

$$\chi^2 = \sum_{i=1, N} w_i \left(u_i - \sum_j c_{ij} p_j \right)^2, \quad (6.4)$$

where w_i is the weight given to the wire in the track. We seek a solution which minimizes χ^2 , that is

$$\frac{\partial}{\partial p_k} \chi^2 = 2 \sum_N w_i c_{ik} \left(\sum_j c_{ij} p_j - u_i \right) = 0 \quad (6.5)$$

We can rewrite Equation 6.5 as a matrix equation

$$\vec{v} = \mathbf{M}\vec{p}, \quad (6.6)$$

where

$$v_j = \sum_i w_i u_i c_{ij}$$

$$M_{jk} = \sum_i w_i c_{ij} c_{ik}$$

Solving Equation 6.5 gives

$$\vec{p} = \mathbf{M}^{-1}\vec{v},$$

$$\chi^2 = \sum_i u_i w_i^2 - \vec{p} \cdot \vec{v}.$$

Finally, since

$$\frac{1}{2} \frac{\partial^2}{\partial p_i \partial p_j} \chi^2 = M_{ij},$$

i.e. M is the inverse covariance matrix, errors on the track parameters are given by

$$\sigma_{p_i}^2 = M_{ii}^{-1}.$$

6.1.2 Template Track Fitting

When a track traverses regions of space with a significant magnetic field, one needs to determine the track momentum in addition to the location and direction at a given z_0 . If one has a guess at the track parameters and the field is sufficiently smooth, the problem can be solved by fitting the set of measurements to a track template. The advantage of this method is the small required number of swims¹ through the magnetic field. The disadvantage of this method is that the track direction is represented by dx/dz and dy/dz , which are difficult to use when the track angle to the z -axis is large.

¹“Swimming a track” refers to computation of the track trajectory, i.e. the position and direction at various values of z , given the starting position and momentum vectors.

When a charged particle traverses magnetic field, to first order its bend angle and therefore displacement from a straight-line track is proportional to q/p , the charge and momentum of the particle. That is, at a given z , we can represent the particle state with 5 parameters: $Q = q/p$, position (x, y) and direction $(dx/dz, dy/dz)$ at $z = z_0$:

$$\begin{cases} x = x_0 + \left. \frac{dx}{dz'} \right|_{z'=z_0} \cdot (z - z_0) + Q\lambda_x(z) \\ y = y_0 + \left. \frac{dy}{dz'} \right|_{z'=z_0} \cdot (z - z_0) + Q\lambda_y(z), \end{cases} \quad (6.7)$$

where λ_x and λ_y can be interpreted as displacement from straight-line trajectory for a particle with $q/p = 1$ and can be calculated by swimming a track with seed parameters ($Q \neq 0$) from z_0 and setting

$$\begin{cases} \lambda_x(z) = \frac{1}{Q} \left(x_{swim} - x_0 - \left. \frac{dx}{dz} \right|_{z=z_0} \cdot (z - z_0) \right) \\ \lambda_y(z) = \frac{1}{Q} \left(y_{swim} - y_0 - \left. \frac{dy}{dz} \right|_{z=z_0} \cdot (z - z_0) \right). \end{cases} \quad (6.8)$$

When $|dx/dz| < 1$ and $|dy/dz| < 1$ at z_0 and z , the errors from this representation are negligible.

Equipped with Equations 6.7 and 6.8, we need a guess at track parameters to compute $\lambda_{x,y}$ at z of every measurement, and we can reuse the linearized chi squared formalism with

$$\vec{p} = \begin{pmatrix} x(z_0) \\ y(z_0) \\ dx/dz(z_0) \\ dy/dz(z_0) \\ Q(z_0) \end{pmatrix}, \quad \vec{c}_i = \begin{pmatrix} \cos \theta_i \\ -\sin \theta_i \\ (z_i - z_0) \cos \theta_i \\ -(z_i - z_0) \sin \theta_i \\ \lambda_y(z_i) \cos \theta_i - \lambda_x(z_i) \sin \theta_i \end{pmatrix}. \quad (6.9)$$

Notice that if the track template takes energy loss into account, this approach will, to first order, behave correctly if energy loss over the length of the track is small compared to the initial track energy.

6.1.3 Fail Safe Fitting

In case the template track fit is inadequate for a track, the fail-safe method of fitting is to minimize the weighted distance from the measurements to the track using the

ROOT TMinuit package. This approach is slow, but it ensures that even when the track is nearly perpendicular to the z -axis its parameters will be computed correctly. Different weights can be chosen for the x, y, z measurements, corresponding to the different errors on the measurement in the three dimensions.

Given a point (x, y, z) the closest point on the track (x_t, y_t, z_t) is found by minimizing

$$D^2 = w_x(x - x_t)^2 + w_y(y - y_t)^2 + w_z(z - z_t)^2. \quad (6.10)$$

If the track is a straight line, from a point on the track, the step that one needs to take to minimize D^2 is given by²

$$s = \frac{w_x(x - x_t)p_x + w_y(y - y_t)p_y + w_z(z - z_t)p_z}{w_x p_x^2 + w_y p_y^2 + w_z p_z^2}, \quad (6.11)$$

where the unit vector (p_x, p_y, p_z) represents the direction of the track at (x_t, y_t, z_t) . If the track is not a straight line, then one has to repeat the procedure until s is sufficiently small.

6.2 Wire Chambers

The MIPP wire chambers are grouped into 3 triplets (BC123, DC123, DC4/PWC56) with the two magnets separating the triplets. The curvature due to magnetic field is negligible between the magnets as well as before Jolly Green Giant and after Rosie, so that one can reconstruct a straight line segment in each group. Once the segments are found, it is simple to test whether a combination of the DC123 segment with the DC4/PWC56 segment appears to form a reasonable track candidate with momentum obtained from the Rosie kick. Finally, if the track candidate momentum is similar to the beam momentum, one can check whether combining the candidate with the BC123 segment will give a reasonable 9-chamber track.

Having reliable track fits with all 9 chambers was crucial to aligning the chambers and finding inconsistencies in the description of the spectrometer geometry.

6.2.1 Wire Clusters

A wire cluster is defined as either one wire or a group of contiguous wires. In the DCs, we cluster wires only if their hit times are similar and the cluster size is limited to

²If $w_x = w_y = w_z = 1$ Equation 6.11 reduces to dot product of track direction and vector pointing from (x_t, y_t, z_t) to (x, y, z) .

two wires. In PWCs, the cluster size is unlimited.

Chamber preamplifiers and discriminators occasionally ring so that all 8 wires are hit. In those cases, wires from that preamplifier are not used for tracking in order to improve the signal-to-noise ratio.

Once the hit wires are grouped into clusters, the geometric center of each cluster in chamber coordinate system is computed through

$$u_{loc} = D_{plane}(W - W_0), \quad (6.12)$$

where D_{plane} is the wire spacing, and W_0 is the hypothetical wire that goes through $u = 0$ in the chamber reference frame. A point on the wire ($u \cos \theta_{loc}, -u \sin \theta_{loc}, z_{loc}$) is then transformed to global reference frame ($x_{glob}, y_{glob}, z_{glob}$), taking into account the chamber position and rotation. Finally, the global u of the cluster is obtained from (x_{glob}, y_{glob}) through Equation 6.1. Note that at this stage z_{glob} is not a meaningful coordinate if the chamber is rotated about the x or y -axis because we do not know where the hit occurred along the wire.

6.2.2 Wire Crosses

To simplify the track segment pattern recognition, we form 3-dimensional space points from wires in at least 2 different views of each chamber. Having 3D space points enables us to apply the same track finding algorithm to the BC1+BC2+BC3, DC1+DC2+DC3, and DC4+PWC5+PWC6 segments. Wire plane angles (see Table 2.1) are the same for the BCs and DCs – subject to small corrections from alignment – so one could imagine doing 2-dimensional uz -search in the BCs and DCs, but having one algorithm for all triplets of chambers made it easier to maintain the code.

From Equation 6.1, it follows that coordinates of the intersection of two wires is given by

$$\begin{cases} x = \frac{u_1 \sin \theta_2 - u_2 \sin \theta_1}{\cos \theta_1 \sin \theta_2 - \sin \theta_1 \cos \theta_2}, \\ y = \frac{u_1 \cos \theta_2 - u_2 \cos \theta_1}{\cos \theta_1 \sin \theta_2 - \sin \theta_1 \cos \theta_2}. \end{cases} \quad (6.13)$$

If more than two wires belong to a cross, its position can be computed through the least squares approach (Equation 6.4), where

$$\vec{p} = \begin{pmatrix} x \\ y \end{pmatrix}, \quad \vec{c}_i = \begin{pmatrix} \cos \theta_i \\ -\sin \theta_i \end{pmatrix}.$$

Wire crosses are then found with the following algorithm:

1. Calculate the intersection of two wire clusters from different planes which do not belong to a common wire cross and verify that (x, y) is within the active chamber volume.
2. Look for wire clusters consistent with the calculated (x, y) in the remaining two views of the chamber.
3. Fit the position of the wire cross using all available views. If the χ^2 is not acceptable, then choose the 3-plane combination with the better χ^2 .

Once all crosses are found, the crosses which are subset of a different cross are eliminated.

The final step in the algorithm is to compute the number of clusters in each cross that belong to crosses with more clusters. The crosses where all wires are used in larger crosses are typically shadows of valid crosses, and they are not used to seed track segments.

6.2.3 Track Segments

The track segment finding is similar to the wire cross finding: the algorithm evaluates all possible combinations of chamber space points and keeps the ones that contain information from all 3 chambers in a triplet and has an acceptable χ^2 .

For the purpose of segment finding, we define a data structure with the following information:

- Wire crosses in the segment,
- Wire clusters in the segment,
- The minimum and maximum wire time,
- The segment fit parameters as (x_1, y_1, z_1) and (x_2, y_2, z_2) .

A cross/cluster data structure is defined to hold

- The minimum and maximum wire time for cross/cluster,
- The list of segments that the cross/cluster is in.

With the data organized this way, any of the following tests become fast:

- Are two crosses compatible in time?
- Is a cross/cluster compatible in time with an existing segment?
- Are two crosses already part of one segment?
- How many clusters are shared between two segments?

The track finding algorithm follows these steps:

1. Loop over all binary combinations of crosses of every pair of chambers.
2. If the two crosses are compatible in time and are not part of a formed segment, continue to the next step.
3. Fit a 3-dimensional line to the clusters of the two crosses and make a prediction of the position at the third chamber.
4. Given the prediction, find the closest cross or cluster which is compatible in time with the initial crosses. If the newly fit segment has an acceptable χ^2 , go to step 6.
5. Find the closest wire cluster in each view of the third chamber compatible in time with the initial crosses. If no acceptable clusters or more than one cluster is found, go to step 1.
6. If the segment has at least the minimum required number of clusters, save it and update the track list of every cross/cluster.

At the end of the segment search, it is important to filter out essentially duplicate tracks: any track that has less than the required number of unique clusters was not saved.

6.2.4 Chamber Track Candidates

A chamber track candidate is defined as a combination of DC123 and DC4/PWC56 track segments. The track bend in the Rosie magnet enables us to measure momentum of the particle. The search for track candidates is done by matching the predicted position and the dy/dz of the two segments in the center of Rosie. While the windows on the variables are quite wide (12 cm match in x , 10 cm in y , and 5 mrad in dx/dz), they help reduce the combinatorics of possible track candidates before a template track fit is attempted.

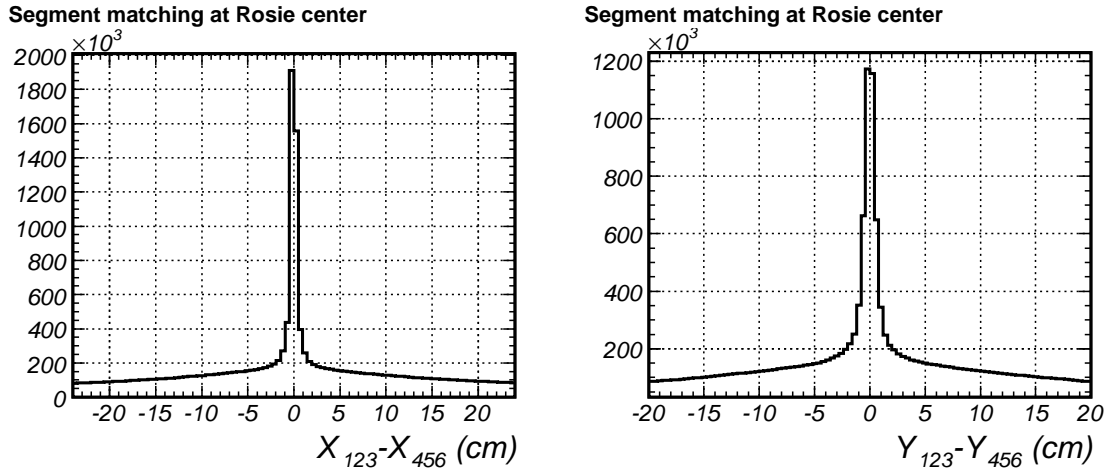


Figure 6.2: Matching of DC123 and DC4/PWC56 segments in the center of Rosie.

A potential pair of segments are first fitted using a 120 GeV/ c particle template. The results of the fit are used to obtain a better template and the track is refit. The track is accepted or rejected based on the χ^2 of the second fit (see Figure 6.3).

The final step of the algorithm is to attempt to match the track with the BC123 track segment. Obviously wrong candidates are filtered out by requiring that the charge of the candidate match the charge of the beam particles in the run, and that the momentum be at least 0.8 of the beam momentum. The decision on whether to keep the track candidate as a 6-chamber or a 9-chamber object is made based on the χ^2 of the resulting track.

6.3 Time Projection Chamber

The TPC dominates the event size and is the most complex detector to reconstruct. The primary problems facing track reconstruction in the TPC are

- Large dead sections of the detector;
- 16 μs integration time, which makes the TPC very sensitive to out-of-time tracks.

The reconstruction algorithm is adopted from the algorithm used by the BNL E910[44]. MIPP-specific aspects of the algorithm are documented in [37]. The main steps of the algorithm are:

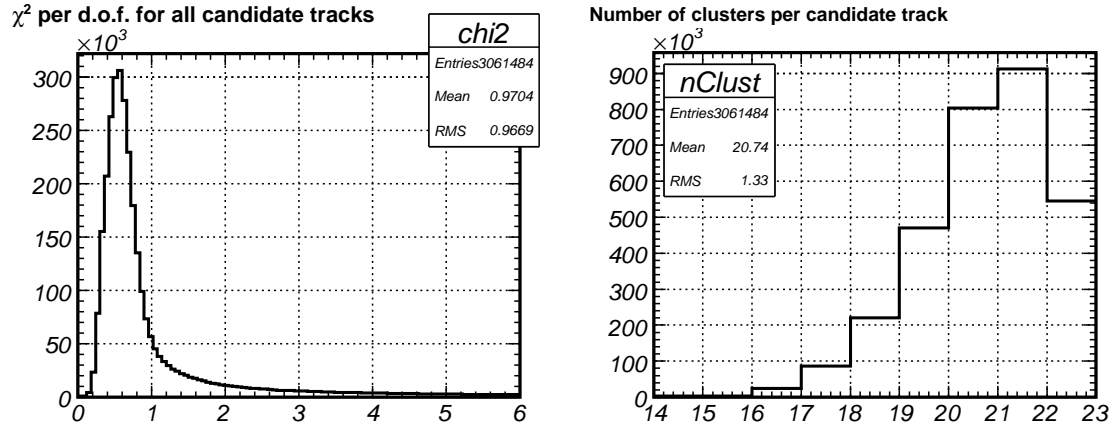


Figure 6.3: The distribution of χ^2 per degree of freedom and the number of clusters in chamber track candidates.

1. Create two-dimensional contiguous clusters in each pad row (z -slice) of the TPC. Each cluster is fitted to a Gamma function in t : $q(t) = At^\lambda e^{-t}$, and a Gaussian in x . For hits with less than 3 pad columns, the position in x is calculated through weighted mean, using charge collected on the pad as the weight.
2. Calculate the hit position by computing the electron trajectory starting from the TPC anode plane (see Section 7.5.2).
3. Search for tracks using what amounts to a simplified Kalman filter approach. Starting from the downstream end of the chamber – where the tracks are best separated – a track is formed by connecting the closest hits in the neighboring pad rows. The track is then extended and a position prediction is made in the next pad row. Acceptable hits are added into the track until no new hits are found in the upstream direction. The hit search is then reversed to pick up hits in the downstream direction.
4. Similar tracks – those that share a large fraction of their hits – are merged to remove essentially duplicated tracks.

6.4 Global Tracking

The objectives of global tracking are

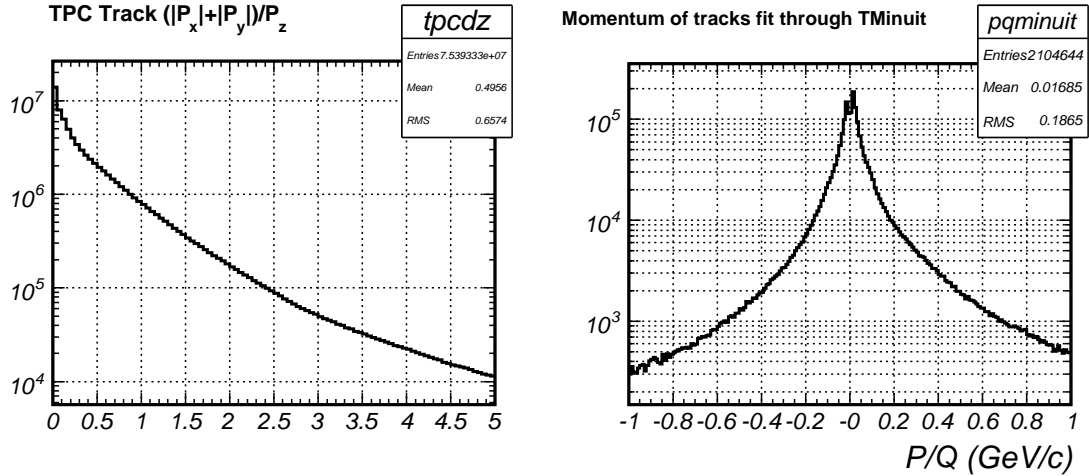


Figure 6.4: Ratio for selecting tracks which are to be fit through the TMinuit and momenta of those tracks.

1. To refit the TPC tracks using the measured JGG magnetic field map;
2. To combine the TPC tracks with the chamber track candidates, track segments, or stand-alone wire clusters.

6.4.1 Refitting TPC tracks

If the track angle with respect to the z -axis is small, the template track fit approach is adequate to refit the TPC track. However, if the track angle to z -axis is large, template fitter is not able to handle it adequately, and the track is passed to the fail-safe TMinuit fitter. The selection of the fitter is based on two criteria:

1. The ratio $(|P_x| + |P_y|)/P_z$ in the middle of the track, at $\frac{1}{4}$ and $\frac{3}{4}$ of z along the track;
2. The number of pad rows in the track.

Tracks with the ratio above 4 and tracks that span fewer than 4 pad rows, are not attempted to be fit to a track template. The tracks selected for the slow fitter are predominantly low momentum tracks (see Figure 6.4).

In either fitter the track parameters are computed in the middle of the track. This way potential problems with very large dx/dz or dy/dz at z_0 are minimized. Seed track parameters are extracted from the helical fit with the momentum computed using the track curvature under the assumption of a homogeneous magnetic field.

In the event that the template fitter cannot reswim the track from the first hit to the last hit, the template fitting is considered to have failed, and the track is passed to the TMinuit fitter.

6.4.2 Cleaning up TPC Tracks

The TPC reconstruction algorithm has two minor problems which result in tracks with a very large χ^2 :

- Two nearby tracks can be merged together;
- The track finding algorithm can pull in hits that are inconsistent with the rest of the hits on the track.

To alleviate these problems, we take the following approach. Hits are removed from the track until its χ^2 per degree of freedom is under 2. Then we continue to remove those hits which contribute more than 8 times than the average contribution to χ^2 . This approach cleans up TPC tracks without sacrificing well reconstructed tracks.

6.4.3 Merging Tracks

Prior to fitting the TPC tracks using the magnet field map, tracks are merged using a more sophisticated approach than just looking at the number of shared TPC and wire chamber hits. The similarity of tracks is judged by computing a “cross χ^2 ” as the sum of weighted residuals squared of one track using the parameters of another track. If the goodness of fit based on cross χ^2 is larger than 0.1 or the ratio of the first track’s χ^2 to cross χ^2 is larger than 0.15, then the tracks are merged together.

6.4.4 Matching TPC Tracks to Chambers

Global tracks – those including TPC and chamber information – are formed by first attempting to match the TPC tracks to the chamber track candidates at DC1. If a matching candidate is not found, then a matching DC123 segment is searched for. If a segment is not found, then we search for the nearest wire clusters in DC1, DC2, and DC3, refitting the track when the new information is added into the track. If the predicted track position at a chamber is outside of the active area of the chamber, then no attempt is made to extend the track further. For tracks that are extended to DC3, the process continues in

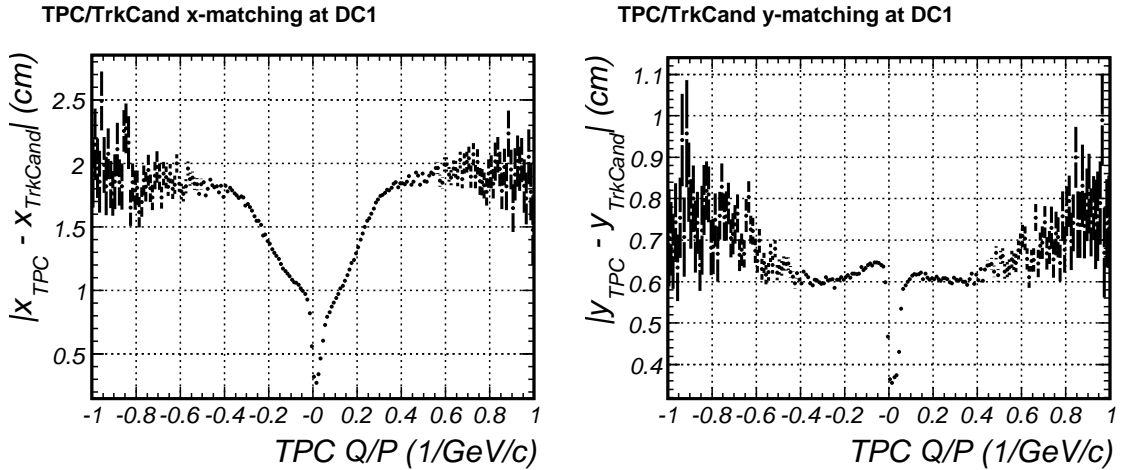


Figure 6.5: The dependence of position matching of the TPC and chamber track candidates when position is computed at DC1.

downstream chambers, first searching for matching C456 track segments and descending to the level of wire clusters if it is necessary.

6.4.5 Tracks in the Event Stream

Saving only track measurements and parameters to the event stream has the potential of slowing down analysis modules that need the tracks to predict the state of the particle at various z along the spectrometer. The waste of CPU time would come from the need to recompute the trajectory multiple times. Third order interpolation which matches the position and the track direction at the two adjacent points is implemented to make trajectory prediction without reswimming the track. While the global tracking module still has the states of the swum track in memory, more points are inserted in the middle of two neighboring points so that third order prediction at $1/4$, $1/2$, and $3/4$ distance in z is within 100 micron of the swim prediction. This accuracy is sufficient for all modules which use the tracking results.

6.5 Vertex Reconstruction

Identifying the primary and decay vertices is essential for the data analysis. Vertex position tells us where the track came from. In addition the track momentum and position resolution are improved when a vertex-constrained fit is done. The vertex reconstruction is

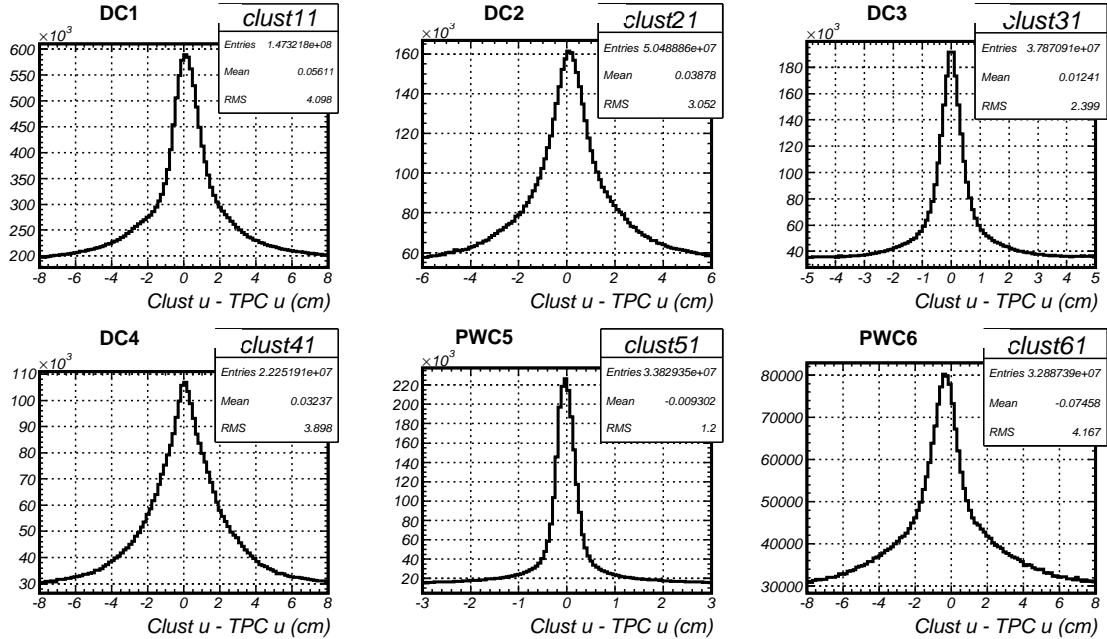


Figure 6.6: Matching of tracks at the six chambers. Notice that the x -axis scales are different.

split into two parts: vertex finding and vertex-constrained track fitting.

6.5.1 Vertex Finding

One of the difficulties in finding vertices is the fact that beam conditions were not always clean. The algorithm that works well is based on a deterministic annealing filter (DAF).

Using TMinuit, we can fit for the point which minimizes the weighted distance squared to all tracks in the event (See Equation 6.10). The filter helps select the tracks associated with the vertex by reducing the weight of the outliers with

$$w_{DAF} = \frac{1}{1 + \exp\left(\frac{D_i^2 - R_c^2}{2T_{DAF}}\right)}, \quad (6.14)$$

where D_i is the distance to the track from the vertex, D_c is the filter critical radius, and T_{DAF} is the temperature. As the temperature is decreased, the weights of the outliers are reduced while the weights of the tracks with $D_i^2 < D_c^2$ are not affected. Figure 6.7 shows the weight function for the temperature schedule used by our vertex finder.

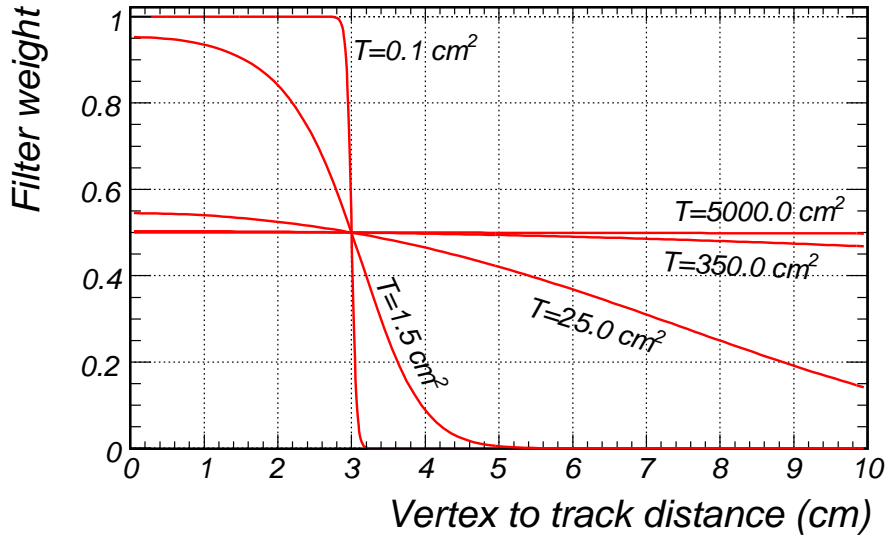


Figure 6.7: The deterministic annealing filter weight function for the temperatures used for the vertex finder.

When the temperature is reduced sufficiently slowly, the filter converges on the most significant vertex even if multiple vertices exist in the event. The tracks that are included into the vertex are excluded from the available track list and the process is repeated until no vertices are found.

In the events where the only two tracks are the incoming beam track measured by the BCs and the same track measured by the TPC and the drift chambers, we find that when the temperature is lowered to 25 cm^2 , it is necessary to repeat the procedure at the same temperature so that the fitted vertex position would prefer to land in the middle of the two tracks rather than exclude one of them completely.

6.5.2 Vertex Constrained Fitting

Fitting a vertex with N particles involves determining $3(N + 1)$ parameters: the vertex position (x_v, y_v, z_v) , and the track directions and momenta $(dx_i/dz, dy_i/dz; q/p_i)$. Template track fitting can be easily linearized for all parameters except z_v if the template coefficients are assumed not to vary with x_v and y_v . Following the conventions set in

Equations 6.1 and 6.7, we now write vertex χ_v^2 as

$$\chi_{vtx}^2 = \sum_{i=1}^N \sum_{j=1}^{n_i} w_{ij} \left\{ \left[x_v + \frac{dx_i}{dz}(z_{ij} - z_v) + Q_i \lambda_{x,i}(z_{ij}) \right] \cos \theta_{ij} - \left[y_v + \frac{dy_i}{dz}(z_{ij} - z_v) + Q_i \lambda_{y,i}(z_{ij}) \right] \sin \theta_{ij} - u_{ij} \right\}^2. \quad (6.15)$$

Here N is the total number of tracks in the vertex and n_i is the number of measurements associated with the i -th track. It is the product of z_v and dx_i/dz that prevents us from being able to linearize the fit for z_v . With z_v held fixed, our solution must satisfy:

$$0 = \frac{\partial}{\partial p_i} \chi_{vtx}^2 = \mathbf{M} \vec{p} - \vec{v}. \quad (6.16)$$

If we define a vector of constants as in Equation 6.9

$$\vec{c}_{ij} = \begin{pmatrix} \cos \theta_{ij} \\ -\sin \theta_{ij} \\ (z_{ij} - z_v) \cos \theta_{ij} \\ -(z_{ij} - z_v) \sin \theta_{ij} \\ \lambda_{x,i}(z_{ij}) \cos \theta_{ij} - \lambda_{y,i}(z_{ij}) \sin \theta_{ij} \end{pmatrix},$$

then

$$\vec{p} = \begin{pmatrix} x_v \\ y_v \\ dx_1/dz \\ dy_1/dz \\ Q_1 \\ \cdot \\ \cdot \\ dx_N/dz \\ dy_N/dz \\ Q_N \end{pmatrix} \quad \vec{v} = \begin{pmatrix} \sum_{ij} w_{ij} u_{ij} c_{1,ij} \\ \sum_{ij} w_{ij} u_{ij} c_{2,ij} \\ \sum_j w_{1j} u_{1j} c_{3,1j} \\ \sum_j w_{1j} u_{1j} c_{4,1j} \\ \sum_j w_{1j} u_{1j} c_{5,1j} \\ \cdot \\ \cdot \\ \sum_j w_{Nj} u_{Nj} c_{3,Nj} \\ \sum_j w_{Nj} u_{Nj} c_{4,Nj} \\ \sum_j w_{Nj} u_{Nj} c_{5,Nj} \end{pmatrix} \quad \mathbf{M} = \begin{pmatrix} \mathbf{A}_0 & \mathbf{A}_1 & \dots & \mathbf{A}_N \\ \mathbf{A}_1^T & \mathbf{B}_1 & 0 & 0 & 0 \\ \dots & 0 & \dots & \dots & \dots \\ \dots & \dots & \dots & \dots & \dots \\ \mathbf{A}_N^T & 0 & \cdot & 0 & \mathbf{B}_N \end{pmatrix}. \quad (6.17)$$

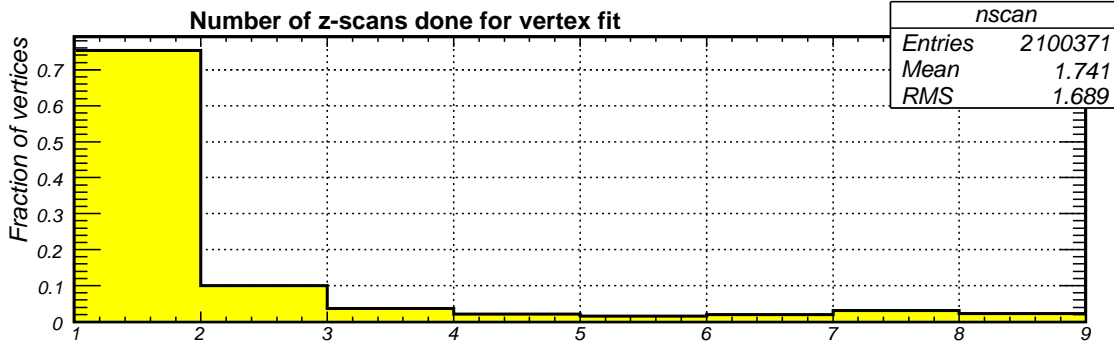


Figure 6.8: The number of z scans required for a vertex constrained fit.

The symmetric matrix \mathbf{M} is made up of the following matrices:

$$\mathbf{A}_0 = \begin{pmatrix} \sum_{ij} w_{ij} c_{1,ij}^2 & \sum_{ij} w_{ij} c_{1,ij} c_{2,ij} \\ \sum_{ij} w_{ij} c_{1,ij} c_{2,ij} & \sum_{ij} w_{ij} c_{2,ij}^2 \end{pmatrix},$$

$$\mathbf{A}_i = \begin{pmatrix} \sum_j w_{ij} c_{1,ij} c_{3,ij} & \sum_j w_{ij} c_{1,ij} c_{4,ij} & \sum_j w_{ij} c_{1,ij} c_{5,ij} \\ \sum_j w_{ij} c_{2,ij} c_{3,ij} & \sum_j w_{ij} c_{2,ij} c_{4,ij} & \sum_j w_{ij} c_{2,ij} c_{5,ij} \end{pmatrix},$$

$$\mathbf{B}_i = \begin{pmatrix} \sum_j w_{ij} c_{3,ij} c_{3,ij} & \sum_j w_{ij} c_{3,ij} c_{4,ij} & \sum_j w_{ij} c_{3,ij} c_{5,ij} \\ \sum_j w_{ij} c_{4,ij} c_{3,ij} & \sum_j w_{ij} c_{4,ij} c_{4,ij} & \sum_j w_{ij} c_{4,ij} c_{5,ij} \\ \sum_j w_{ij} c_{5,ij} c_{3,ij} & \sum_j w_{ij} c_{5,ij} c_{4,ij} & \sum_j w_{ij} c_{5,ij} c_{5,ij} \end{pmatrix},$$

and \mathbf{A}_i^T is the transpose of \mathbf{A}_i .

Thus, the solution is given by

$$\vec{p} = \mathbf{M}^{-1} \vec{v}.$$

In order to determine z_v , we scan around the seed value of the vertex, and compute z_v and the error on z_v from a parabolic fit to the 5 points around the minimum. In practice, since the track template coefficients do change with vertex location, until the computed minimum is within 5 cm of the z -coordinate where the template coefficients were evaluated, we continue the scan with template coefficients re-evaluated at the new minimum. Most vertex z positions returned by the DAF vertex finder are sufficiently good, so that only one scan is required to fit the vertex z .

6.5.3 Fixing Track Momentum in the Vertex Fit

The central momentum of the beam tracks can be measured very well, and the typical spread in momentum is less than 3%. Therefore in vertex-constrained fits, the momentum of beam tracks should not be varied lest we introduce an error into determination of the beam track parameters. The algorithm outlined above is easily modified to fix the momentum of one or more tracks by changing the matrices \mathbf{A}_i and \mathbf{B}_i to

$$\mathbf{A}_i = \begin{pmatrix} \sum_j w_{ij} c_{1,ij} c_{3,ij} & \sum_j w_{ij} c_{1,ij} c_{4,ij} \\ \sum_j w_{ij} c_{2,ij} c_{3,ij} & \sum_j w_{ij} c_{2,ij} c_{4,ij} \end{pmatrix},$$

$$\mathbf{B}_i = \begin{pmatrix} \sum_j w_{ij} c_{3,ij} c_{3,ij} & \sum_j w_{ij} c_{3,ij} c_{4,ij} \\ \sum_j w_{ij} c_{4,ij} c_{3,ij} & \sum_j w_{ij} c_{4,ij} c_{4,ij} \end{pmatrix},$$

and replacing the relevant part of the vector \vec{v} with

$$v_i = \begin{pmatrix} \sum_j w_{1j} (u_{ij} - Q_i c_{5,ij}) c_{3,ij} \\ \sum_j w_{1j} (u_{ij} - Q_i c_{5,ij}) c_{4,ij} \end{pmatrix}.$$

Otherwise, no changes to the algorithm are required.

6.5.4 Limitations of Vertex Fitting

The vertex finder clusters tracks within ± 3 cm of the vertex position. This means that nearby secondary vertices may get erroneously pulled into the primary vertex. The two problems that arise are the pull on vertex position that the incorrect tracks will have and the incorrect conclusion that the extra particles come from the vertex rather than from a neutral decay.

The current implementation of the vertex fitter splits the vertex only to require that the RMS of track times (as measured by the drift chamber wire hits) is below 20 ns. This cleans up pileup, but does not do anything to tracks otherwise incorrectly associated with a vertex.

The resolution of the vertex z (see Figure 6.9) is inferior to the 2 mm sigma resolution that was obtained by the BNL E910 experiment. The primary reason is thought to be the imperfect understanding of the distortion corrections due to the non-uniform JGG magnetic field. The uniformity of the magnetic field in E910 was significantly better so that corrections of order 1 mm were required[41]. In practice, poor vertex resolution in z makes

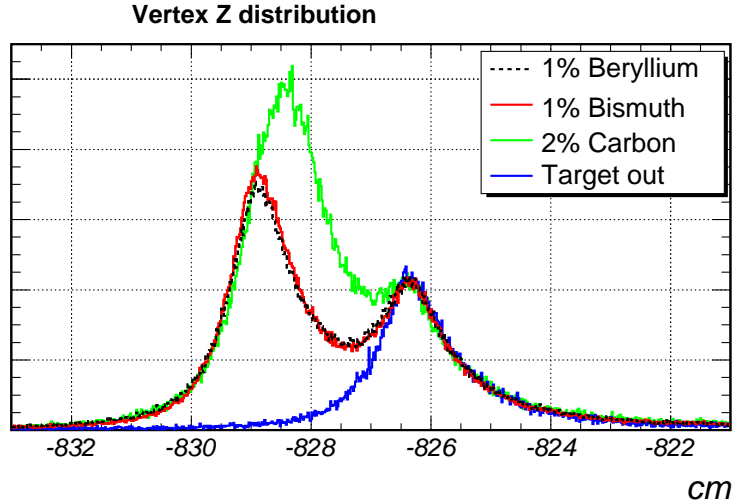


Figure 6.9: The distribution of the fitted vertex z from the three different targets and the target-out configuration. The histograms were normalized to have the same height as the interaction trigger counter. Excluding the long tails, the resolution on vertex z is approximately 13 mm FWHM.

target-out subtraction somewhat more important, but does not have a large effect on the analysis presented here.

6.6 Particle Identification

Particle identification is done using different detectors. Since this work is focused on the high momentum end of the spectrum, the reconstruction algorithm of the RICH is described here.

6.6.1 Particle Identification Methods

Given a track that passes through the RICH radiator volume, there are two approaches to determining the particle identity (PID):

1. Calculate the ring radius and convert the radius and the track momentum into particle mass;
2. Calculate the likelihood for electron, muon, pion, kaon, proton hypotheses and select the PID of the hypothesis with the largest likelihood.

For most momenta of interest, the two approaches give nearly identical results, as one would expect by looking at Figure 6.17. The first method has the advantage of being faster, but it does not take the dispersion of the radiator gas into account. The second method is slower, but has the capability of improving the separation at high momenta where the difference between the $\pi/K/p$ Cherenkov angles is less than the total thickness of the ring. However, this improvement can only be obtained when the detector is very well calibrated. This work is based on the calculation of ring radii, and is adequate for momenta where pion and kaon statistics are significant.

6.6.2 Fitting Ring Radius

The algorithm to fit the ring radii is based on a deterministic annealing filter (see Section 6.5.1) coupled to the hit sharing algorithm proposed for the HERA-B RICH [42].

While the algorithm does not take into account the effect of dispersion of CO_2 in detail, the RMS width of the ring as a function of ring radius is taken into account. Figure 6.10 shows that RMS of the light distribution can be modeled by a simple function for $r > 9$ cm:

$$\sigma(r) = C \cdot (r)^{-a}, \quad (6.18)$$

where r and $\sigma(r)$ are measured in centimeters, $C = 23.78$ and $a = 1.044$. For $r \lesssim 9$ cm, the number of photoelectrons starts dropping as the photons for higher wavelengths go below the Cherenkov threshold. In order to allow the algorithm to converge to radii below 9 cm, the width associated with the ring was modeled as

$$\sigma(r) = \begin{cases} C \cdot r_{crit}^{-a}, & r \leq r_{crit} \\ C \cdot r^{-a}, & r > r_{crit} \end{cases} \quad (6.19)$$

Looking at the index of refraction and the PMT efficiency as a function of wavelength of light, one cannot expect that the function of expected photoelectrons versus radius to be Gaussian. However for simplicity, the weight of each PMT given the ring radius is taken as

$$w_i(r) = \frac{(r - r_i)^2}{\sigma^2(r)}. \quad (6.20)$$

The first step is to select all in-time tracks with non-zero path lengths through the CO_2 and predicted ring centers within the maximum (electron) ring radius from the PMT array. For each ring hypothesis, we compute the number of hits within the active region –

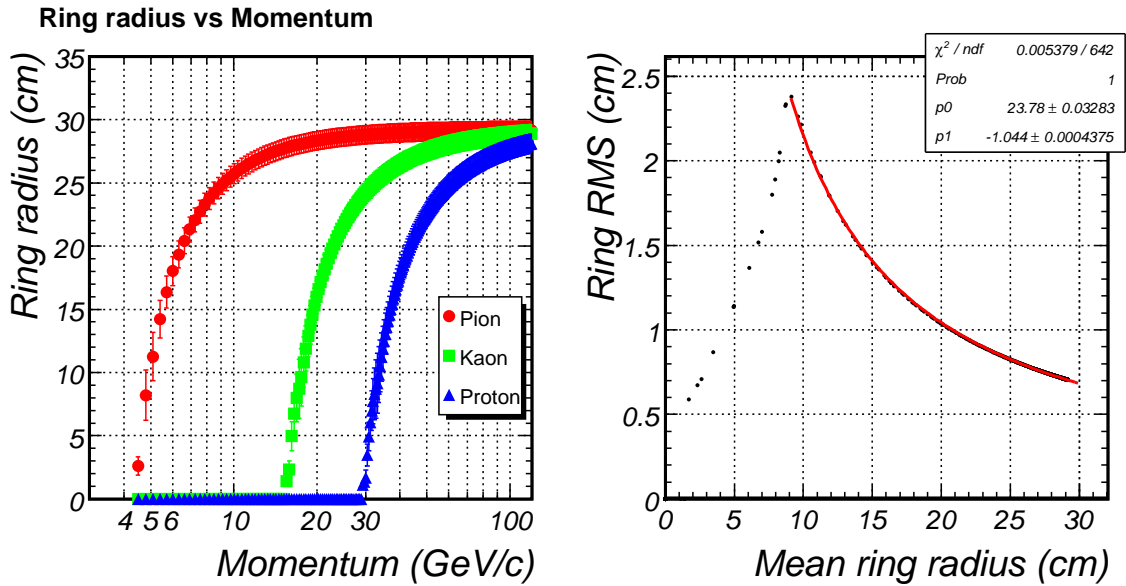


Figure 6.10: Computed pion, kaon, and proton mean ring radii and the RMS of light distribution on the ring.

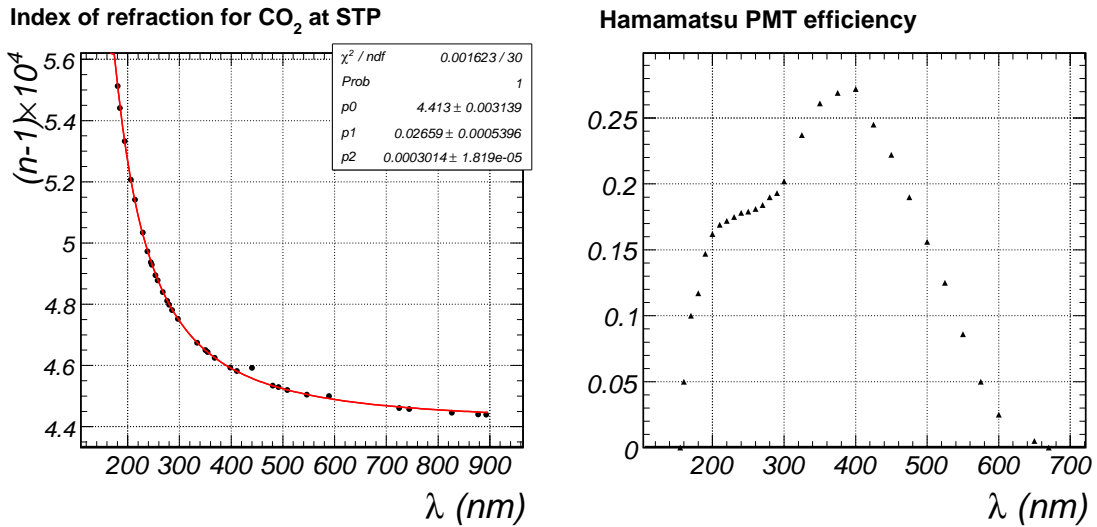


Figure 6.11: Data for the CO₂ index of refraction at STP and the efficiency of Hamamatsu PMTs (efficiency shape of FEU PMTs is similar but about a factor of 2 lower). The index of refraction is well represented by $(n - 1) \cdot 10^4 = 4.413 + 2.66 \cdot 10^{-2} \cdot \lambda^{-2} + 3.01 \cdot 10^{-4} \cdot \lambda^{-4}$ where λ is in μm .

defined by the electron ring radius with a 5 cm safety margin. Any track with less than 3 hits in the active region is dropped from the track list.

To determine the seed ring radius, we scan the sum of $w_i(r)$ for radii from 2.5 cm up to the maximum radius in steps of $\sigma(r)$ and select the radius which gives the smallest sum. To limit the effect of outliers, the weight of hits is limited to σ_{max}^2 . Section 6.6.3 explains why $\sigma_{max} = 3.7$ was chosen.

Equipped with the predicted ring radius, we iterate over the DAF temperature cycle with the following algorithm:

1. Compute $\sigma_{max}(r)$, where r is the current guess of the ring radius. It is important not to vary σ_{max} as r changes because that forces the minimization to converge to a smaller radius and produces wider distribution of ring radii.
2. Compute the filter hit weight. The DAF critical radius is taken as σ_{max}^2 .
3. Compute the hit occupancy $o_{i;j}$ in each ring, which is defined as the number of PMTs that fall into the same radius bin of j -th track. 0.4σ bins were used.
4. Fit each ring radius allowing the ring center position to vary if at least 6 hits are associated with the ring. Each hit weight is modified as

$$w_{i;j} = w_i(r) \cdot w_{DAF} \cdot \frac{o_{i;j}}{\sum_j o_{i;j}},$$

thus the total weight of each hit in the event is 1, but varies in different tracks so that hit sharing is taken into account.

The DAF temperature cycle of (5, 1, 0.2, 0.04) cm² works well even in busy events. At the end of the cycle, hit usage is computed with a 0 cm² DAF critical radius where hits with weight larger than 0 are considered to be used by the algorithm. Rings that had less than 2 non-shared hits were interpreted to come from noise and were assigned $r = 0$.

6.6.3 Choosing σ_{max}

The DAF critical radius parameter σ_{max} dictates the signal region for a given ring radius. There are two considerations that must be taken into account to select its value. On the one hand, the region should be sufficiently large to include all hits that come from the ring. On the other hand, very large σ_{max} will make the algorithm more susceptible to noise.

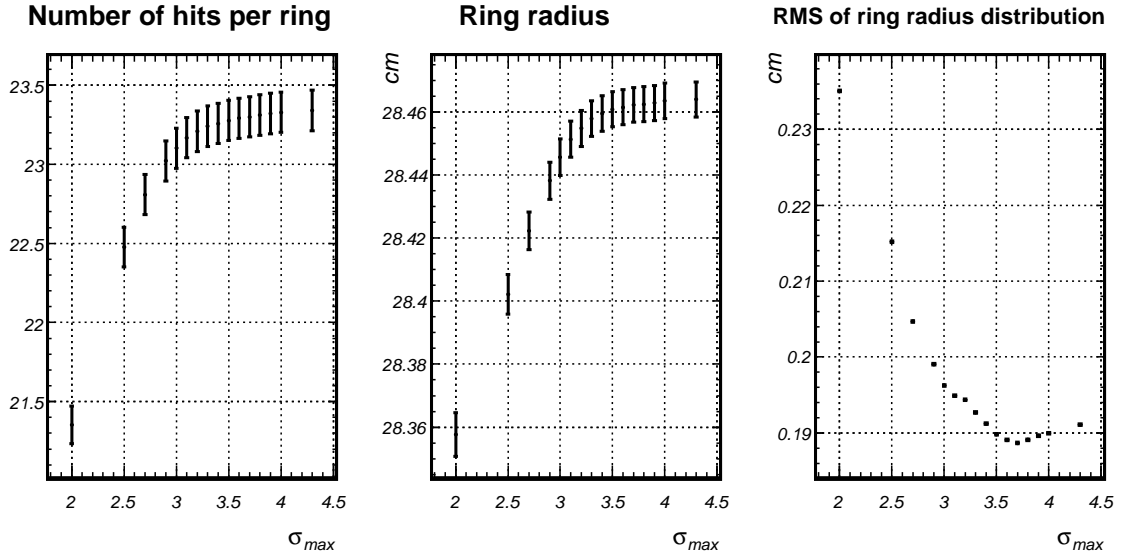


Figure 6.12: Effect on the proton ring fits by different choices of σ_{max} (see text for explanation).

Figure 6.12 shows how the proton ring fits are affected by the choice of the ring signal region. We see that smaller values of σ_{max} prevent the algorithm from using all of the available information for the ring fit, resulting in fewer hits per ring, smaller radius, and larger width of the ring distribution. As σ_{max} is pushed past 3.7, the potential for picking up noise is higher, resulting in a somewhat larger width of the proton ring distribution.

6.6.4 Incorrectly Fit Rings

A feature of the algorithm is that it will preferentially go for hits inside the signal region, whether those hits were generated by noise or the particle Cherenkov light. There are two predictable ways in which the algorithm incorrectly fits a ring

1. The ring center gets shifted far away from predicted position;
2. Fit maximally allowed ring radius, well above electron ring radius.

Minimization is done with limits on the ring radius and displacement of the ring center from the prediction. momentum dependent window is chosen to limit the ring center shift:

$$D_{x,y} = \begin{cases} C_{x,y}/p_{tot}, & p_{tot} < 120 \\ C_{x,y}/120, & p_{tot} \geq 120 \end{cases} \quad (6.21)$$

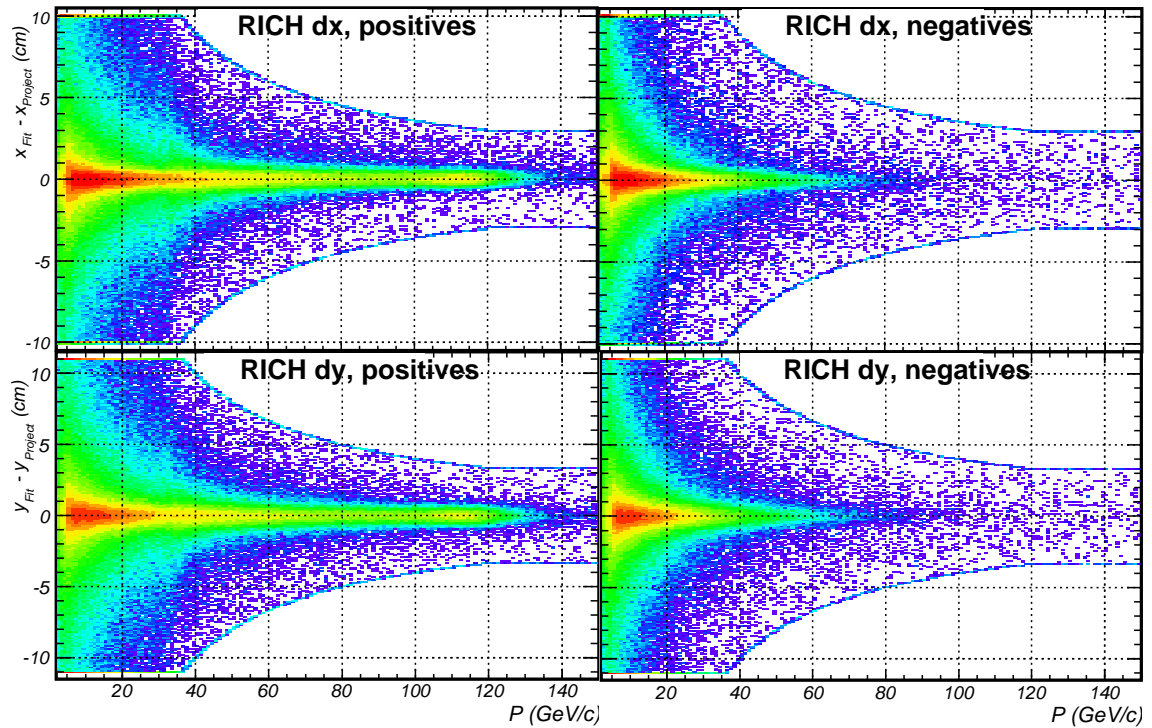


Figure 6.13: Distributions of the ring center displacement in x and y by the fit from the prediction made from the track parameters.

where $C_x = 360 \text{ cm GeV}/c$, $C_y = 400 \text{ cm GeV}/c$, and p_{tot} is the momentum of the track. The choice is motivated by the effects of multiple scattering, since the track position and angle predictions are more reliable for the higher momentum tracks. Finally, D_x is limited to 10 cm and D_y to 11 cm so that the ring is less likely to “walk” into another ring potentially causing two incorrectly fit rings.

6.6.5 Corrections to Ring Radius

When the RICH was repaired after the accident, every fourth PMT column was left empty to provide a uniform coverage of the PMT array. This creates aliasing in ring fits due to regularly missing information. The effect on ring fits can be observed by scanning over the pion ring radius selecting particles in a narrow band of momentum so that the predicted ring radius does not change by more than $\pm 0.1 \text{ cm}$. Figure 6.14 shows that the observed ring radius depends on the mean value of ring radius and the x -coordinate of the

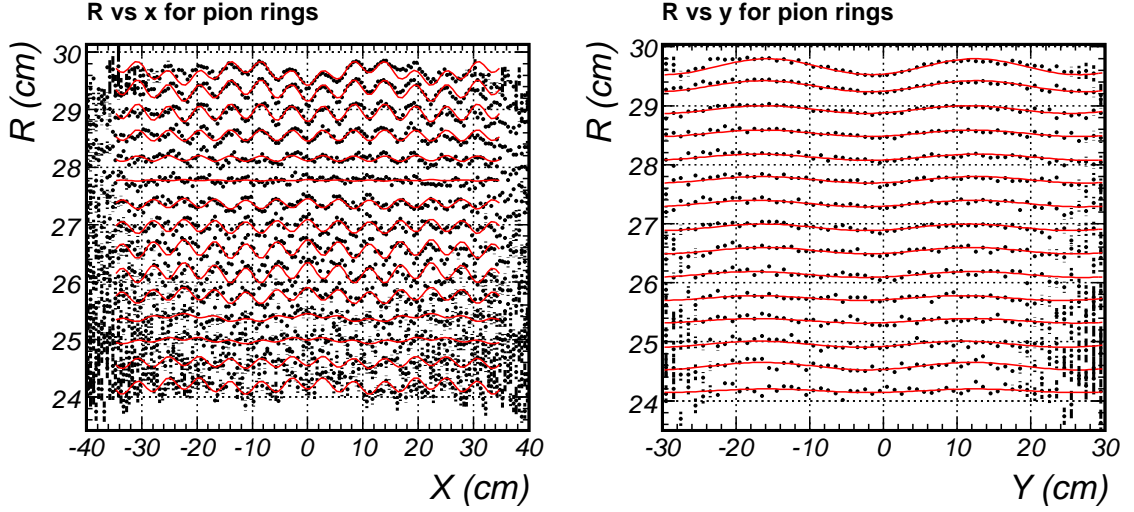


Figure 6.14: Ripples in the measured RICH ring radius due to aliasing. The binned histograms show the result from a scan of pion rings in 4 mm steps of the central ring radius.

ring center. The period of the sinusoidal variations is 5.5 cm – the distance between four PMT columns.

These ripples in the measured radius can be parametrized through

$$\delta R_x(x, R) = A_{x0}(R) \cos(\omega_x x) + A_{x4}(R) \cos\left(\frac{\omega x}{4}\right), \quad (6.22)$$

$$\delta R_y(y, R) = A_y(R) \cos(\omega_y y + \phi). \quad (6.23)$$

The lower frequency correction in x as well as the correction in y result from a systematic difference in the ring radius when a portion of the ring is no longer detected by the photomultipliers as the ring center shifts away from the center of the PMT array. As Figure 6.15 shows, we find that the amplitude $A_{x0}(R)$ is well described by $A_0 \sin(\omega R)$. This corroborates the statement that the ripples result from geometric aliasing.

Ripple corrections are most important for the high radius rings since at high momenta the difference in ring radii of protons, kaons, and pions becomes small. Figure 6.16 shows that for high momentum pions the effect is a $\sim 10\%$ improvement in the RMS of ring distribution.

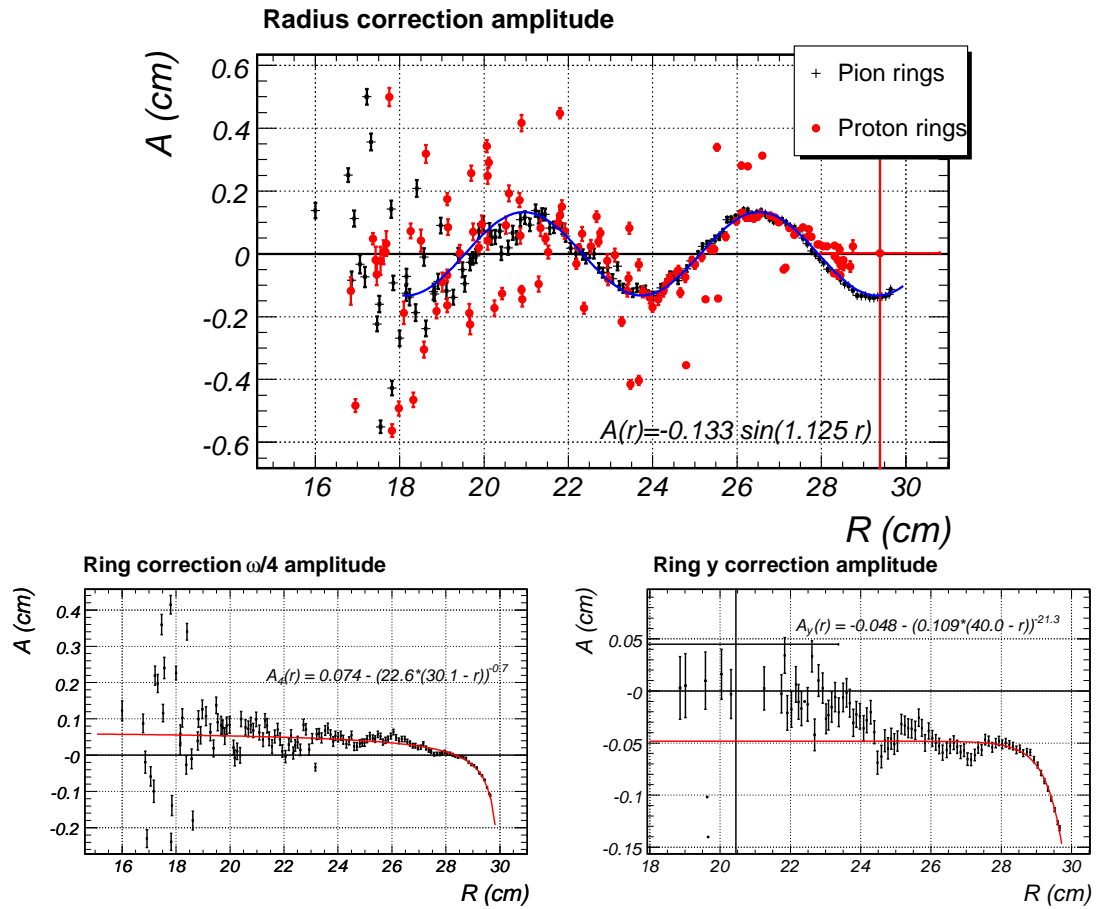


Figure 6.15: Results of fits to the amplitude of the ring radius ripples as a function of the selected ring radius. As a sanity check, the scan was repeated for proton rings to verify that the effect is not specific to pion rings. The fact that amplitude of the dominant oscillation in x is consistent with $\sin(\omega_x R)$ confirms that the effect is purely geometric.

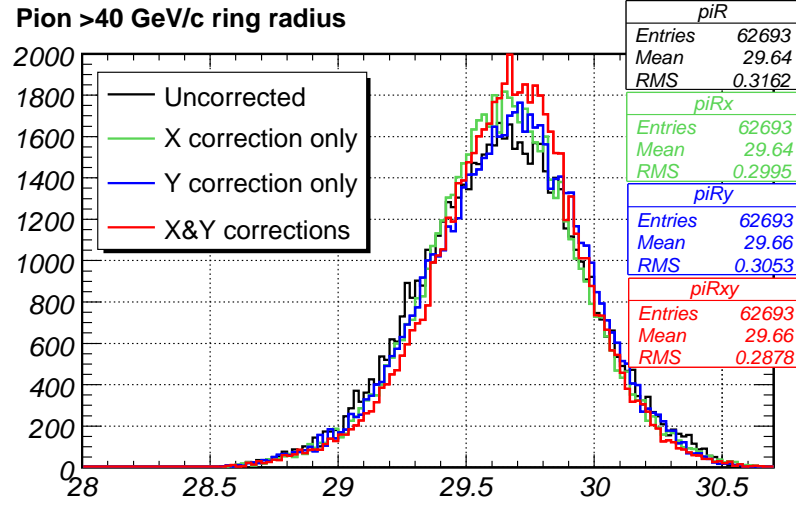


Figure 6.16: A 10% improvement in radius width of high momentum pions is obtained by removing ripple corrections through parametrized equations.

6.6.6 Particle Identification from Ring Radius

For a Cherenkov photon in a gas with index of refraction n , the angle at which photons are emitted by a particle with speed β is given by

$$\frac{1}{2}\theta^2 = 1 - \frac{1}{n\beta}. \quad (6.24)$$

We can define θ_0 as the maximum opening angle, when $\beta = 1$. Then

$$\frac{1}{2}\theta_0^2 = 1 - \frac{1}{n}.$$

From equation of relativistic momentum $p = m\gamma\beta$, we get

$$m^2 = p^2 \left[\frac{1}{\beta^2} - 1 \right] = p^2 \left[\left(\frac{1 - \frac{1}{2}\theta^2}{1 - \frac{1}{2}\theta_0^2} \right)^2 - 1 \right] = p^2 \left[\left(\frac{F^2 - \frac{1}{2}R^2}{F^2 - \frac{1}{2}R_0^2} \right)^2 - 1 \right], \quad (6.25)$$

where $F = 990$ cm is the focal length of the RICH mirrors, and R_0 is the ring radius of a $\beta = 1$ particle. Given the fact that $n \approx 1 + 4.5 \cdot 10^{-4}$ in CO_2 at STP, $\theta_0^2 \approx 9 \cdot 10^{-4}$. Equation 6.25 can then be approximated to better than one part in a thousand by

$$m^2 = p^2 \frac{R_0^2 - R^2}{F^2}, \quad (6.26)$$

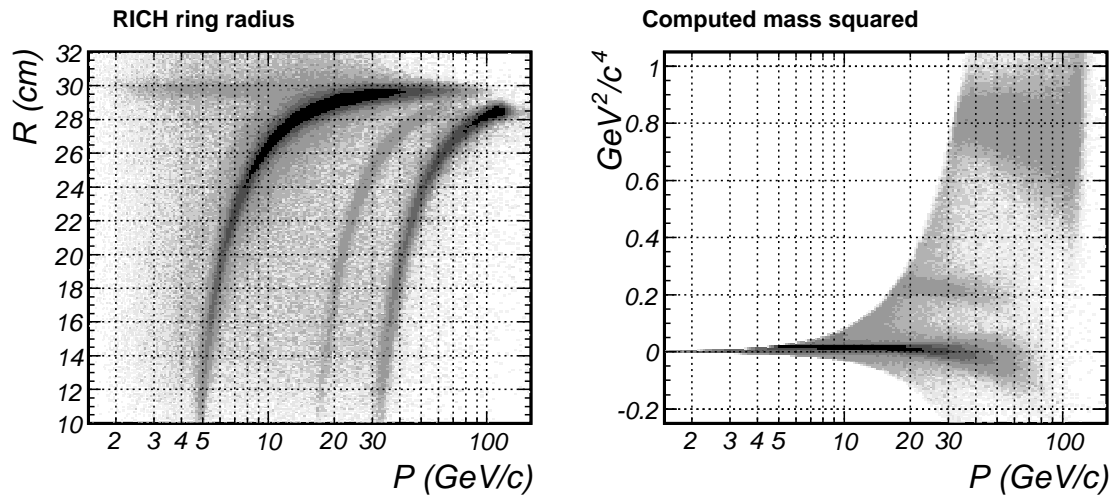


Figure 6.17: The distribution of the RICH ring radii in 120 GeV/c interactions (left) and the same plot where mass squared is computed using Equation 6.26.

which is handy to get a feel for the behavior of the ring radius on momentum. Using Equation 6.25 we can then transform the R vs p plot into a more useful m^2 vs p plot, which can be used for an analysis (see Figure 6.17).

Chapter 7

Detector Calibration and Alignment

Good detector calibration is essential for the reconstruction algorithms to work well. We calibrate different parts of the spectrometer in multiple passes, each subsequent pass depends on the constants generated in the previous passes.

In the first pass, we perform the calibration of systems that do not require tracking: the ADC pedestals, the event trigger time, the time offsets of drift chamber wires, hot channels in the RICH and in the wire chambers. With calibrated drift chamber time offsets, the chamber track finding algorithm is able to improve signal-to-noise ratio. Reliable chamber tracks allow us to align wire chambers and later align other subsystems (TPC, RICH, calorimeters) to the chambers. Finally, when global tracks exist, the calibration of detectors providing particle identification can be done.

7.1 Event Time

Good event time is critical to performance of the TOF wall and K/p separation in a 5 GeV/ c beam. In order to have 3-sigma K/p separation in the TOF wall at 3 GeV/ c , one needs a 200 ps resolution on the time difference measurement (see Figure 7.1).

One of the complications in the calibration of the T0 counters is the temperature dependence of the time offset. This dependence requires an offset for each channel which depends on the time of day. Figure 7.2 shows an example of an overnight run where the delay cables drifted by about 1 ns with respect to the event trigger. It is clear that just

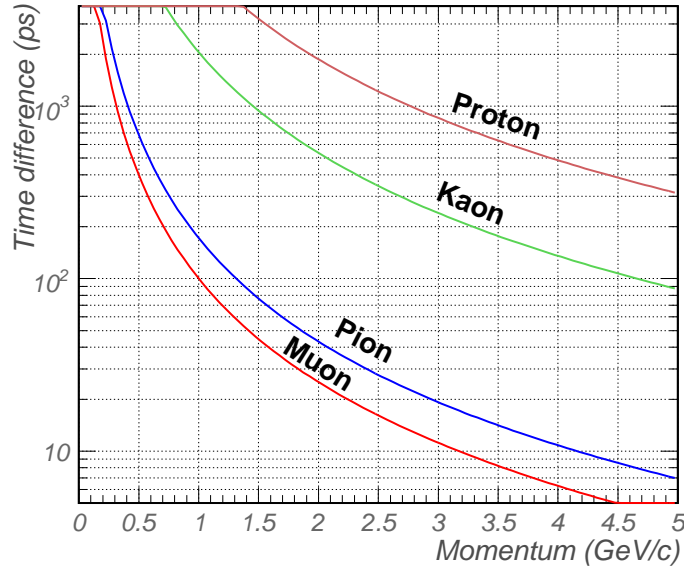


Figure 7.1: The time of flight difference from a $\beta = 1$ particle for a straight line particle from the target to the TOF wall.

one offset per channel per run (or subrun) is insufficient to obtain the desired resolution of 200 ps.

We represent the offset of each channel as a third degree polynomial for each subrun (typically about 5000 events). The coefficients of polynomials are calculated using the following algorithm.

1. Calculate the ADC pedestals.
2. Determine the TDC offset for every PMT and trigger bit. Different trigger bits were timed in to a nanosecond or so, which is good for a trigger system, but these offsets are comparable to the effect we want to correct.
3. Choose the TDC offset of the trigger bit with the largest number of entries as the reference and compute the relative time of the other trigger bits for each counter (a group of 4 PMTs).
4. Partition the data into bursts. Each burst contains at least 80 triggers (if possible) and lasts no more than 10 minutes. Data is first split into accelerator spills, and then

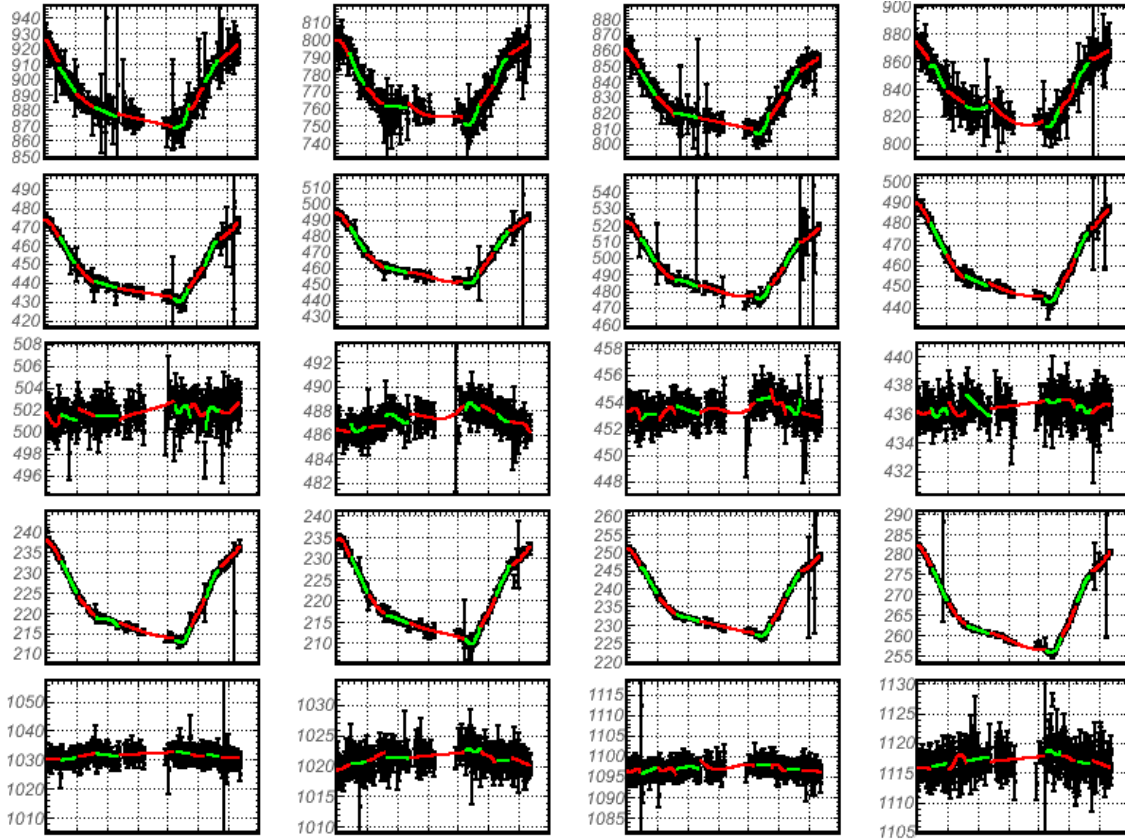


Figure 7.2: Variations in the T0 counters timing offset for an overnight run and superimposed correction curves for every subrun. Each of the five rows shows the distribution for the four PMTs that belong to that counter and the set of cables. From top to bottom, the rows correspond to T00-ribbon, T01-ribbon, T01-RG8, TBD-ribbon, T00-RG8. TDC counts are plotted on the vertical axis, with 60 ns per bin for the TBD-ribbon, and 30 ns per bin for all the other counters.

spills with less than 80 events are merged with adjacent spills unless the burst would become too long. The average time (seconds since Jan 1, 1970) is computed for each burst.

5. Fit the TDC distribution of every channel in every burst to a Gaussian, and save the mean and the error on the mean.
6. Fit the distribution of the TDC versus time to a third degree polynomial for every PMT.
7. Redo steps 2 and 3 using the fits from step 6.
8. Repeat steps 5 and 6 to obtain the final results which get stored into the database.

The second correction applied to the TDC signals is due to the time slewing from the amount of charge that created the signal. Figure 7.3 shows that there is a systematic dependence of the PMT hit time on the amount of charge that the PMT collected. The time slewing correction is computed with the following algorithm:

1. The pedestal-subtracted ADC spectrum is fitted to a Landau function for each channel.
2. Entries between 0.5 and 2.5 of Landau most probable value are used to make a graph for every channel. Entries get sorted by $1/\sqrt{ADC}$, and the TDC distribution of at least 40 entries is fitted to a Gaussian, and is saved along with the average $1/\sqrt{ADC}$.
 - The reason for limiting the range of ADC signals is to avoid over-correcting very small signals and limit the impact of pileup on high-ADC events.
3. The distribution of time versus $1/\sqrt{ADC}$ for each channel is fitted to a parabola.
4. To ensure that the TDC distribution is centered at 0 once all corrections are applied, an overall offset for each channel is calculated with the temperature and the ADC correction taken into account before the results are saved into the database.

Results of these corrections give 120 ps resolution for the T01-TBD time difference (see Figure 7.4, which is sufficiently good for both the TOF wall and the beam time of flight at low momenta).

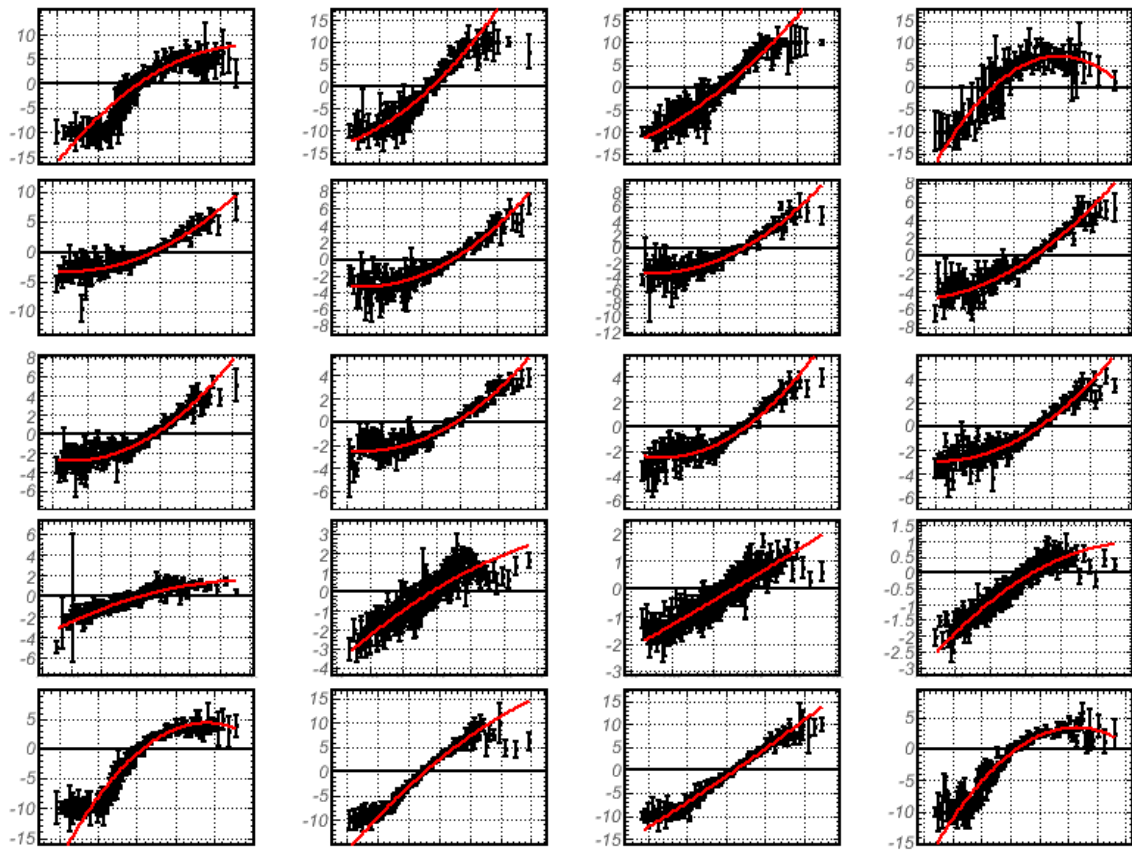


Figure 7.3: The T0 counters' TDC values after temperature correction versus $1/\sqrt{ADC}$ and superimposed quadratic fits. The five rows are identical to those in Figure 7.2.

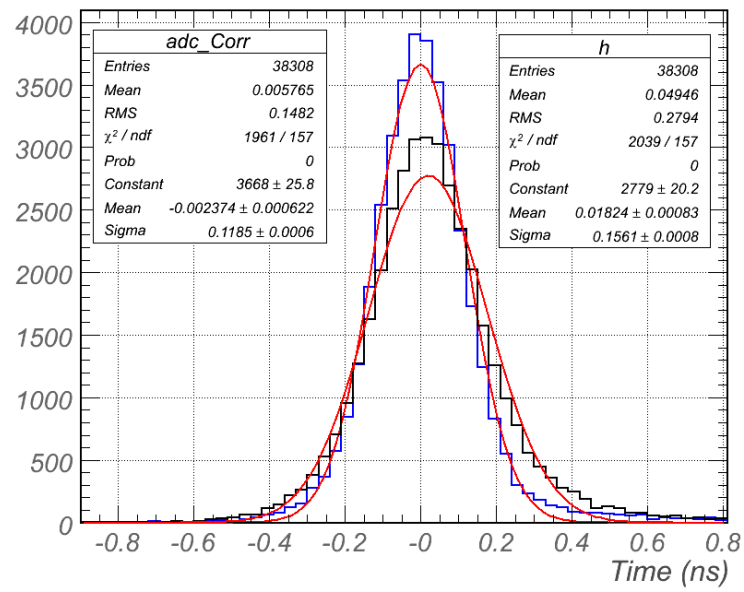
T01 RG8 - TBD Time Difference

Figure 7.4: The reconstructed time difference between the T01 and TBD counters with (blue curve) and without (black curve) ADC correction. The time slewing correction improves the resolution by more than 25%.

7.2 Drift Chamber Time Offsets

Between the drift chamber electronics and the difference in cable length, the time offset has to be calculated for each wire. In addition, since there are systematic shifts from run to run we need a constant for each wire and run. No single run has enough statistics to determine the offset for each wire, so we use the following approach to compute the time offsets (t_0 's).

1. In each run we determine t_0 for the wires which have enough statistics;
2. For each run where at least 3 wires are fit, we compute the average $t_{0,run}$ for the run;
3. For every wire in the runs that have the run offset computed, we compute the overall offset for the wire ($t_{0,wire}$) by shifting entries from different runs by $t_{0,run}$.
4. For every run, we use wires with a valid $t_{0,wire}$ to recalculate $t_{0,run}$;
5. As steps 3 and 4 are repeated three times, each subsequent iteration picks up more runs and wires;
6. For every wire in every run, the time offset is set to t_0 if it was computed in step 1, otherwise it is set to $t_{0,run} + t_{0,wire}$, thus taking into account the differences from run to run and from wire to wire.

7.2.1 Event Selection

Event selection is quite important in order to determine t_0 's well. We attempt to limit pileup by imposing the following requirements:

- No more than two T0_{13/4} or TBD_{3/4} are allowed in the event;
- If there are two 3/4 signals in either counter, the time separation between the two has to be at least 100 ns;
- If a beam chamber has more than 24 wires hit, it is ignored;
- If a drift chamber has more than 150 wire hit, it is ignored.

Although a significant fraction of the data is thus ignored, the signal to noise ratio is much higher than if all the available data are used. Given the fact that wires on the edge of the chamber have little signal, it is extremely important to reject noise.

7.2.2 Fitting

Wire time distributions can be modeled quite well by a Gaussian with an exponential tail, i.e.

$$f(t) = \begin{cases} A \exp\left(-\frac{1}{2}\left(\frac{t-t_{peak}}{\sigma_t}\right)^2\right), & t < t_{peak} + \sigma_{cut}\sigma_t \\ A \exp\left(\frac{1}{2}\sigma_{cut}^2 - \frac{t-t_{peak}}{\sigma_t}\sigma_{cut}\right), & t \geq t_{peak} + \sigma_{cut}\sigma_t \end{cases} \quad (7.1)$$

Here t_{peak} is the center of the Gaussian peak, and σ_{cut} is a unitless parameter that determines how many sigma to the right of the peak the function becomes exponential. In this representation, the function and its derivative are continuous. After making a guess at parameters for a histogram, the fitting is done using the TMinuit minimizer package from ROOT. The time at half-maximum was taken as t_0 .

7.3 Chamber Alignment

7.3.1 Aligning Chamber Planes

Initial chamber plane positions from the survey of the experimental hall agreed with data to a few millimeters. Misalignment of chamber planes was sufficiently small, so that the track finding efficiency was not much affected, but as Figure 7.5 shows, an improvement to the alignment was necessary. To put matters in perspective, a 120 GeV/ c particle is deflected from a straight line by only 1.8 cm through the length of the experiment, so a half wire spacing (1.5 mm) misalignment can create a 10% systematic effect on the momentum measurement of a 120 GeV/ c particle.

The chamber alignment is split into two parts:

- Align the beam chambers,
- Align chambers 1-6 to the beam chambers.

Doing alignment for beam chambers separately boosts statistics for the 3 chambers, since a good beam track is available in more than 90% of events. Chamber 1-6 alignment is done with 6-chamber tracks and 9-chamber beam tracks. The first set of tracks makes it possible to determine the chamber rotations relative to one another (BCs do not have a long enough lever arm), and the second set makes sure that the alignment of all 9 chambers is consistent.

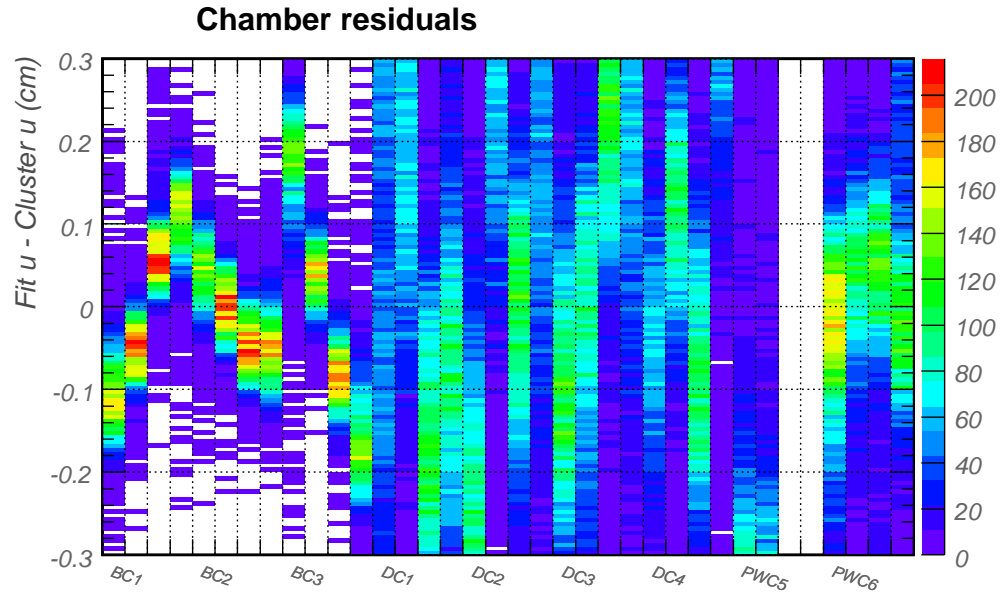


Figure 7.5: Chamber residuals before the chamber alignment was done. On the horizontal axis are chamber planes, on the vertical, residuals from 9-chamber track fits.

Track selection is crucial to a successful alignment calculation. For the final pass, we select only those tracks that pass through all the 6 chambers and where at most two chamber planes are missing. Requiring almost all planes to be present provides immunity to incorrectly reconstructed tracks and reduces the bias due to an insufficient amount of data. Unfortunately, the chamber efficiency is not high enough to allow us to use only those tracks where all the chamber planes are present (see Figure 6.3). If a wire plane contains two hit wires, it is excluded from the fit so as to limit the impact of noise and pileup. Lastly, tracks below 4 GeV/c are rejected, because of significant multiple scattering, and the fact that continuous energy loss in the spectrometer is not taken into account in the track fits. This requirement is not a heavy toll on available statistics because of the poor geometric acceptance for low momentum particles in chamber 6.

The alignment algorithm is quite simple. For each wire in the track we calculate the unbiased residual, i.e. the residual when the wire is taken out of the track fit. We compute the mean of residuals for each wire plane using all available tracks, and shift the wire plane by 0.3 of the residual. Next the track list is preened by removing those tracks

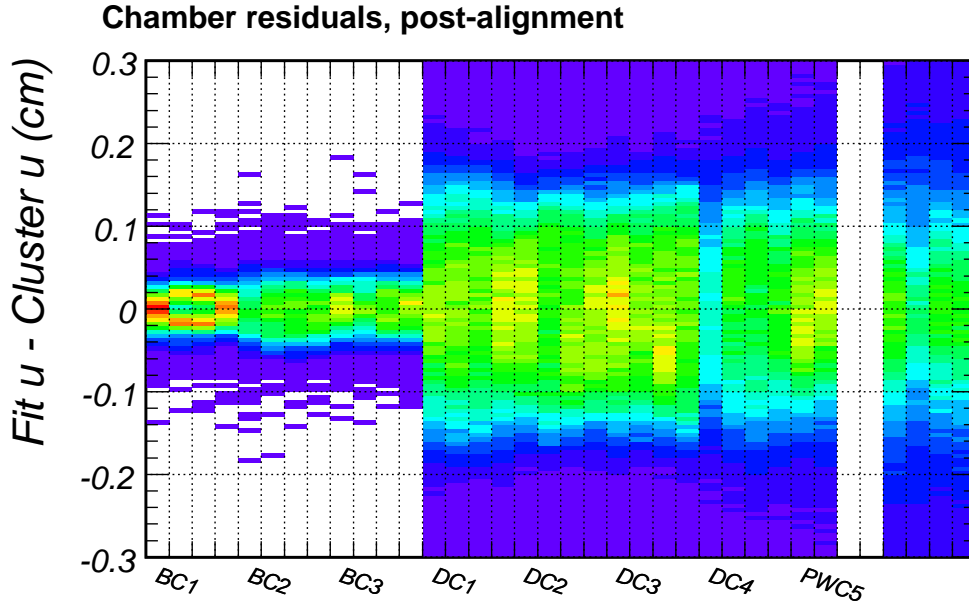


Figure 7.6: Residuals once chamber alignment was completed.

where at least one residual exceeded 1.5 wire spacing plus the absolute value of the computed mean of residuals. The procedure is repeated until the largest mean of residuals is below 1% of wire spacing.

A typical run with at least 5000 tracks provides enough statistics to do reliable alignment and to monitor stability and correlation with beam momentum of alignment constants.

7.3.2 Z-alignment and Rotations

A lot of effort went into verifying that chamber z -positions and rotations about the z -axis are correct in the description of the spectrometer geometry[30]. Since the magnetic field makes track fits more uncertain, we primarily relied upon the data with magnetic field off. Unfortunately, the amount of available field-off data is very small, so the precision of the field-off alignment is limited. Nevertheless, through this work we found significant errors in positioning of the wire chambers in the experiment.

The algorithm for z -alignment of chambers is similar to the wire plane alignment:

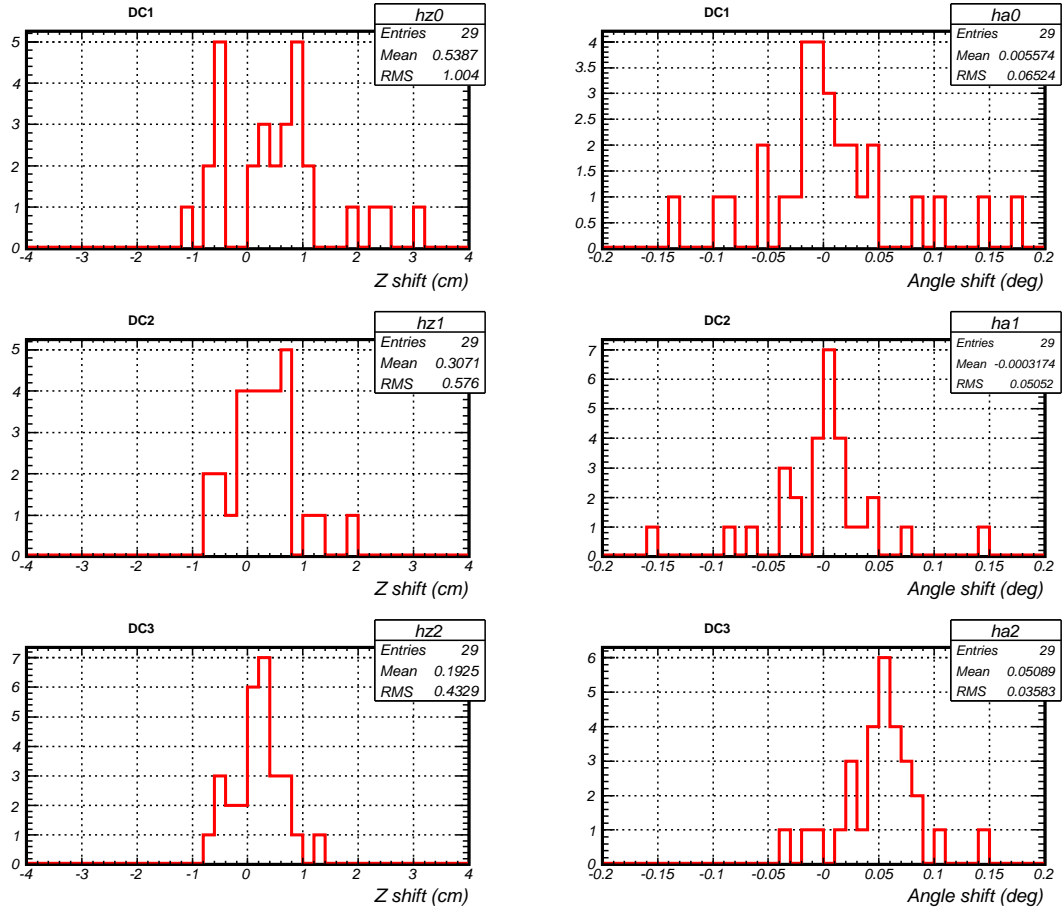


Figure 7.7: DC123 z -alignment with field-off runs with no known geometry errors. Still, DC3 is being systematically rotated by 0.055° by z -alignment algorithm in 29 different runs from 5 different time periods.

tracks are stored in memory for the entire run, and at the end minimization of the sum of χ^2 is done using TMinuit by shifting the z of the chambers and rotating them about the z -axis.

Figure 7.7 shows that even when all known errors were solved in the geometry description, DC3 appeared to have a rotation about the z -axis of $0.055^\circ \approx 1$ mrad. The effect of this rotation on the edge of the chamber is about $\frac{1}{4}$ of wire spacing, and therefore was corrected based on the results of alignment.

Figure 7.8 shows results of the z -alignment algorithm re-run with DC3 rotated. Here we see that the alignment algorithm wants to move DC123 in z by 5 mm, 3 mm, and

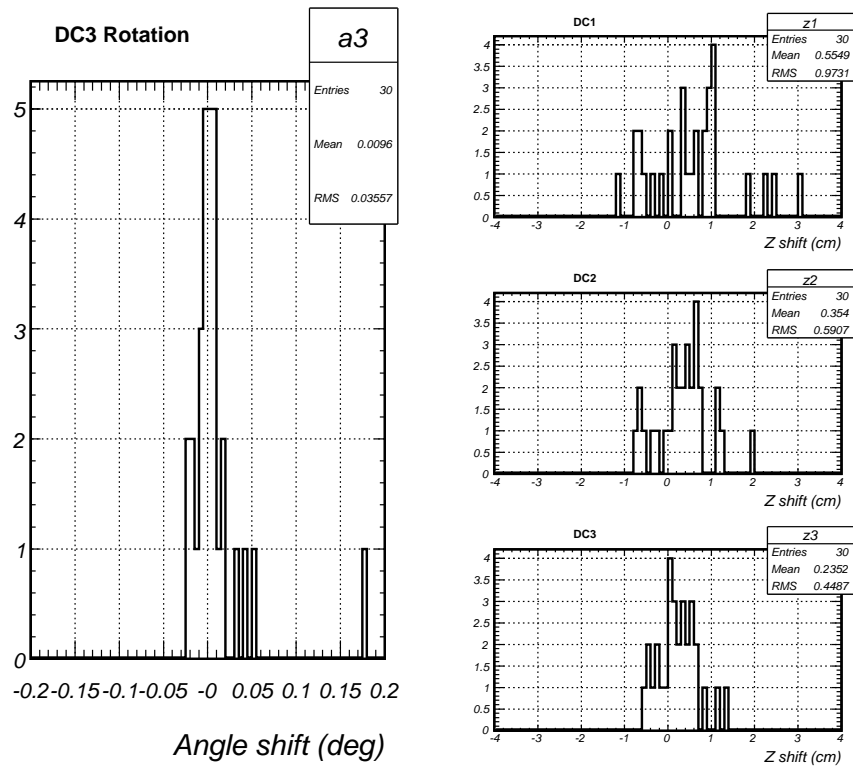


Figure 7.8: DC123 z-alignment after the rotation in DC3 was removed.

2 mm respectively. These corrections were not applied for the following reasons:

- We do not take into account the Earth’s magnetic field and the residual field in the magnets;
- Rotation of chambers about the x - and y -axes, which can shift the z -position of the hit, is not taken into account by the reconstruction;
- The systematic error on position measurement due to these misalignments is less than 0.1 wire spacing.

7.4 Tuning the Magnetic Field

Measurement of the magnetic fields with Ziptrack had very small uncertainties in the positions of the Hall probe jig, but due to the size of the holder, the precise rotation of the probe could not be set or measured. This leaves room for the dominant component to bleed into a smaller component and thus can be observed with data as well as magnetic field measurements.

7.4.1 B_x/B_y Rotation

The wire plane alignment of runs with different momenta showed very strong correlation of the alignment constants for vertical-measuring planes of the PWCs (see Figures 7.9 and 7.10). Multiple studies concluded that the large B_x component of the field in magnet field map was the most likely source of this problem

To determine whether the dominant B_y is bleeding into B_x we ran another track χ^2 minimization algorithm, where only 9-chamber beam tracks were used, and the algorithm was free to rotate B_x and B_y components of the two magnets through

$$\begin{aligned} B'_x &= B_x \cos \theta + B_y \sin \theta, \\ B'_y &= -B_x \sin \theta + B_y \cos \theta. \end{aligned}$$

The results, shown in Figure 7.11 demonstrate that $\theta_{JGG} = \theta_{Rosie} = 0$ is not consistent with data. The large spread of the two rotation angles comes from the fact that a minor misalignment of the chamber planes has an enormous effect on the large-momentum runs, and the minimizer will compensate for the misalignment by inflating B_x .

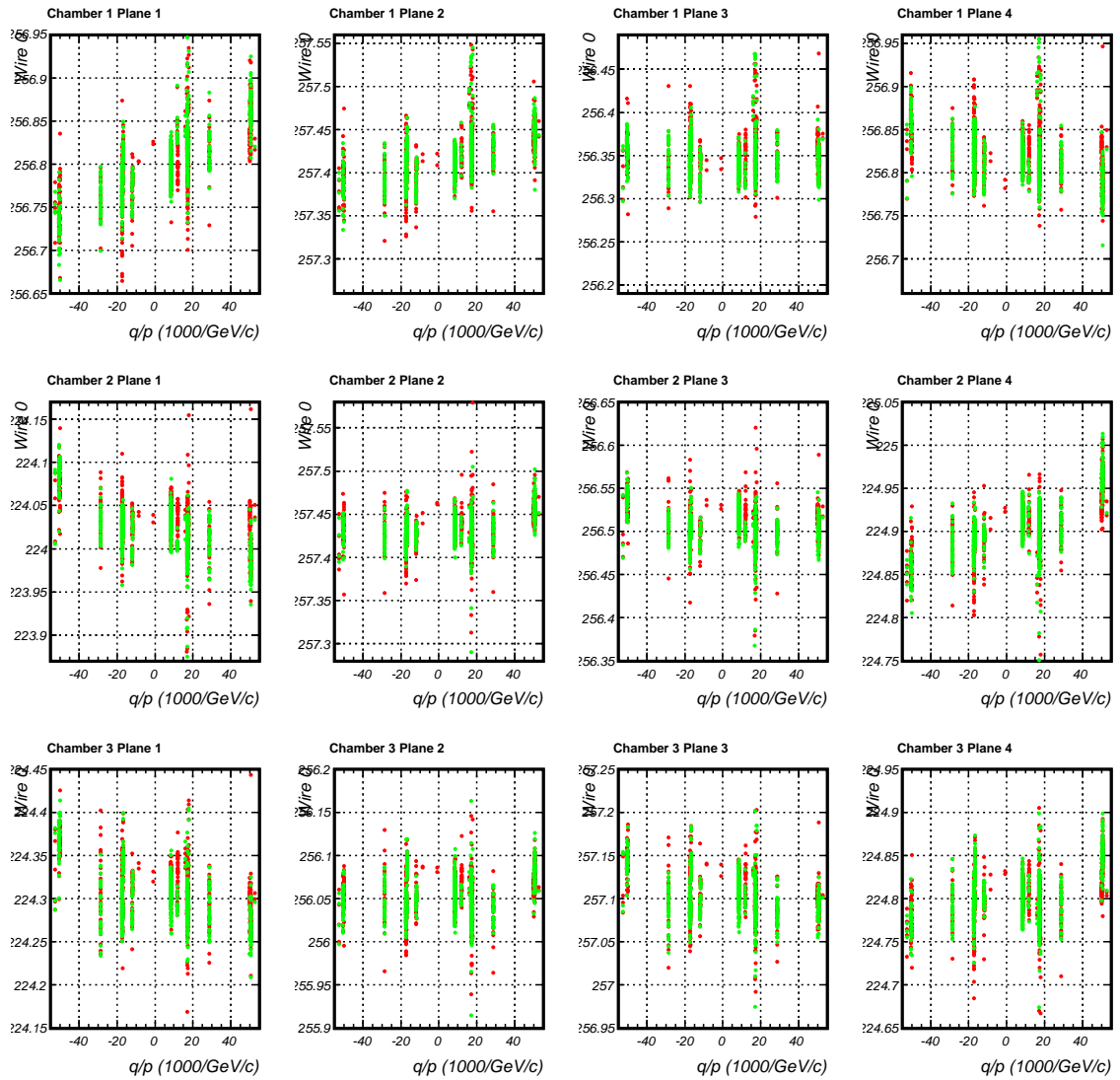


Figure 7.9: The DC123 alignment results for runs with different beam momenta. Red dots come from the alignment with the BCs fixed, and green diamonds from the alignment when the BCs are allowed to vary.

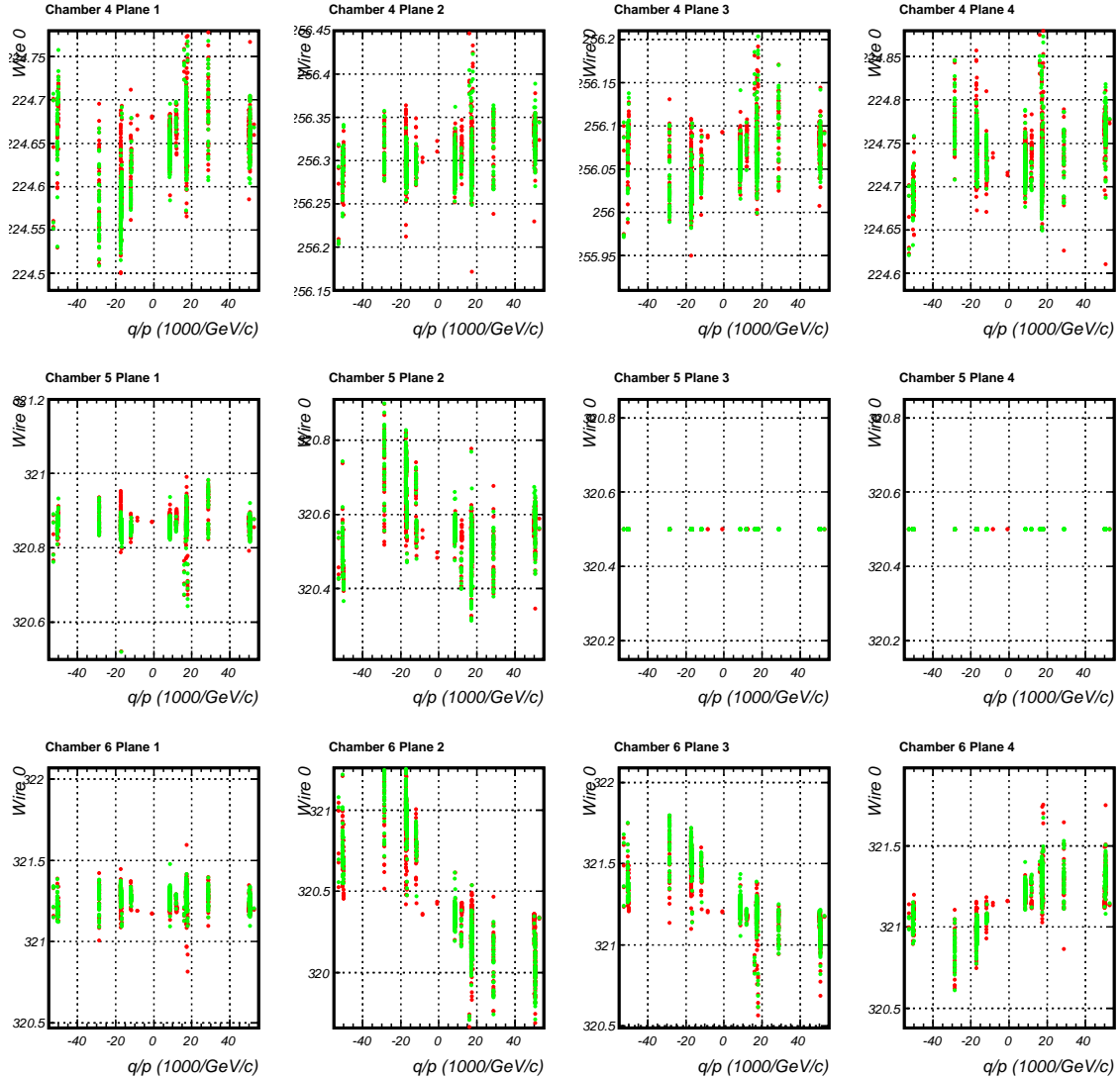


Figure 7.10: The DC4 and PWC56 alignment results for runs with different beam momenta. Red dots come from the alignment with the BCs fixed, and green diamonds from the alignment when the BCs are allowed to vary. Notice the large correlations of alignment offset in the second (vertical-measuring) plane of PWC5 and PWC6.

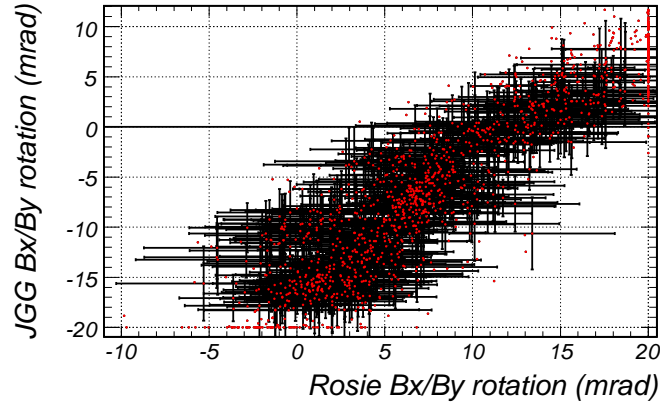


Figure 7.11: Results of optimizing the B_x/B_y rotation. While the different runs are clustered in a line rather than a single point, all runs exclude rotation $(0, 0)$ for the two magnets' field components.

The two magnets' fields were measured with the same apparatus rotated by 180° about y -axis. Therefore, if the misalignment truly comes from rotation of the Ziptrack Hall probe holder, the B_x/B_y ratio in the center of the magnet (where B_x has to be vanishingly small), must be equal and opposite. Figure 7.12 clearly shows that this is the case in the magnetic field measurements, and the B_x/B_y ratio is about 0.7%. The point $(7, -7)$ mrad is supported by the data, as it falls in the middle of the band in Figure 7.11, so B_x/B_y components in the two magnet field maps were rotated by 7 mrad in opposite directions.

7.4.2 B_y/B_z Rotation

While the experiment is not very sensitive to B_z since most track angles are small with respect to the z -axis, the Hall probe measurements do suggest a 3 mrad rotation of the B_z/B_y components, which was done in the same way as the B_x/B_y rotation. The summary of the chamber wire plane alignment constants with the xy and yz rotations of the Hall probes taken into account is shown in Figures 7.13 and 7.14.

7.4.3 B_x/B_z Rotation

The most difficult rotation of the magnetic field components to correct is that about the y -axis. B_x and B_z are comparable in most regions of the magnet, so B_x/B_z or B_z/B_x ratios of magnetic field measurements are not as easy to interpret as the B_x/B_y or

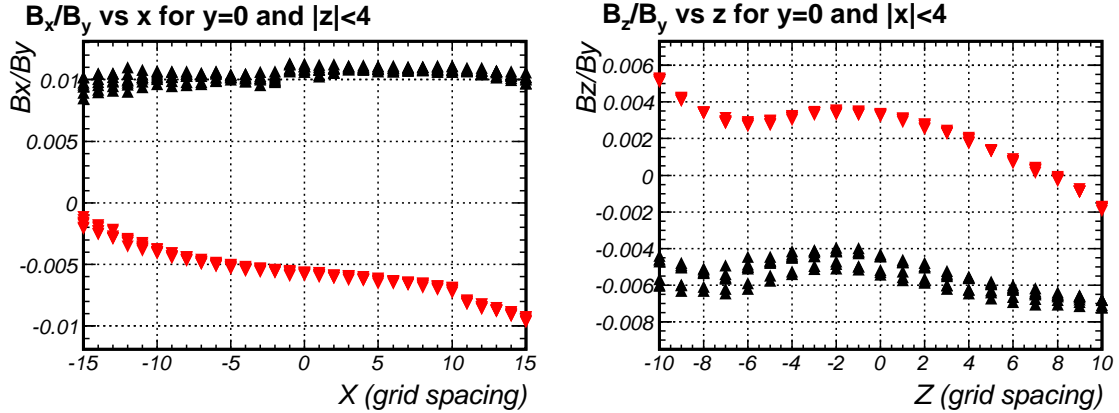


Figure 7.12: The ratios of field components in the center of the magnet. JGG is shown in up-pointing black triangles and Rosie in downward-pointing red triangles.

B_z/B_y ratios. While tracking is not very sensitive to this rotation, the TPC drift correction is. To determine the optimal rotation, the slope of the TPC x -residual vs z was measured for different values of the component rotation. Results shown in Figure 7.15 suggest that the data wants to have the components rotated by 9.6 mrad.

The ratio of the magnetic field components favors rotation of the same magnitude (see Figure 7.16) to achieve better symmetry of the B_x/B_z ratio. Given that the rotation is of the same order of magnitude as the other two rotations, and the TPC is more sensitive to it than the magnetic measurements are, a rotation of 9.6 mrad was applied to both JGG and Rosie.

7.5 TPC Electron Drift

Understanding of electron drift in the the TPC consists of two more or less independent problems. The first is measuring the drift velocity in the absence of a magnetic field, which is equal to the drift velocity when the magnetic and electric fields are collinear. We call this velocity v_0 . The second problem is the drift velocity components given the magnetic field strength and the angle between the magnetic and electric fields (electric field is assumed to be a constant 122 V/m). This 3-dimensional effect distorts the tracks from a straight-line projection in a complicated fashion by as much as 8 cm in x and 10 cm in z . Good understanding of this effect is crucial if the TPC measurements are to be trusted.

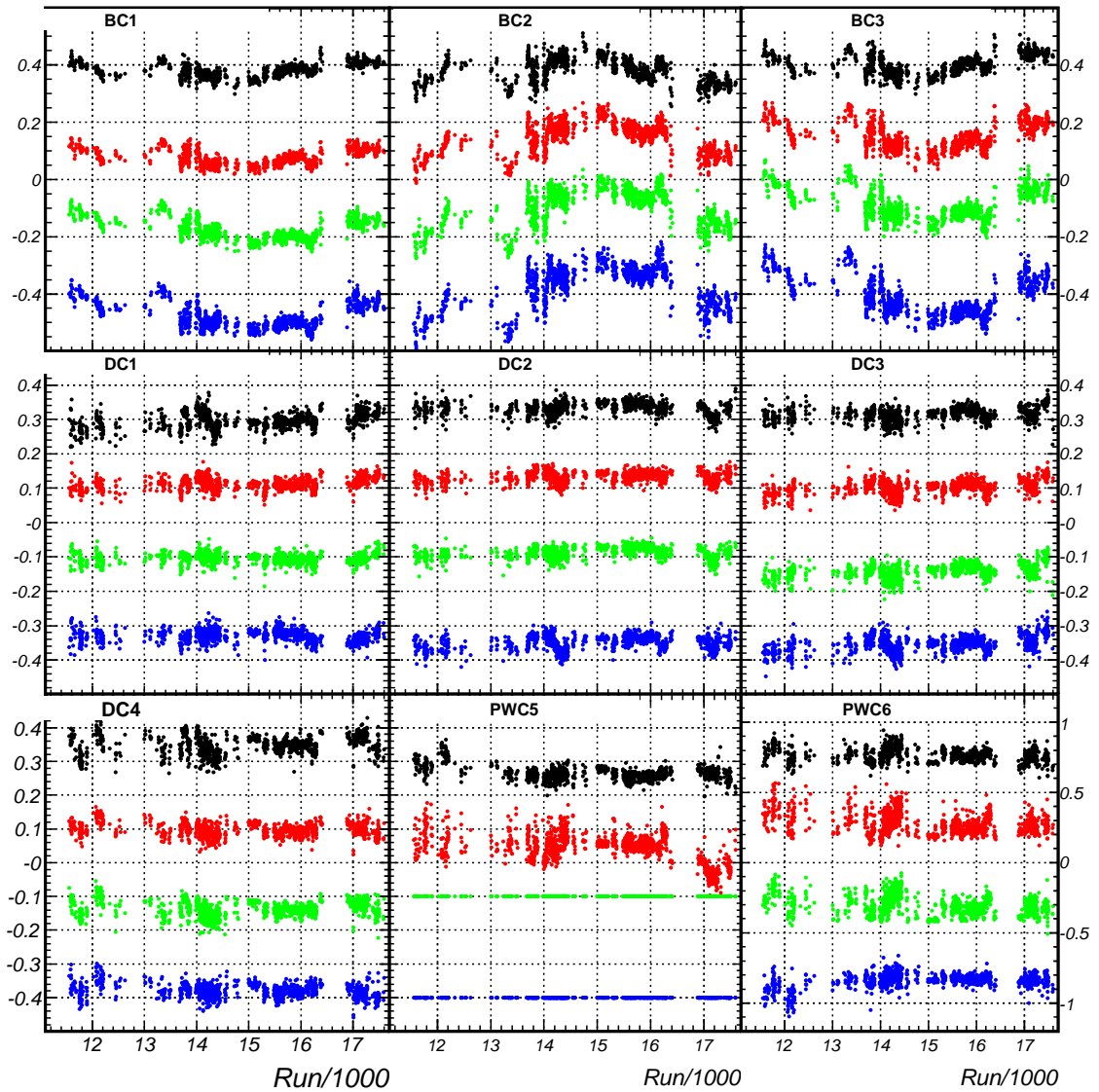


Figure 7.13: Alignment summary with geometry and magnetic field corrections. Plane 1 is at the top of every set of graphs for each chamber. Note: the y -scale of PWC6 plots is different from all the other chambers.

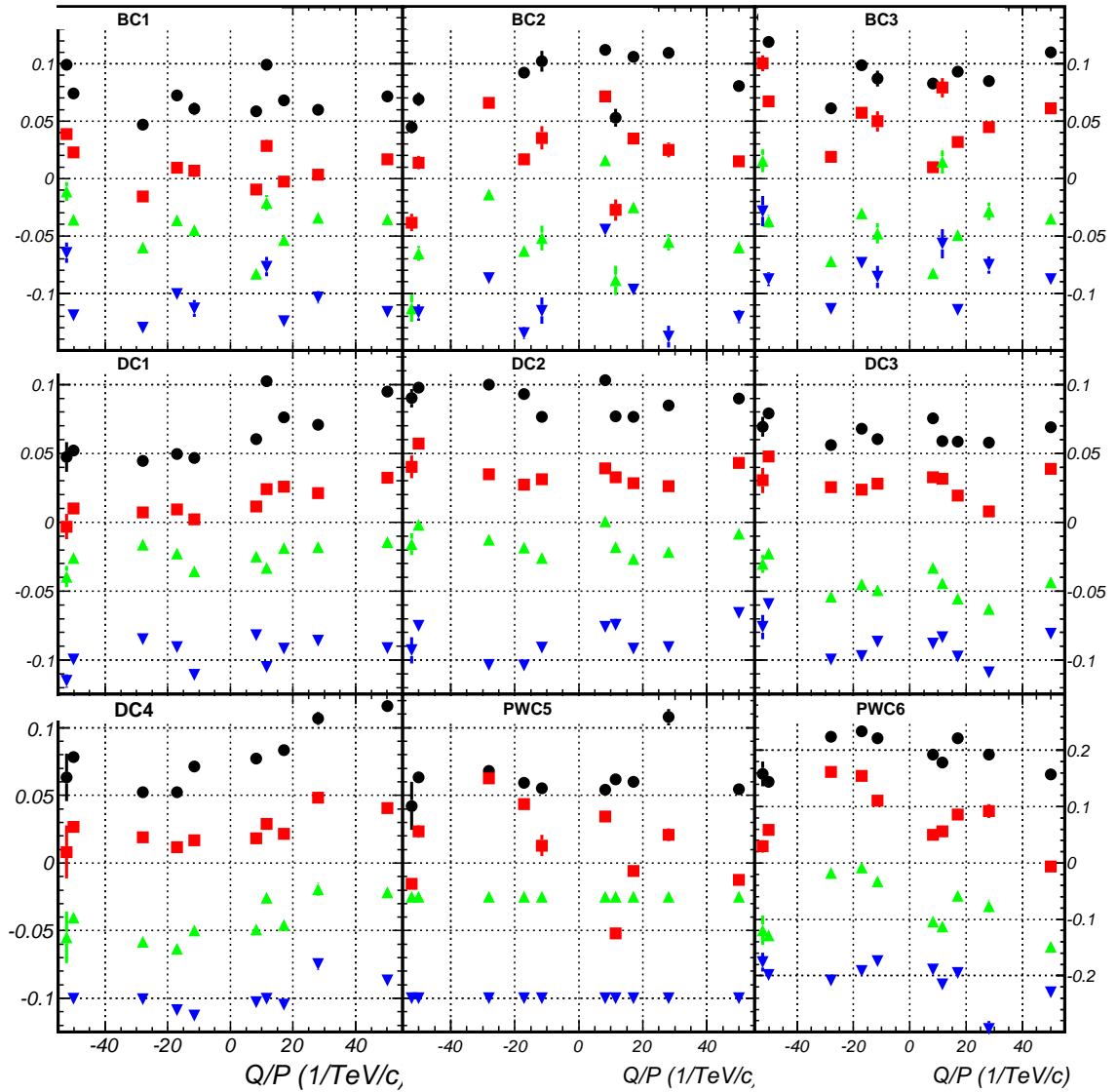


Figure 7.14: The alignment summary with the geometry and magnetic field corrections. Plane 1 is at the top of every set of graphs for each chamber. While correlations with momentum still exist, they are small, and their effect on tracking can be measured. Note: the scale of the PWC6 plots is different from all other chambers.

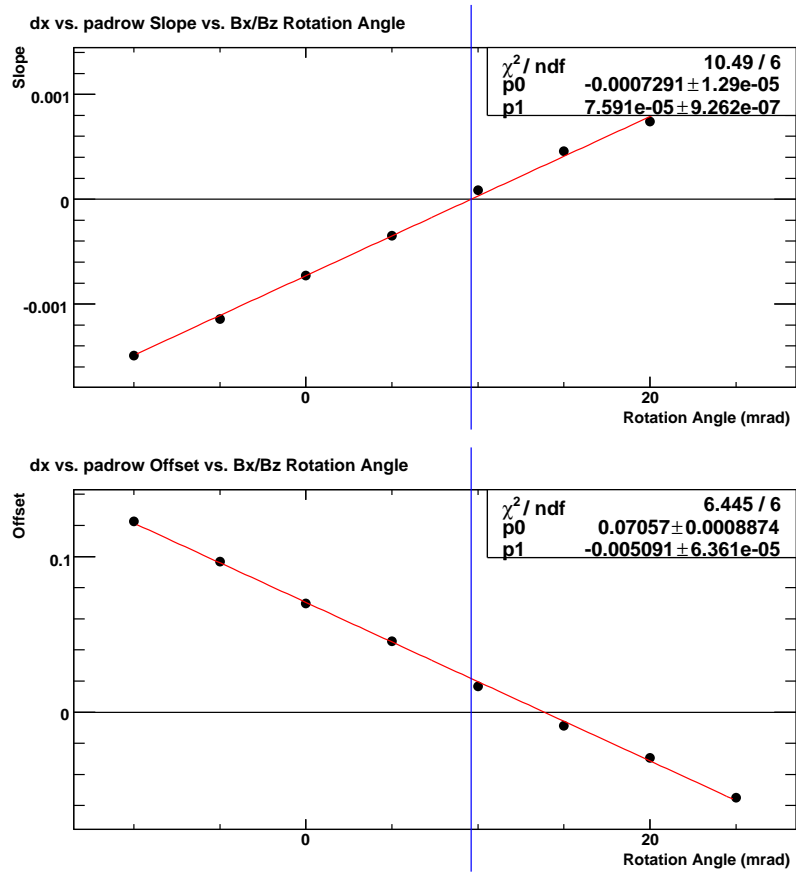


Figure 7.15: The dependence of the slope of the x -residual on z for different rotations of B_x/B_z components.

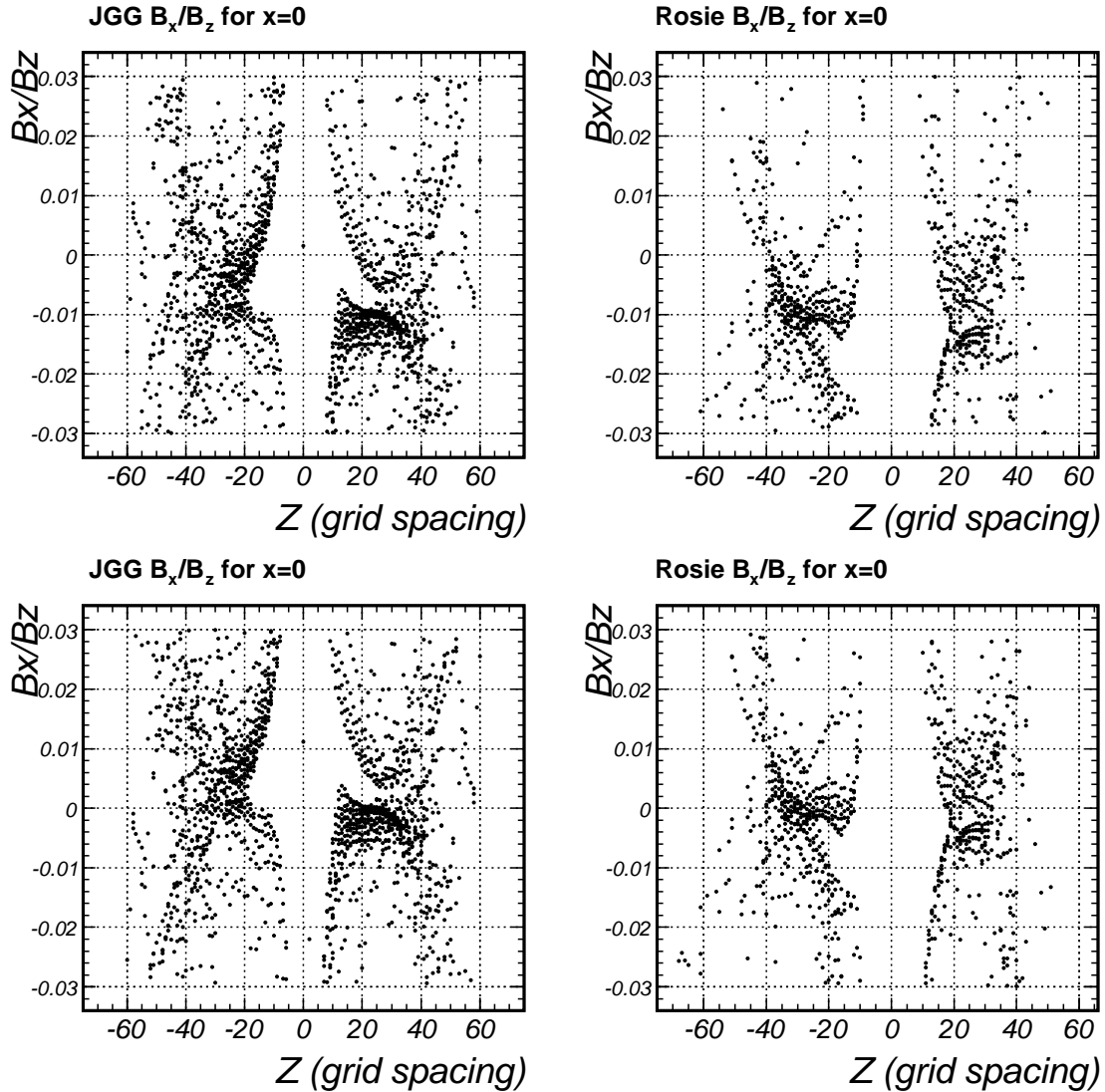


Figure 7.16: The top pair of plots shows the ratio of B_x/B_z of the two magnets for $x = 0$ in the field map. The bottom pair shows the same ratio when the field components are rotated by 9.6 mrad . Note that unlike B_x/B_y and B_z/B_y , the sign of this ratio is expected to be the same for both magnets, since the Hall probes were rotated about the y -axis.

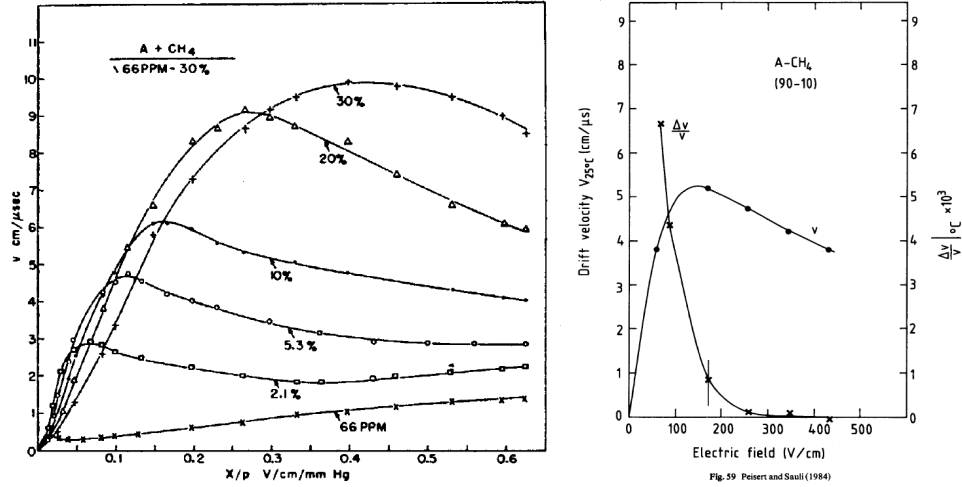


Figure 7.17: Two sets of measurements of the drift velocity in P10 mixture[15, 38].

7.5.1 Measuring v_0

Electron drift velocity in argon-methane mixtures is a function that depends on a number of variables: the fraction of methane, the ratio of electric field to the gas pressure, oxygen and water vapor contamination, and the gas temperature. Measurements for a clean P10 (90% Ar 10% CH₄) are shown in Figure 7.17. The choice of P10 at atmospheric pressure makes the dependence of the drift velocity on pressure very weak when electric field is about 120-150 V/cm.

Distortions of the drift velocity in the center of the TPC are small as the field is quite uniform. This makes it possible to measure the drift velocity even when the magnetic field is on using the reconstructed hits in the center of the TPC drift volume.

In order to remove any sort of bias from the measurement of the drift velocity, we did the full event reconstruction and then refitted the vertex using only the information from the wire chambers. In order to achieve this using one value of the drift velocity for all runs, the cut windows to match the TPC track to chambers were quite loose. Once the vertex-constrained fit was done, we selected the vertices with three or more secondary tracks, and saved the position predicted at the z of the hit and its measured time. One can take two distinct approaches to measuring the velocity: bin the data in t or z and do a least squared fit or do a non-linear fit minimizing the sum of the squares of distances from the straight line to the data points. The latter method has the advantage that the outliers have

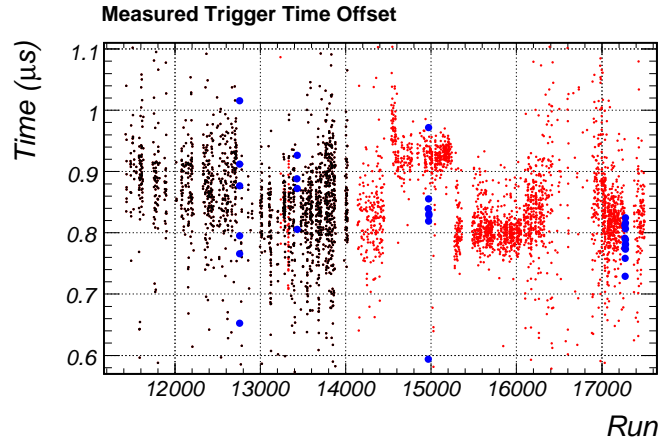


Figure 7.18: The measured TPC trigger delay time as a function of run. Large blue circles come from field off runs. See text for further explanation.

a smaller effect on the fitted slope, and therefore is not as sensitive to the event selection as the former method.

One of the unknowns in the system is the trigger delay time, which should be constant from run to run. Figure 7.18 shows the measured trigger offset as a function of run. There are some notable features in the plot:

- Runs before 12700 have a systematically different trigger delay. Between runs 12700 and 13000, a lot of work on the trigger was done in the hall, so while we do not know how much the trigger time was changed, the data suggests a 70 ns difference.
- NuMI runs (14500-15250) measure a different trigger delay. This is not very surprising, because NuMI events have much higher multiplicities and therefore wide windows to match TPC tracks to chamber data may have an adverse effect.
- Field-off data gives approximately the same delay as field-on data, which is a confirmation that the effect of the magnetic field on the drift velocity in the center of the TPC is negligible.
- Runs before 14100 were taken with a larger gating grid delay, which limited the active volume of the TPC. As expected, the reduction of the gating grid delay did not affect the trigger delay.

With these results, we fix the delay to 875 ns for runs before 12700 and to 800 ns

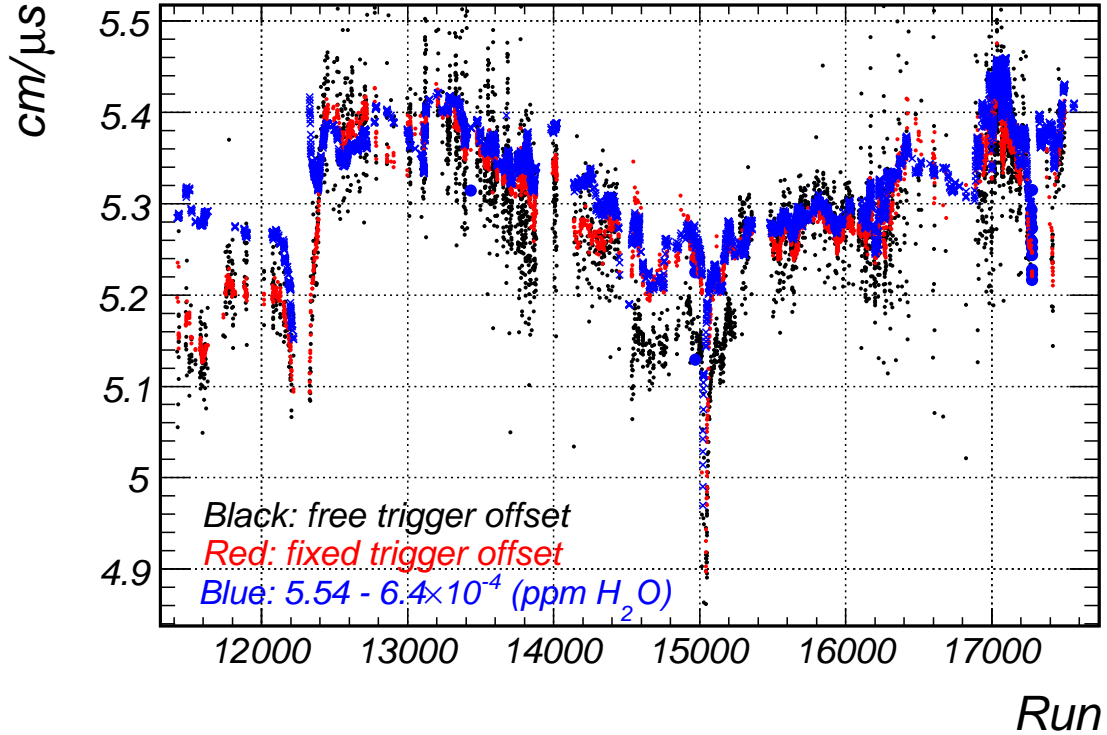


Figure 7.19: The measured TPC drift velocity as a function of run. The benefit of fixing the trigger time is clear: the precision of velocity measurement is much higher, and the correlation with water content in the TPC gas becomes much stronger.

for runs above 12700. Then we go back to the data to measure the drift velocity with a constant trigger delay. Figure 7.19 shows the measured drift velocity when the trigger offset is free, and when it is fixed.

The computed drift velocity varies smoothly with the run number, and strongly correlates with the water content measured in the TPC exhaust gas. Therefore, we feel that v_0 is measured to 0.01 cm/μs, or 0.2%. The 10 ns uncertainty on the trigger delay time adds a 0.2% systematic error on the hit position. At the top of the 80 cm drift volume, this translates into a better than 2.4 mm precision of the y -measurement.

7.5.2 Distortion Corrections

Electron drift in a non-uniform magnetic field is a complicated problem. Conceptually, it is clear that if the electric and magnetic fields are not collinear, the force due to the magnetic field on electron creates a force proportional to $\vec{E} \times \vec{B}$, but the electron motion

in that direction will cause additional force proportional to $(\vec{E} \times \vec{B}) \times \vec{B}$, hence all three components of the drift velocity are non-zero.

A linear model of drift is motivated by a drag force on the electron, which is proportional to the drift velocity[5]:

$$\frac{d\vec{v}}{dt} = \frac{e}{m}\vec{E} + \frac{e}{m}\vec{v} \times \vec{B} - \frac{\vec{v}}{\tau} = 0, \quad (7.2)$$

where \vec{v} is the drift velocity, e is the electron charge, m is its mass, \vec{E} is the electric field, \vec{B} is the magnetic field and τ can be thought of as the mean time between collisions of the drifting electron and the gas molecules. Equation 7.2 can be solved to obtain

$$\vec{v} = -\frac{|e|\tau E/m}{1+b^2} \begin{pmatrix} (1+b_x^2)e_x + (-b_z + b_x b_y)e_y + (b_y + b_x b_z)e_z \\ (b_z + b_x b_y)e_x + (1+b_y^2)e_y + (-b_x + b_y b_z)e_z \\ (-b_y + b_x b_z)e_x + (b_x + b_y b_z)e_y + (1+b_z^2)e_z \end{pmatrix}, \quad (7.3)$$

where signs take into account the negative charge of electron, $\vec{E} = E(e_x, e_y, e_z)$, $v_0 = |e|\tau E/m$, and $b_i = \frac{|e|\tau}{m} B_i = \frac{v_0}{E} B_i$.

If $\vec{E} = E\hat{y}$, and $\vec{B} = B(\cos\theta, \sin\theta, 0)$, this equation reduces to:

$$\vec{v} = -\frac{v_0}{1+b^2} \begin{pmatrix} b^2 \cos\theta \sin\theta \\ 1 + b^2 \cos^2\theta \\ b \sin\theta \end{pmatrix}, \quad (7.4)$$

where $b = v_0 B/E$.

However, when this equation is used to correct the drift, one quickly sees that there is significant over-correction in both x and y (Figure 7.20). While we do not know the reason why the linear model fails to describe the drift in the TPC, the solution was to use the Magboltz Monte Carlo program[39, 40]. Magboltz takes the gas mixture, constant electric and magnetic fields at an arbitrary angle with respect to each other. Simulated trajectories of 10^6 electrons are used to predict the three drift velocity components. In order to use the results given by Magboltz, we had to create a map of the drift velocity components in (B, θ) space, with θ is defined by Equation 7.4. Figure 7.21 shows that we needed to include angles up to 50° into this map.

We included all the details of the gas mixture that were provided by our monitoring:

- Oxygen concentration, which was relatively stable at 350 ppm.

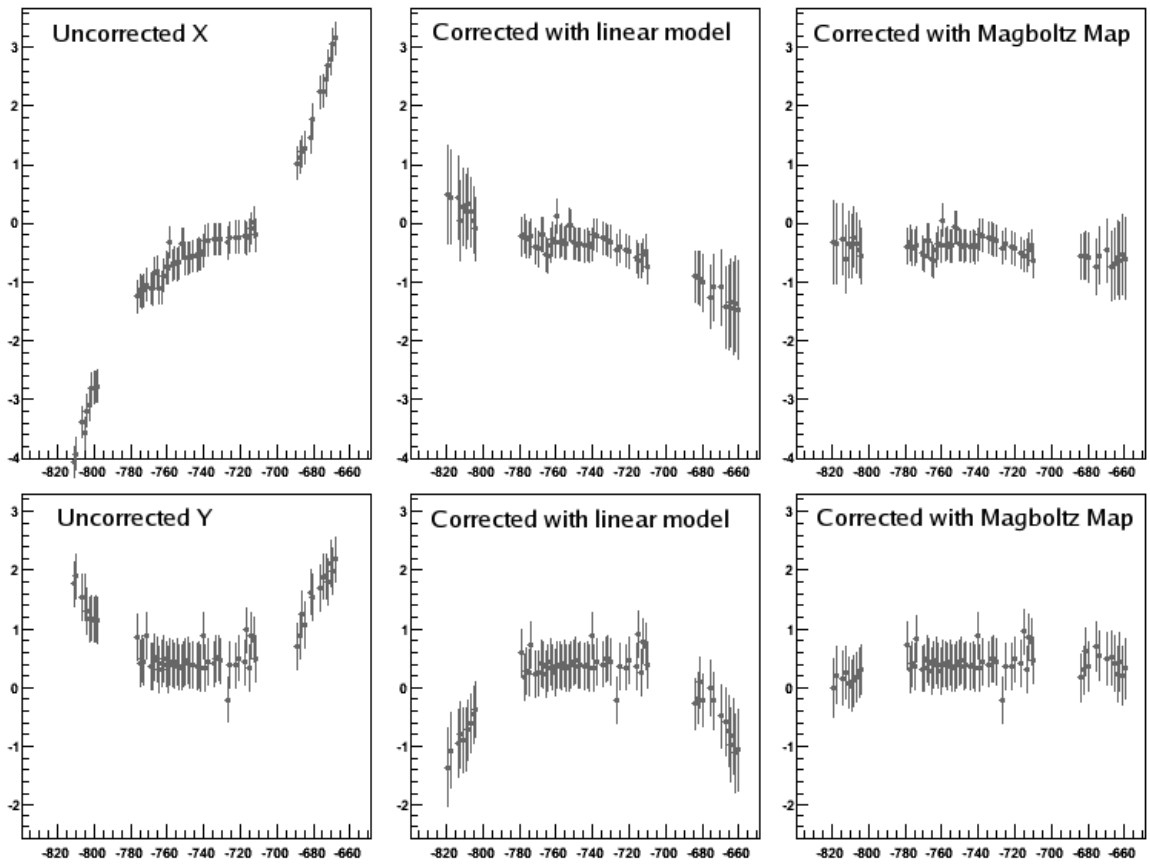


Figure 7.20: xz and yz projections of TPC hits from a 120 GeV/ c track. The units on both axes are cm.

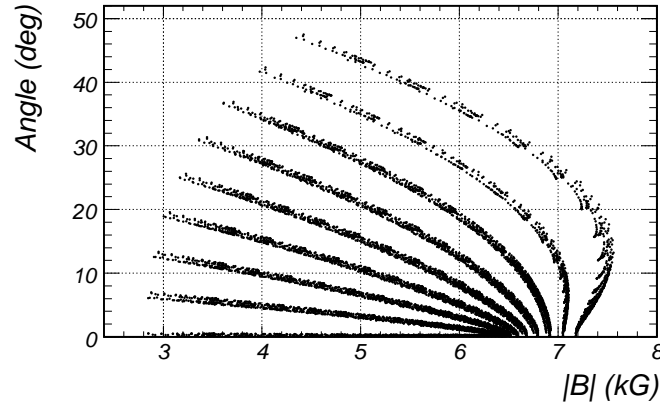


Figure 7.21: The angle between the vertical and horizontal field components in the JGG field map inside the TPC drift volume.

- Nitrogen concentration at 78/21 of oxygen concentration, since oxygen must have come from air together with nitrogen.
- Water concentration. Since drift velocity strongly correlates with water content, gas mixtures with 50, 300, 550, 700, and 950 ppm of water were modeled with v_0 of 5.403, 5.299, 5.179, 5.097, and 4.965 cm/ μ s respectively.

Equipped with 5 Magboltz maps and v_0 for a run, we compute the map for the run using a weighted sum of the 2 maps with the closest v_0 , since $v_i(B, \theta)/v_0$ depends on v_0 . As Figure 7.20 shows this model of electron drift agrees with the data.

7.6 RICH R_0

Over the course of the run, the CO_2 density in the RICH fluctuated by about 1.5%, which translates into a 3 mm difference in R_0 ($\beta = 1$ ring radius). The RMS width of the 120 GeV/ c proton ring distribution is about 1.8 mm, so at high momenta density fluctuations widen the ring radius distribution if the ring radius is left uncorrected.

In the case of the 120 GeV/ c thin target data, calibration of the effective index of refraction is easily achieved by measuring the radii of uninteracted protons. In a typical file with 5000 events one finds more than 1000 clean events with uninteracted protons. We

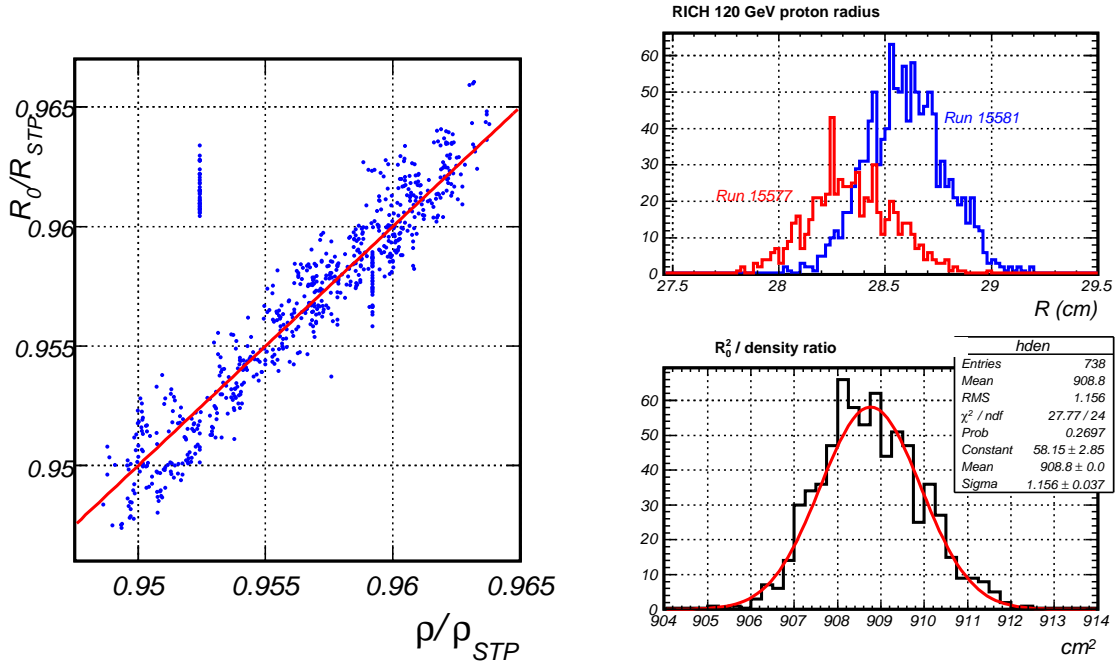


Figure 7.22: The left plot shows the dependence of RICH R_0^2 on the density of CO_2 , where both variables are divided by the respective values at STP. The few outliers come from subruns where the gas temperature or pressure are not recorded in the database. The $y = x$ line is superimposed to demonstrate that the expected linear dependence between R_0^2 and gas density is observed. The top right plot shows the difference in proton ring radius distributions in two nearby runs. The CO_2 pressure was raised between the two runs. The bottom right plot tells us that R_0^2 is known to about 0.1%.

can rewrite Equation 6.25 as

$$\frac{1}{2}R_0^2 = F^2 - \frac{F^2 - \frac{1}{2}R^2}{\sqrt{1 + m_{\text{prot}}^2/p_{\text{beam}}^2}}, \quad (7.5)$$

which allows us to compute R_0 from measured proton ring radius. Figure 7.22 shows the summary of RICH calibration thus obtained.

Chapter 8

Monte Carlo Simulation

Monte Carlo simulation was necessary in order to measure the reconstruction performance. In particular for this analysis, we need to know particle identification efficiency and backgrounds.

We used FLUKA-06 [24, 25] to simulate particle production and GEANT 3.21 [10] to transport particles through the spectrometer. GEANT hits (idealized energy deposition) were stored into the ROOT event tree, and hits were converted into digits (mock raw data) with packages written by the MIPP collaboration.

8.1 Time Projection Chamber Digitization

In order to get an accurate model of the TPC track, the following effects have to be modeled:

- Electron drifting in non-uniform magnetic field,
- Variations in gas gain due to different anode voltages,
- Diffusion of charge in space,
- Diffusion of charge in time,
- Electronic noise.

The TPC gas volume inside the field cage has dimensions of $104.4 \times 79.4 \times 162.8$ cm. It was segmented into $0.87 \times 1.05 \times 1.27$ cm rectangular parallelepipeds so that

GEANT could record hits at boundary crossings. The objective of digitization is to compute the ADC in each voxel. A voxel is defined as a time slice on a pad in a pad row.

8.1.1 Generating Digits

Starting from the hit position (x, y, z) , we drift the hit to the anode wire plane obtaining (x', y_{anode}, z') and the drift time t_d (see Section 7.5.2). A fourth-order Runge-Kutta stepper was implemented to do this, and with $0.5 \mu\text{s}$ steps it computed the distortion with a precision of about 1 micron, as tested by reversing the drift to restore the starting hit position.

Before the TPC digits are generated, (x', z', t_d) are converted to pad column, pad row, and time bucket $(x_{col}, x_{row}, t_{bkt})$ through

$$\begin{aligned}x_{col} &= (x' - x_{col,0})/L_{col} \\x_{row} &= (z' - x_{row,0})/L_{row} \\t_{bkt} &= (t_d - t_{trig})/T_{bkt}\end{aligned}$$

Here $x_{col,0}$ and $x_{row,0}$ are the locations of column 0 and pad 0, $L_{col} = 0.8 \text{ cm}$ and $L_{row} = 1.2 \text{ cm}$ are the pad sizes, and $T_{bkt} = 0.1 \mu\text{s}/\text{bucket}$. The trigger time t_{trig} is generated as a constant time offset plus a uniformly distributed $0 - 50 \text{ ns}$ jitter time. In data, this time offset is measured, and the jitter results from the fact that the TPC 20 MHz clock is not synchronized to the trigger time.

The next step is to spread the hit energy deposition over the pads, columns and buckets. To improve performance of the algorithm, we defined a 3-dimensional array of total charge in the TPC voxels. At the beginning of each event, the charge on each voxel is reset to 0. For each hit, we define a three dimensional energy density function as a product of a Gaussian in the pad columns centered at x_{col} , a Gaussian in the pad rows centered at x_{row} , and a gamma function in the buckets with the peak at t_{bkt} . The integral of the the function is set to the hit energy deposition multiplied by a gain factor, which is different for every anode section of the TPC. For each TPC voxel where the integral of the density function is at least 0.5 counts, the charge sum is incremented, and the track number that generated the hit is added to the track list associated with the voxel. Having the associated track list allows us to establish the correspondence between the reconstructed and the MC track.

In the course of the run, some anode regions were not able to hold the nominal high voltage of 1250 V, thus creating large dead regions in the TPC. Undoubtedly, the missing data has an adverse effect on the track finding algorithm, so it has to be modeled. Each anode region was assigned a different gain: the factor converting the GEANT hit energy deposition to the ADC value. Additional missing data comes from electronic problems as a number of sticks (two half pad rows) never read out. These sticks were turned off in the Monte Carlo simulation.

To generate the TPC digits, for each voxel on a good stick with at least 1 ADC count, we multiply the charge by a Gaussian random number centered at 1 to randomize the pad gain. Finally, we add a Gaussian pedestal and if the total charge in the voxel is above the threshold, it is written out.

8.1.2 Generating Noise

There are 3 sources of noise in the TPC:

1. Hot voxels;
2. Hot pads where all voxels are lit up or every other voxel is on;
3. Charged cosmic particles.

All of these sources of noise are typically well rejected by the TPC reconstruction algorithm. Cosmic particles are rare, and are not likely to go through the target, so they were not modeled. In order to speed up modeling of noise, a random Gaussian number of voxels was selected to be noisy in an event and their ADC spectrum was generated to be consistent with the data.

8.2 Wire Chamber Digitization

The GEANT hits in wire chamber planes are converted to hit wires by computing the number of drift cells that the track crossed and dividing the deposited energy equally between all the affected wires. A track number list is filled for every wire as the deposited energy is being added to the wires. Charge from all hits is integrated over all wires, and wires above the threshold are written out as digits. This approach makes it more difficult to tune the chamber efficiency than choosing a random number for each wire. However, it

is motivated by the physics of wire chambers, and makes it possible to simulate cross talk where it is most likely to happen given a distribution of particles at the chamber.

In addition to computing wires above threshold, the drift time needs to be calculated in the drift chambers. As the charge is being split between wires, the minimum distance from the track to the wire is stored. In the case where more than 2 drift cells are crossed, minimum distance is set to 0 for the inner wires. The minimum distance is converted into drift time using a linear relation between drift distance and drift time.

The final part of chamber digitization is to add cross talk. Cross talk on the discriminator/pre-amplifier cards was simulated by computing the total amount of charge on each card, and a fraction of that charge is added to all wires on the card. The common group is 8 wires in the drift chambers and 32 wires in the proportional chamber. If a wire that gets a cross talk contribution was not hit, its minimum drift distance is set to the smallest drift distance in the group in order to preserve causality.

8.3 RICH Hits and Digits

The Cherenkov photons in the RICH are generated by GEANT with a fixed gas density consistent with the average CO₂ density during the data taking. Over the year of running, the density in the RICH varied by about 1%. Given the fact that the detector can be easily calibrated (see Section 7.6) one gas density for the Monte Carlo simulation is sufficient.

To generate the PMT hits, photons are generated along the trajectory of the track according to the parametrized functional form of the index of refraction (see Figure 6.11). The photons are then transported to be reflected off the mirrors and then to the PMT array. Absorption in the CO₂, reflectivity of the mirrors, opacity of the quartz windows are taken into account in the transport of photons.

The digits are generated by choosing a random number between 0 and 1 for each photon. Photons with this number above PMT efficiency for the photon's wavelength generate digits.

Chapter 9

Data Analysis

The objective of the data analysis is to extract the ratios of the production of charged pions and kaons with momentum above 20 GeV/ c using 120 GeV/ c proton data on a 2% interaction length carbon target in bins of longitudinal and transverse particle momentum. With four particle species (K^\pm, π^\pm), there are a total of six ratios, although only three are mathematically independent. In practice, the four ratios of interest are those of like charges and like species, i.e. K^+/π^+ , K^-/π^- , K^-/K^+ , and π^-/π^+ , since systematic errors of the four ratios are different and the latter two ratios have been described phenomenologically[6] with a simple relation.

9.1 Data Binning

9.1.1 Geometric acceptance

Although the objective is to sample as much of (p_z, p_T) space as possible, geometric acceptance of the RICH is not perfect above 20 GeV/ c . Figure 9.1 shows acceptance of the PMT array for particles with ring centers within 5 cm of the edge of the array. At 20 GeV/ c momentum, a kaon ring radius is approximately 15 cm, so requiring the center to be within 5 cm of the PMT array ensures that a significant fraction of the ring can be detected by the PMTs.

Given the statistics of recorded proton carbon interactions and the fact that the transverse momentum spectrum is steeply falling (see Figure 9.2), we limit our attention to regions of space where the geometric acceptance of the RICH is at least 50%.

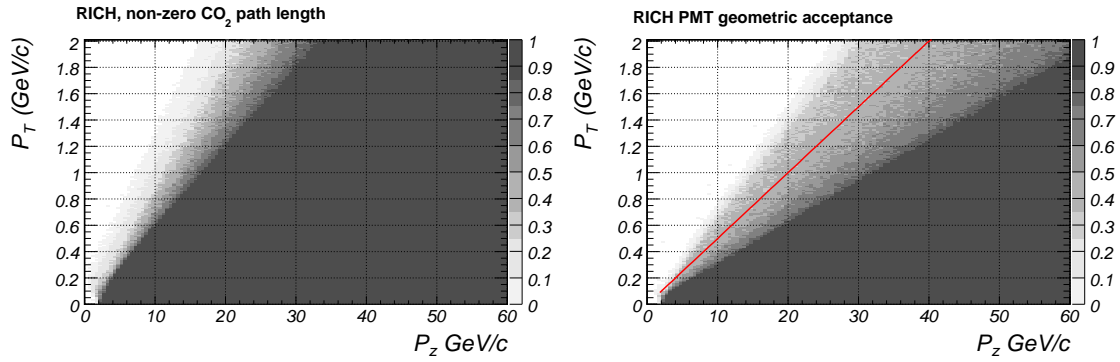


Figure 9.1: Geometric acceptances for the RICH radiator volume and the PMT array where the ring center is within 5 cm of the edge of the PMT array. Line $p_T = 0.05p_z$ shows the limit for 50% geometric acceptance by the photomultipliers.

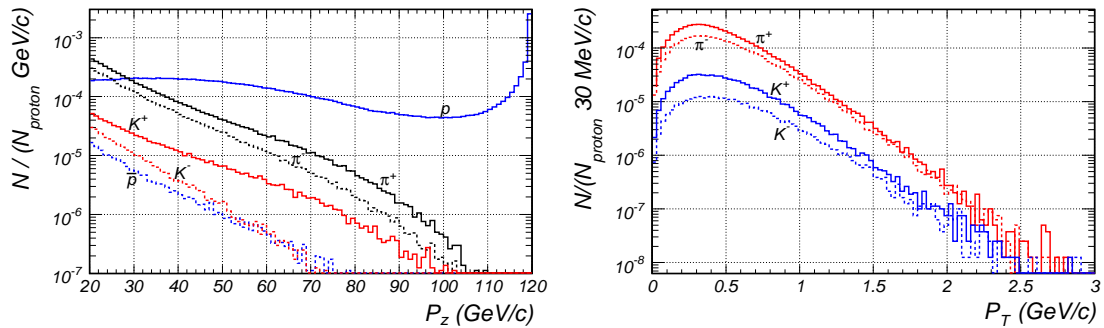


Figure 9.2: Charged hadron fluxes with longitudinal momentum above 20 GeV/c per incident proton as simulated by FLUKA-06 on 2% carbon target.

9.1.2 Bin Selection

The choice of upper and lower limits on p_z is governed by two considerations. The kaon threshold is around 17 GeV/ c , thus a 20 GeV/ c momentum lower limit with $\sim 5\%$ momentum resolution ensures minimal bias from the threshold effect, which we are unable to measure from the data at this time. Particle production with momenta above 90 GeV/ c is heavily dominated by inelastically scattered protons, so cutting the right bin at $p_z < 90$ GeV/ c will reduce the background underneath the K^+ peak and remove a small number of true kaons and pions.

In the limit of infinite statistics, one would like to have the smallest bins possible. However with $5 \cdot 10^5$ recorded triggers and estimated 50% interaction trigger purity, we must select sufficiently large bins in order to have a statistically significant measurement. Figure 9.3 shows bin by bin the expected number of π^+ from $2 \cdot 10^5$ proton-carbon interactions modeled in FLUKA-06. Of the four particles of interest, the π^+ is the majority particle, hence at the very least one needs to have a significant number of pions to do the measurement. The criteria used to select bin boundaries was to get 3% or better statistical error on π^+ if possible. On the other hand, the momentum resolution is at most 5.5%, so using that as the upper limit, we select at least 20% bins so that the effect of mixing between bins is minimized. The 24 bins defined for the measurement are shown in Table 9.1.

9.2 Pileup Removal

Resonant extraction from the Main Injector could not be tuned to guarantee a single particle per 10 μ s cycle in the machine, therefore a significant fraction of triggers contain two or more incident protons. While the probability of both protons to interact is small, pileup can create confusion in vertex finding and fitting. Since this bias is not modeled in the Monte Carlo (MC), it is best to remove pileup events from the analysis.

9.2.1 Determining Pileup Cuts

In order not to bias the measurement, pileup removal has to be done using information from detectors upstream of the target as much as possible. This includes

- Number of tracks in the beam chambers, and beam track time;
- Three scintillator counters (charge and hit time differences);

Bin	Minimum p_z	Minimum p_z	Maximum p_T	Maximum p_T
(0, 0)	20	24	0	0.2
(0, 1)	20	24	0.2	0.4
(0, 2)	20	24	0.4	0.6
(0, 3)	20	24	0.6	1.0
(1, 0)	24	31	0	0.2
(1, 1)	24	31	0.2	0.4
(1, 2)	24	31	0.4	0.6
(1, 3)	24	31	0.6	1.0
(1, 4)	24	31	1.0	1.2
(2, 0)	31	42	0	0.2
(2, 1)	31	42	0.2	0.4
(2, 2)	31	42	0.4	0.6
(2, 3)	31	42	0.6	1.0
(2, 4)	31	42	1.0	1.55
(3, 0)	42	60	0	0.2
(3, 1)	42	60	0.2	0.4
(3, 2)	42	60	0.4	0.6
(3, 3)	42	60	0.6	1.0
(3, 4)	42	60	1.0	2.0
(4, 0)	60	90	0	0.2
(4, 1)	60	90	0.2	0.4
(4, 2)	60	90	0.4	0.6
(4, 3)	60	90	0.6	1.0
(4, 4)	60	90	1.0	2.0

Table 9.1: (p_z, p_T) bins selected for ratio measurement.

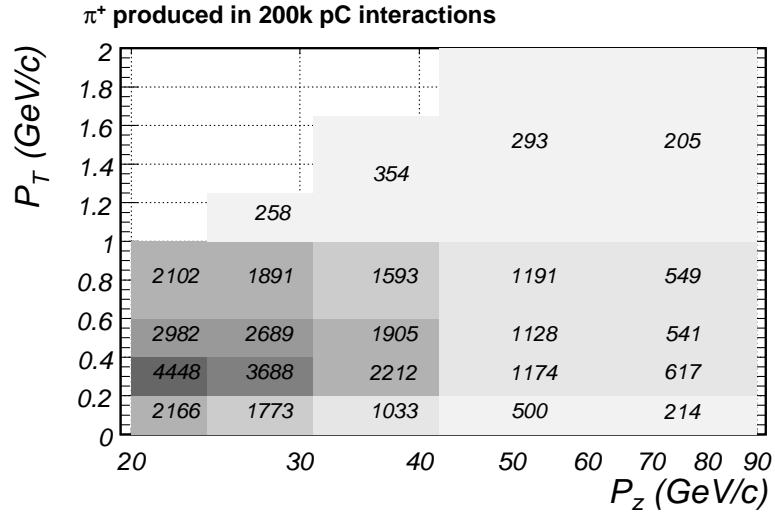


Figure 9.3: Expected number of π^+ particles in the bins selected for the ratio measurement. Bin boundaries in p_z are 20, 24, 31, 42, 60, 90 GeV/c, and in p_T 0.2, 0.4, 0.6, 1 GeV/c. The largest p_T bin stretches to 2 GeV/c or 0.05 of the lower bin boundary, which corresponds to 50% geometric acceptance.

- Four beam Cherenkov PMT signals (charge and hit times);
- Times of reconstructed secondary tracks.

For the purpose of finding variables to remove pileup, we can identify pileup events by looking at the amount of energy deposited by uninteracted proton tracks inside the TPC. Figure 9.4 shows that when two or more tracks are on top of one another, the TPC integrates the total ionization energy resulting in multiple peaks in dE/dx . One has to keep in mind that the chamber integrates over 15 μ s, while most detectors keep information in a 100 ns window, and chamber TDCs have 1 μ s window. Therefore a fraction of events which look like pileup in the TPC will create normal response in all other detectors.

Events with $dE/dx < 3$ were taken to come from clean events, whereas those with $dE/dx > 5$ were selected as pileup candidates. Figure 9.5 shows distribution of variables which are most helpful to select between clean and pileup events. In order of significance, we use the following cuts to remove pileup:

1. The number of beam tracks is greater than 1;
2. The average charge of beamline scintillator counters is greater than 1.8;

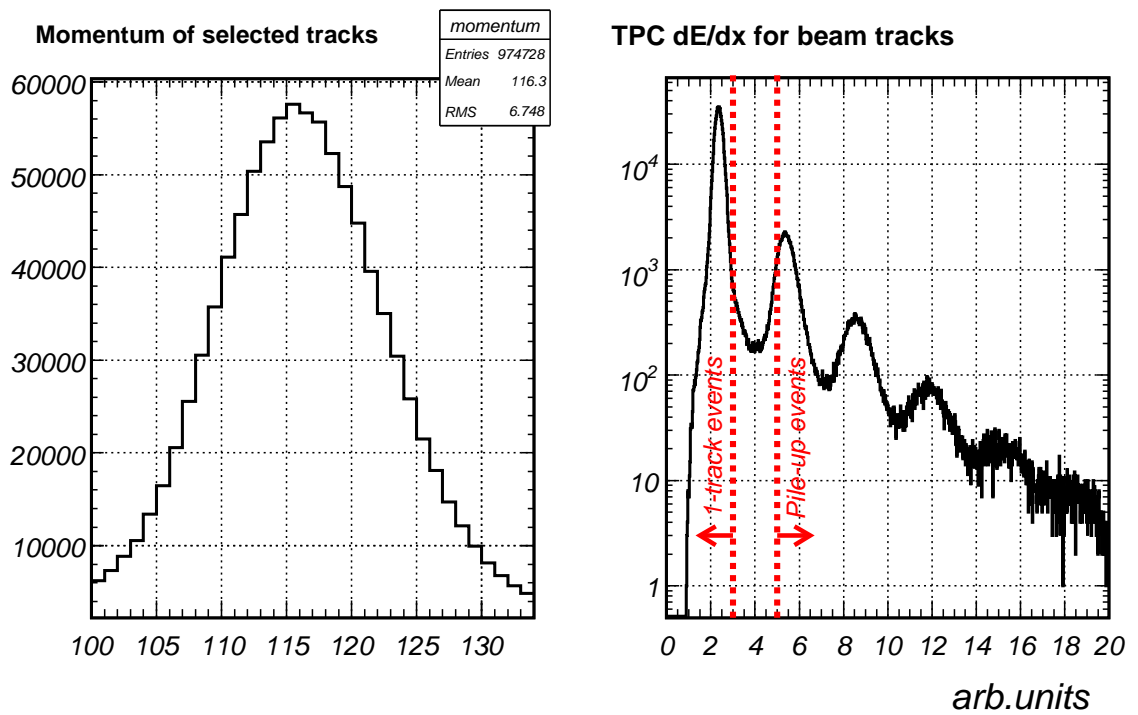


Figure 9.4: Momentum (in GeV/c) and energy loss of beam tracks in the TPC where single and pileup proton tracks are easily identified.

3. The beam track time is outside of -5 to 20 ns window;
4. Large (greater than 1 ns) time difference of signals in T0 counters;
5. The average charge of beam Cherenkov charge is greater than 330 ADC counts;
6. A TDC hit in the outer PMT of either beam Cherenkov (none are expected);
7. The TDC of the inner PMT on the upstream beam Cherenkov is outside of the 800 to 1040 window;
8. The TDC of the inner PMT on the downstream beam Cherenkov is outside of the 700 to 950 window;

One additional cut is placed on the time of secondary tracks. This is the only cut that does involve data from detectors downstream of the target. However, as Figure 9.6 shows, in case of single-proton tracks selected for pileup study, only 1% of events with no pileup candidates have out of time secondary tracks and 45% of pileup candidates have out of time secondary tracks. Thus, requiring that all tracks come in between -15 and 55 ns removes additional sources of pileup.

9.2.2 Effect of the Pileup Cuts

In addition to dE/dx in the TPC, a variable that helps us judge the performance of pileup removal is the amount of energy deposited in the hadron calorimeter. Figure 9.7 shows that the cuts clean up energy deposition in the TPC volume and in the hadron calorimeter. While about 20-40% of the data contains pileup after these simple cuts, less than 1% of the data contains events with pileup.

9.3 Primary Vertex Selection

With 6 mm vertex resolution in z , the cuts on target-like events need to be done in such a way so as not to introduce a bias into the measurement. We open a wide window to include both the target and the scintillator, and subtract appropriately scaled target-out data.

To determine the fraction of target-out data that needs to be subtracted from target-in data, we plot distributions of vertex z in each set in pileup free events. The shape

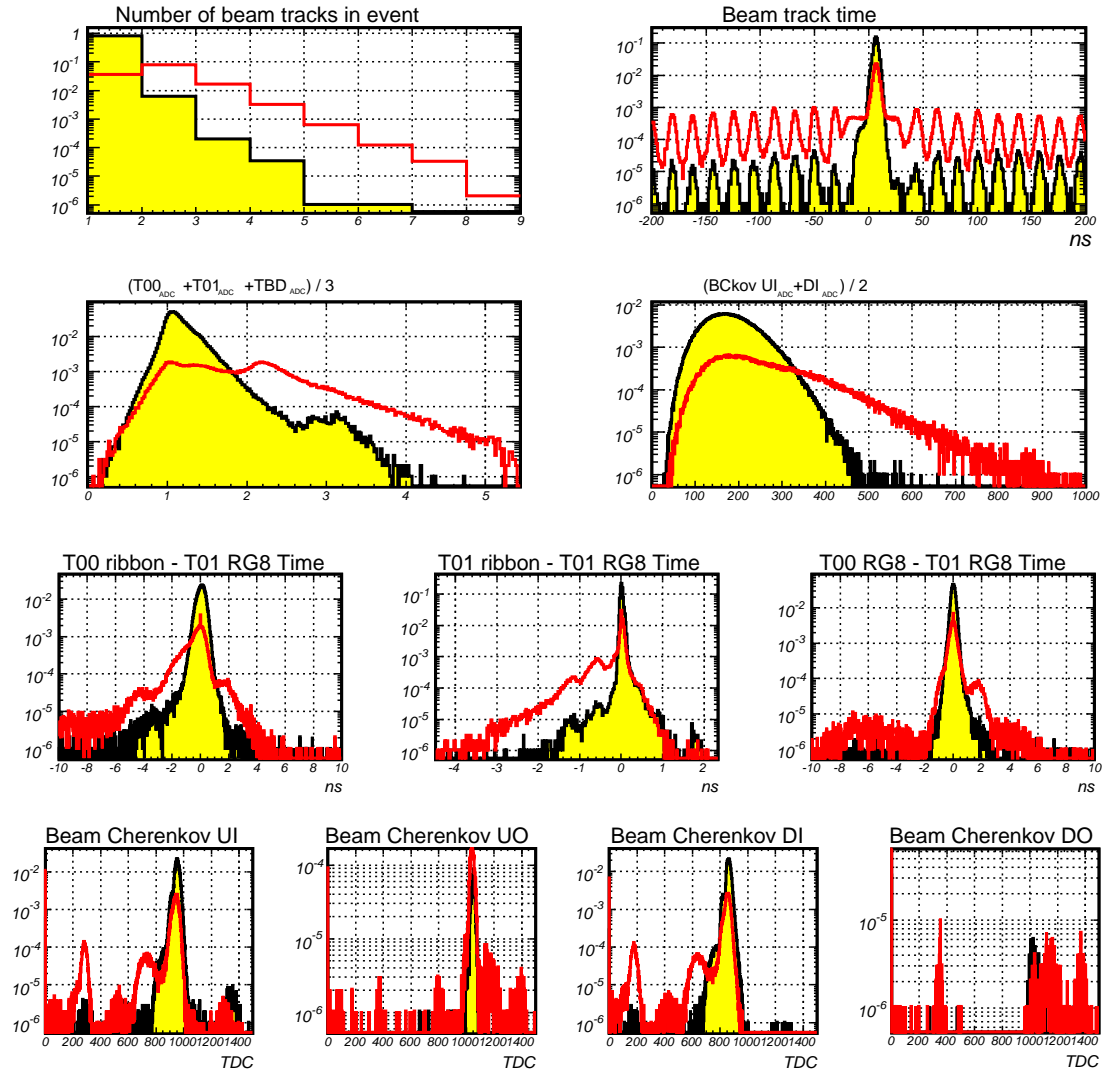


Figure 9.5: Distribution of variables that help distinguish pileup events from clean events. Shaded histograms are filled with information from single-track candidates, and non-shaded histograms from pileup candidate events. The histograms are scaled by the total number ($5.7 \cdot 10^5$) of proton tracks selected for the pileup study.

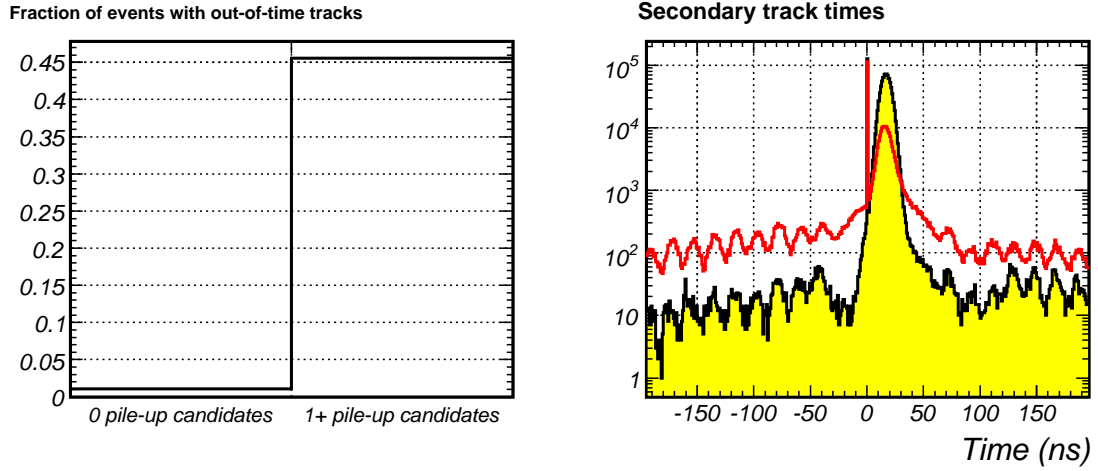


Figure 9.6: On the left is fraction of events containing out of time secondary tracks in single proton candidate and pileup candidate events. On the right is distribution of times for the two classes of events. The peak at 0 ns corresponds to tracks that have no information from the drift chambers.

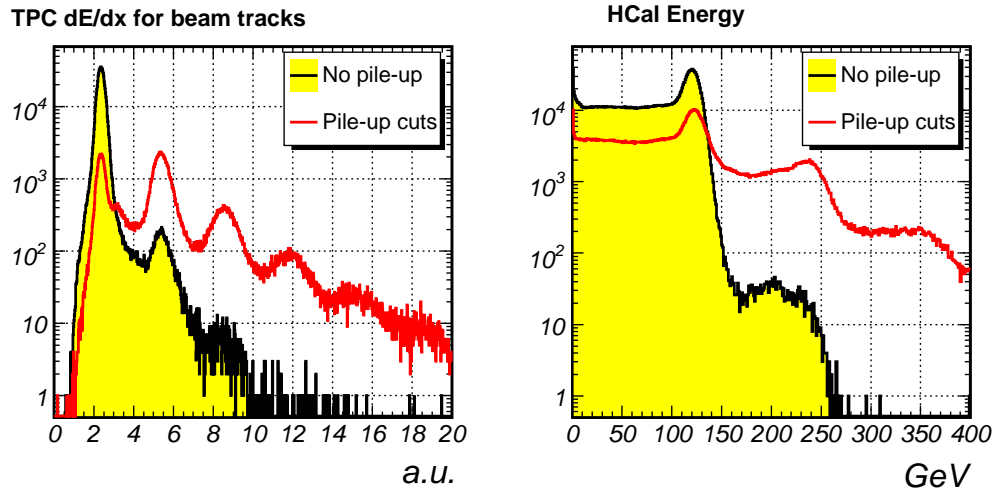


Figure 9.7: Pileup cuts are good at removing multiple peaks from TPC dE/dx of beam tracks and very high calorimeter energy. Less than 1.5% of beam tracks have measured dE/dx consistent with two or more particles and less than 0.5% of events deposit more energy than a single 120 GeV/c proton.

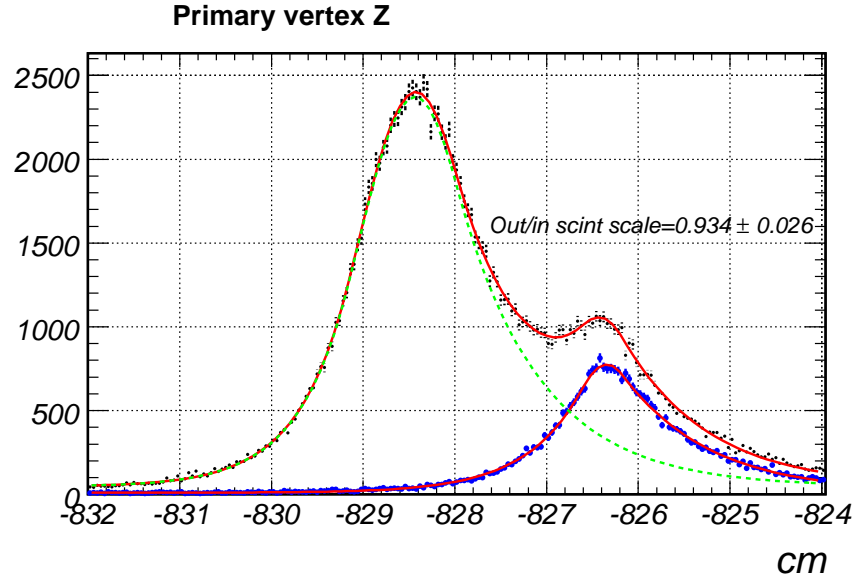


Figure 9.8: 2% carbon and target-out data. The scale factor of available thin target data is based on fitting a Gaussian with exponential tails to the target and the interaction counter.

of the z distribution is well described by a Gaussian with exponential tails on both sides plus a constant background. First, we make a fit to the target-out data to determine the shape of the trigger counter peak. To fit for the target in distribution, we hold all parameters of the scintillator peak fixed except for the amplitude. Figure 9.8 shows that this technique does a good job at fitting for the carbon data z distribution and tells us that the available target-out data needs to be scaled by 0.934 ± 0.026 before it is subtracted from the 2% carbon data to account for the presence of the scintillator behind the target. Based on this plot we can tell that by defining target region from -832 to -825 cm in z will eliminate any potential bias due to cuts.

9.4 Interaction Trigger Efficiency

The interaction trigger efficiency needs to be understood as multiplicities of events containing kaons and pions may be somewhat different. To remove bias from calculation of the efficiency, we selected interactions from events where minimum bias trigger recorded the event. For the study of interaction trigger efficiency, we selected events with no pileup and vertex z between -831 and -827 cm.

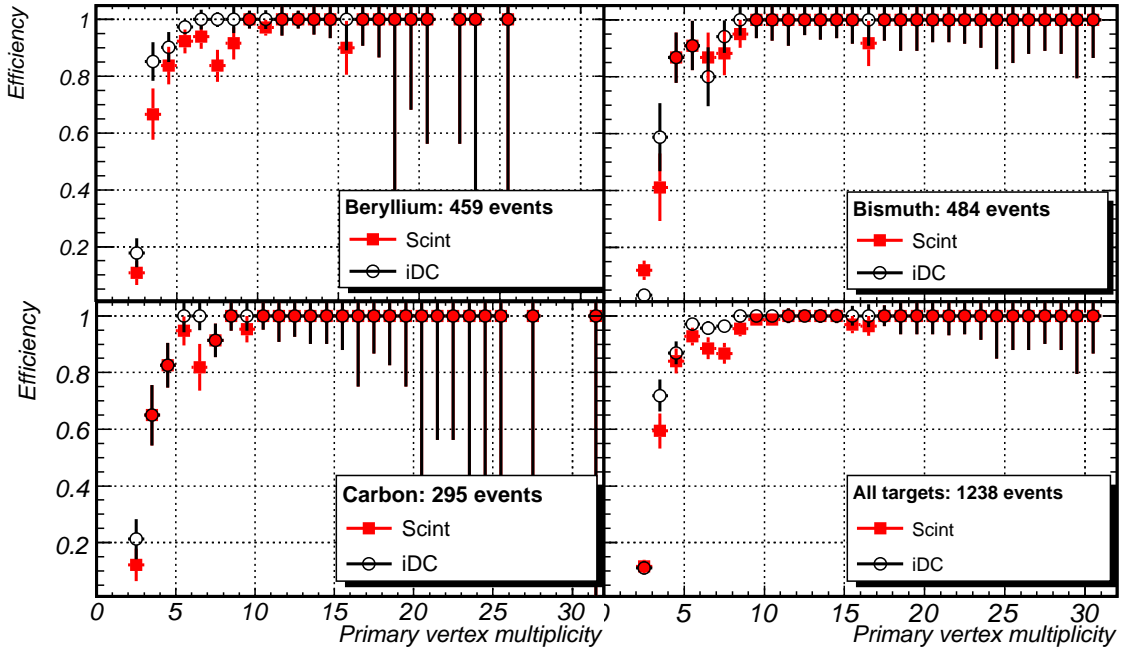


Figure 9.9: Interaction trigger efficiency for different targets at 120 GeV/c and the combined trigger efficiency for all targets.

Trigger efficiency does not only depend on the properties of the scintillator, but also on event topology. Therefore, it is not surprising that measured efficiency using beryllium or carbon data is different from efficiency computed using bismuth data. To quantify effect of the trigger efficiency, we rely upon the beryllium and carbon minimum bias events. We use the average iDC and Scint efficiency for the measurement. In each multiplicity bin, we take the highest efficiency of the four numbers as our upper limit and the lowest to get the lowest and the highest efficiency in each multiplicity bin (see Table 9.2).

9.5 Particle ID Variable

Computed mass squared using the RICH ring radius varies with particle p_z and p_T making it impossible to directly compare data and Monte Carlo simulation (see Figures 9.11 and 9.12). The source of this dependence is not currently understood. To make it possible to do data – Monte Carlo comparisons, we create a particle ID variable α through

$$\alpha(m^2) = a_{ij} + b_{ij}m^2, \quad (9.1)$$

	Vertex multiplicity							
	2	3	4	5	6	7	8	9
Highest efficiency	0.212	0.852	0.903	1.000	1.000	1.000	1.000	1.000
Lowest efficiency	0.107	0.650	0.826	0.923	0.818	0.837	0.916	0.952
Average efficiency	0.158	0.751	0.863	0.962	0.909	0.919	0.958	0.976

Table 9.2: Trigger efficiency using beryllium and carbon data. Highest/lowest efficiency is the highest/lowest number out of iDC-beryllium, iDC-carbon, Scint-beryllium, Scint-carbon values shown in Figure 9.9.

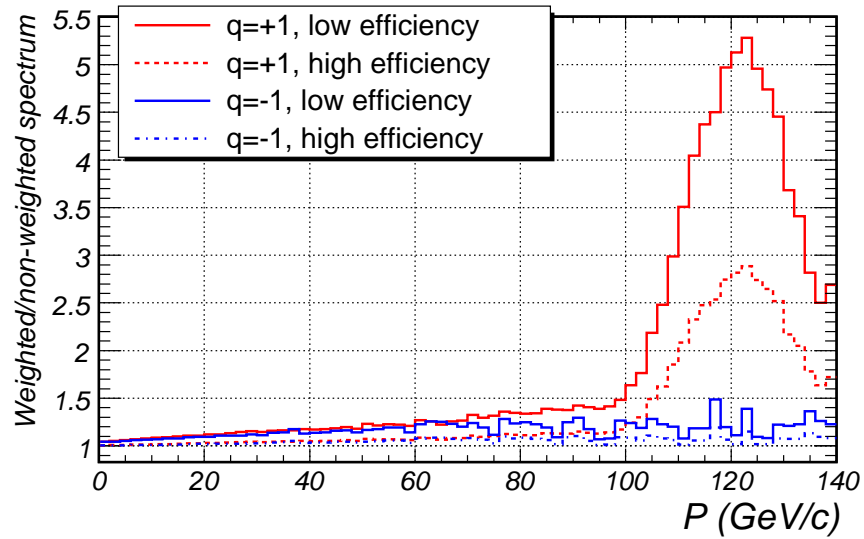


Figure 9.10: Combined carbon, beryllium, and target out momentum spectrum enhancement under the assumptions of the most efficient and the most inefficient trigger.

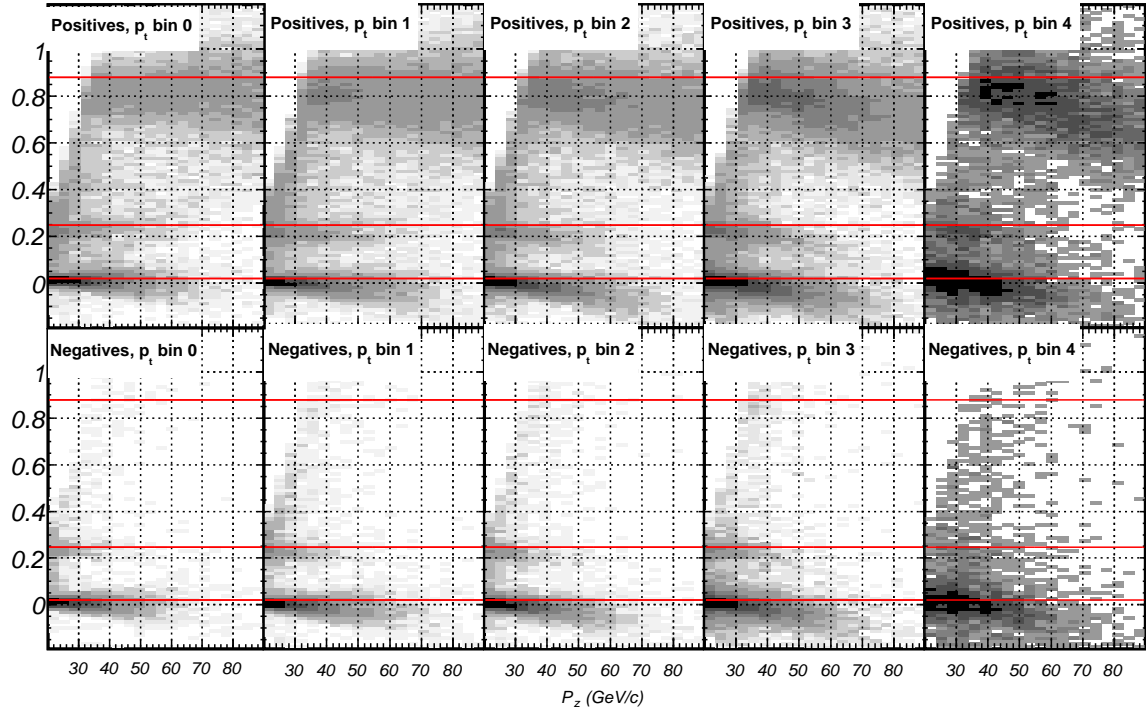


Figure 9.11: Variations of computed mass squared with p_z and p_t make it impossible to directly compare data and Monte Carlo. Superimposed are horizontal lines corresponding to mass squared of pions, kaons, and protons.

where a_{ij} and b_{ij} are different in each (p_z, p_T) bin. We defined $\alpha = 0$ to correspond to pion and $\alpha = 1$ to proton. Then kaon peak will be found at 0.265.

To find a_{ij} and b_{ij} , in each (p_z, p_t) bin we group negatives and positives from carbon, beryllium, and target out data together. Distributions of m^2 are fit for pion and proton peak or kaon if proton is under threshold in both data and Monte Carlo. Peak positions are then converted into coefficients through

$$b = [m_p^2 - m_\pi^2]^{-1} \quad (9.2)$$

$$a = -bm_\pi^2 \quad (9.3)$$

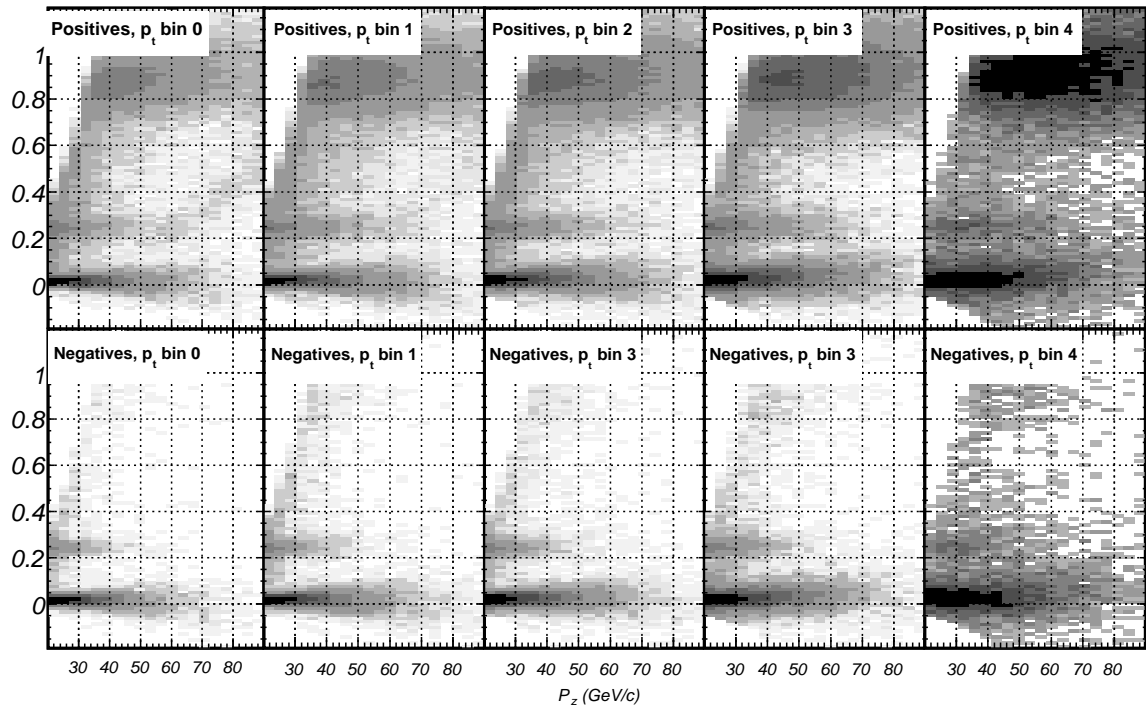


Figure 9.12: Variations of computed mass squared observed in data are not present in Monte Carlo.

p_z bin	p_t bin	Data				Monte Carlo	
		$m_\pi^2 \cdot 10^3$	$m_p^2 \cdot 10^3$	$a_{ij} \cdot 10^3$	b_{ij}	$a_{ij} \cdot 10^3$	b_{ij}
0	0	12.9 ± 0.1	228.4 ± 1.2	-15.9	1.230	-23.8	1.171
0	1	8.4 ± 0.1	229.3 ± 0.9	-10.1	1.199	-25.3	1.175
0	2	8.5 ± 0.1	229.8 ± 1.1	-10.1	1.197	-25.7	1.170
0	3	12.2 ± 0.2	228.2 ± 1.2	-14.9	1.226	-26.1	1.172
1	0	11.0 ± 0.2	228.4 ± 1.2	-13.4	1.219	-23.1	1.161
1	1	4.0 ± 0.1	222.8 ± 0.9	-4.8	1.211	-26.2	1.175
1	2	2.3 ± 0.1	223.3 ± 0.7	-2.8	1.199	-27.5	1.172
1	3	4.2 ± 0.2	225.5 ± 1.1	-5.1	1.198	-27.2	1.169
1	4	13.3 ± 1.4	219.2 ± 3.4	-17.2	1.287	-29.0	1.168
2	0	8.2 ± 0.3	794.5 ± 2.2	-10.5	1.272	-22.3	1.208
2	1	-3.6 ± 0.2	792.4 ± 1.3	4.6	1.256	-27.1	1.211
2	2	-8.9 ± 0.2	799.4 ± 1.2	11.1	1.237	-32.4	1.202
2	3	-9.2 ± 0.3	804.7 ± 1.3	11.3	1.229	-32.4	1.196
2	4	-1.9 ± 1.3	803.3 ± 3.9	2.4	1.242	-32.7	1.188
3	0	2.0 ± 0.8	810.0 ± 1.7	-2.5	1.238	-15.8	1.147
3	1	-15.3 ± 0.6	807.6 ± 1.0	18.5	1.215	-22.0	1.150
3	2	-27.2 ± 0.6	797.4 ± 1.0	32.9	1.213	-31.9	1.160
3	3	-33.1 ± 0.6	791.0 ± 1.0	40.2	1.214	-40.1	1.164
3	4	-27.6 ± 1.9	810.1 ± 2.8	33.0	1.194	-38.9	1.151
4	0	-11.9 ± 2.8	813.6 ± 1.7	14.4	1.211	-8.6	1.111
4	1	-34.7 ± 2.0	793.6 ± 1.2	41.9	1.207	-11.5	1.116
4	2	-58.2 ± 2.2	766.3 ± 1.3	70.6	1.213	-24.8	1.132
4	3	-67.5 ± 2.2	744.2 ± 1.4	83.2	1.232	-48.7	1.150
4	4	-80.9 ± 5.7	726.7 ± 3.5	100.1	1.238	-61.2	1.150

Table 9.3: Coefficients for conversion from m^2 in GeV^2/c^4 into particle ID variable α . For p_z bins 0 and 1, the numbers were computed using pion and kaon peak since proton is under threshold below $31 \text{ GeV}/c$. Ideal $a_{ij} = -22.45 \cdot 10^{-3}$ and $b_{ij} = 1.162 (\text{GeV}/c^2)^2$.

9.6 Corrections from Monte Carlo Simulation

9.6.1 Need for Corrections

A number of effects that one cannot easily extract from data must be corrected for. These include

1. Interactions in the spectrometer: about 10% of secondary particles will interact before reaching the RICH;
2. Interactions in the RICH flange: about 10% of particles passing through the flange rather than the RICH window will interact;
3. Decay in flight: about 10% of kaons will decay before they reach the RICH;
4. Particle misidentification due to RICH efficiency and ring fitting efficiency;
5. Particle misidentification due to multiple scattering: large angle scattering of a small fraction of protons (majority particle above ~ 30 GeV/ c) will create a measurable contamination, especially under the kaon peak;
6. Decay products of neutral particles (e.g. K_S , Λ) that get incorrectly pulled into the primary vertex.
7. Interactions in the trigger counter;

Figures 9.13 and 9.14 show that data and Monte Carlo distributions of the particle ID variable compare well in most bins, although Monte Carlo peaks are somewhat narrower.

9.6.2 Background Modeling

In order to extract correct numbers of pions and kaons, one has to evaluate the shape of the background in the particle ID variable and subtract the background from underneath the peaks. Figure 9.15 shows distribution of reconstructed Monte Carlo mass squared in one of the bins. As one would expect, protons are the primary source of background under the kaon peak in the bin where protons are under threshold. What is more surprising that a significant number of true protons get identified as pions. The possible explanations for this are

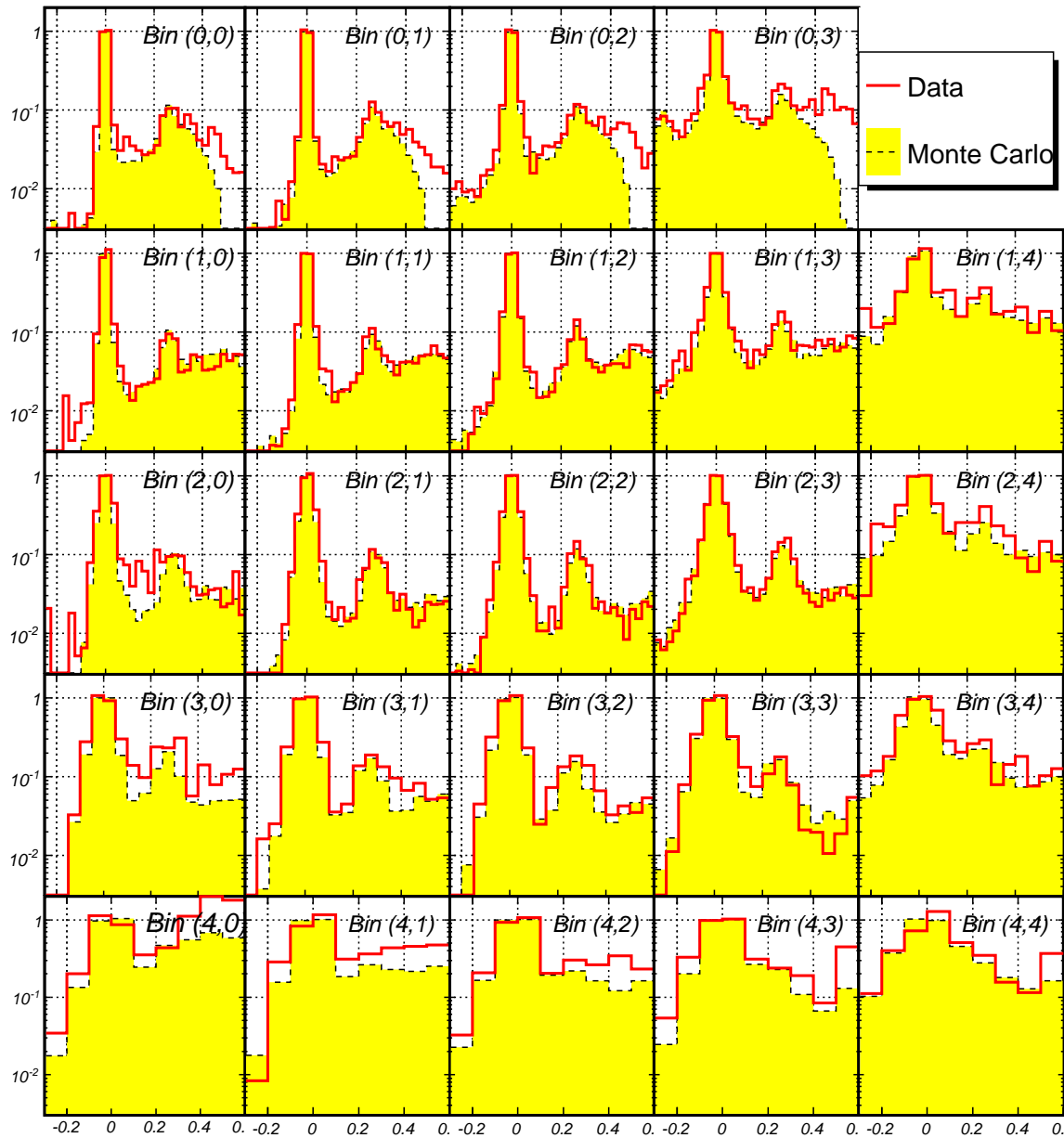


Figure 9.13: Data – Monte Carlo comparison of particle ID variable distributions for positives in the (p_z, p_t) bins. Histograms are normalized to set the pion peak to 1.

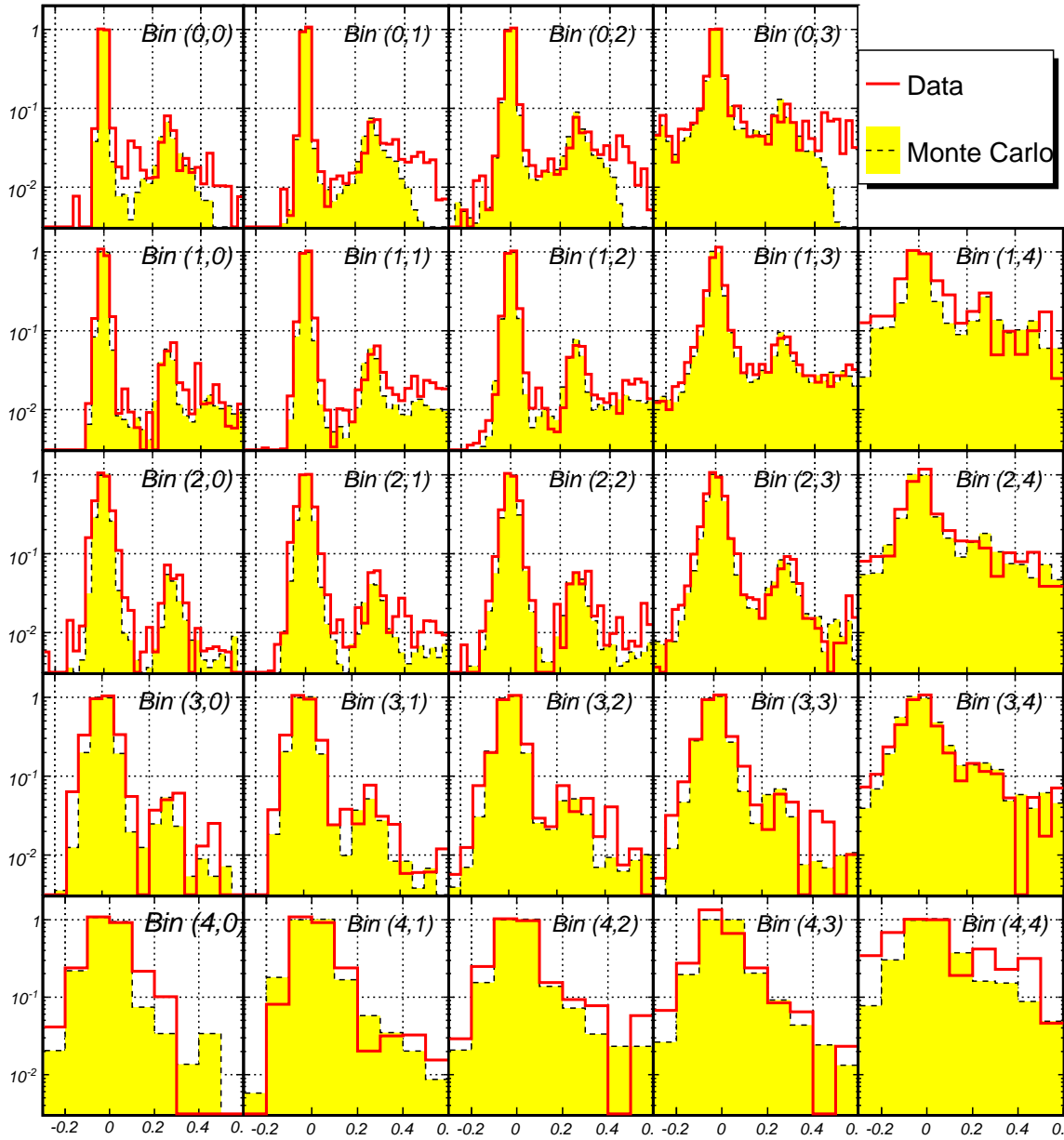


Figure 9.14: Data – Monte Carlo comparison of particle ID variable distributions for negatives in the (p_z, p_t) bins. Histograms are normalized to set the pion peak to 1.

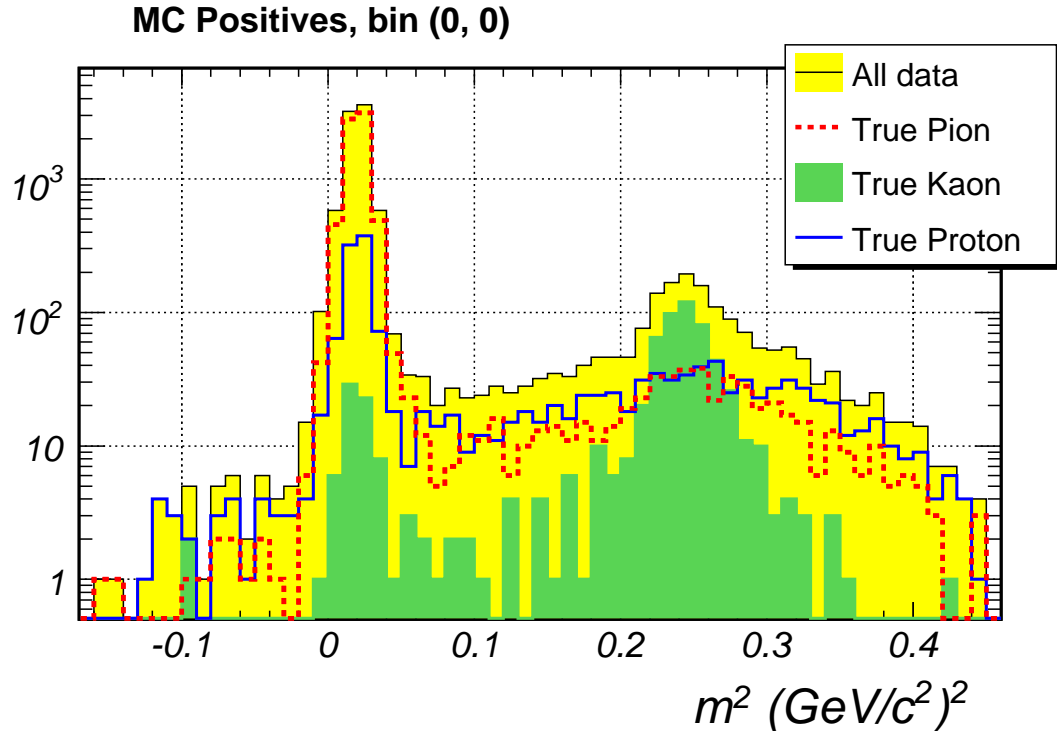
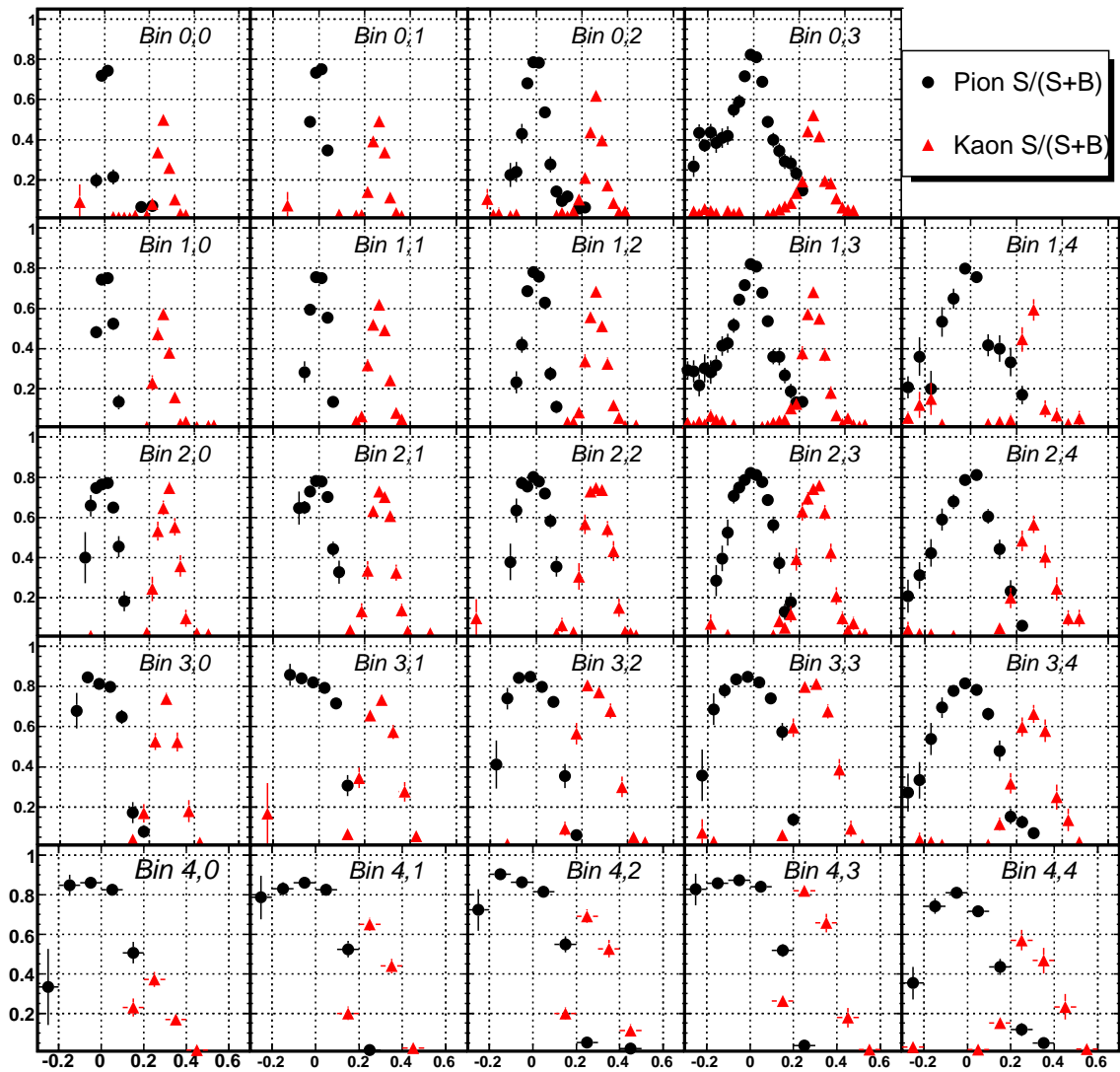


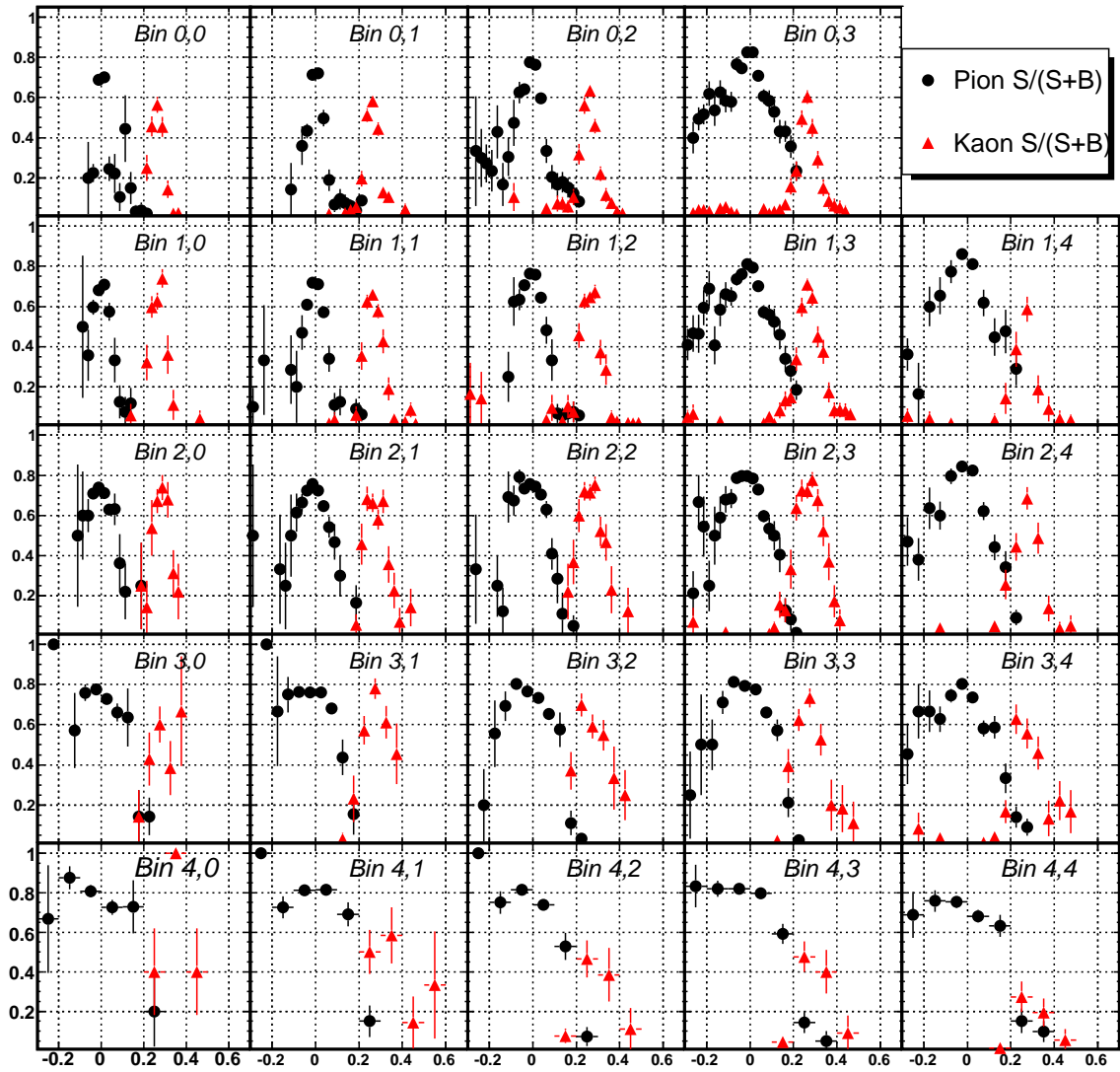
Figure 9.15: Reconstructed Monte Carlo mass squared in the first bin. It is clear that background has to be subtracted in order to extract correct number of kaons.

- Protons interacting in the spectrometer that create a forward pion or electron so that the track is extended into the RICH and gets identified as a pion;
- Incorrect association of reconstructed to true track.

The data – Monte Carlo comparison is the best model of background that we have, so to extract the signal from the background, we use true Monte Carlo information to extract the occupancy o of pions and kaons in the bins of particle ID histograms. Pion (kaon) occupancy is defined as the fraction of true pions (kaons) with reconstructed momentum within 4σ of true momentum. The highest occupancy (see Figures 9.16 and 9.17) almost never goes above 0.8. The order of magnitude of the maximum pion occupancy is consistent with our expectation that $\sim 14\%$ of protons will interact in the spectrometer. Note that to first order the occupancy does not depend on the Monte Carlo π/K ratio in a given bin, but it does depend on the number of protons relative to pions and kaons.

Equipped with the occupancy in each bin, we apply it to the data sample multiplying every bin of the data binned the same way by the computed occupancy. Then the

Figure 9.16: Occupancy of positive pions and kaons in Monte Carlo in the (p_z, p_t) bins.

Figure 9.17: Occupancy of negative pions and kaons in Monte Carlo in the (p_z, p_t) bins.

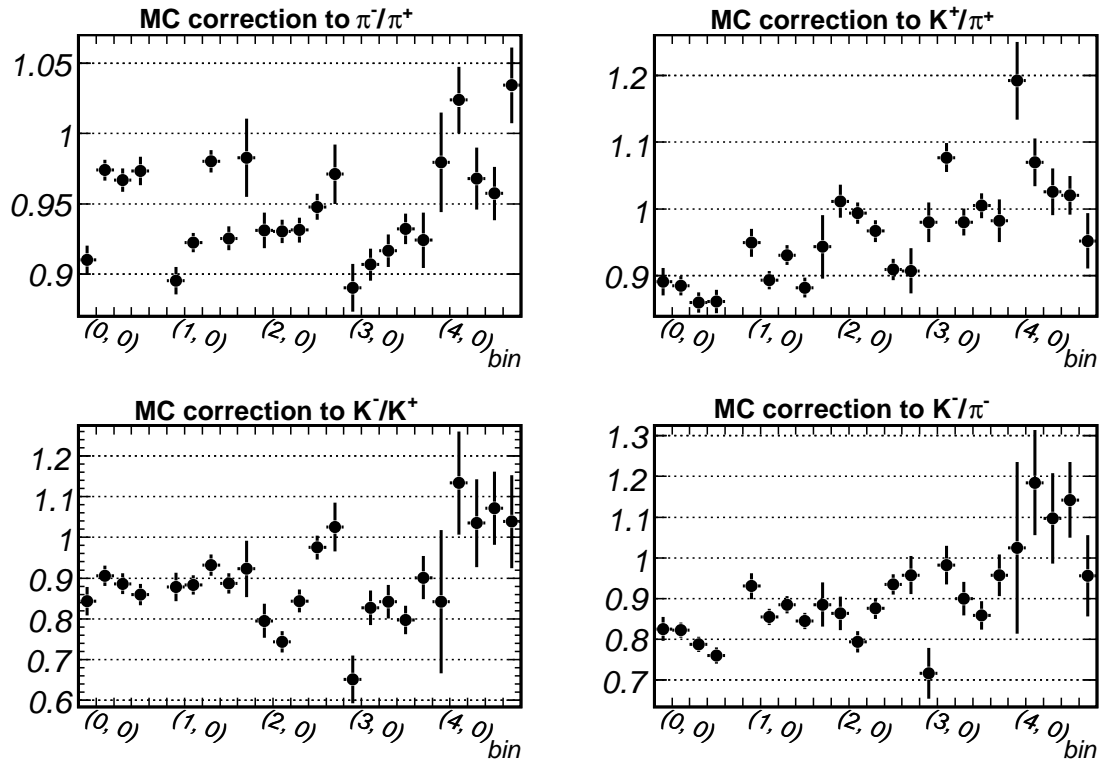


Figure 9.18: Ratios of reconstructed Monte Carlo ratios and true Monte Carlo ratios. The error bars come from propagation of statistical errors on the ratios, which are correlated between the reconstructed and true ratios.

number of pions in kaons is simply the integral of the derived histograms. The error on the count of particles is the sum of errors in each bin added in quadrature.

9.7 Corrections and Errors

We can judge how well the analysis method performs by comparing ratios derived from reconstructed Monte Carlo to true ratios in each (p_z, p_T) bin. Results shown in Figure 9.18 indicate that typical corrections are less than 10%. Given our current modeling of detectors in the Monte Carlo simulation, we will assign a conservative 50% systematic uncertainty on the applied correction.

As expected, errors associated with imperfect knowledge of interaction trigger efficiency are quite small with the exception of the bins which have little statistics. To compute the error associated with trigger efficiency, we compute the ratios using the upper

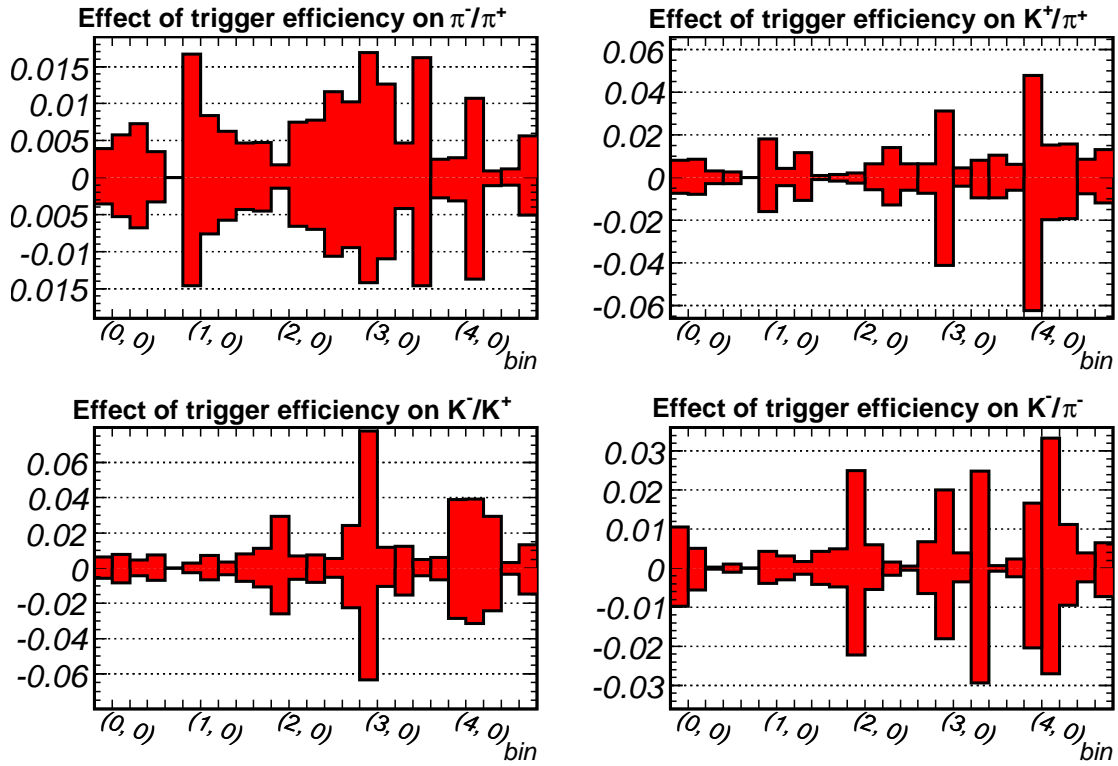


Figure 9.19: Effect of knowledge of interaction trigger efficiency on the ratios is quite small.

estimate of efficiency, giving each identified particle the weight equal to inverse of efficiency. We then repeat the process with the lowest estimate of efficiency and compute the quantity

$$\frac{r_\epsilon - r_0}{r_\epsilon + r_0}. \quad (9.4)$$

Here r_ϵ is the ratio measured given the assumption on trigger efficiency, and r_0 is the ratio derived using the average efficiency.

Another small error comes from the subtraction of signal associated with the particle production on the scintillator interaction trigger. The results of fits of a Gaussian with exponential tails (Figure 9.8) give a 2.5% uncertainty on target out subtraction. Figure 9.20 shows that even if we assume a 5% uncertainty on the fraction, this affects the ratios by less than 0.5%.

The largest systematic error comes from modeling of background using the Monte Carlo. To compare how well data and Monte Carlo simulation agree, we normalize data and Monte Carlo particle ID distributions by the average number of pion events in the central two bins of the pion peak (see Figures 9.16 and 9.17). We then compute the amount of pion

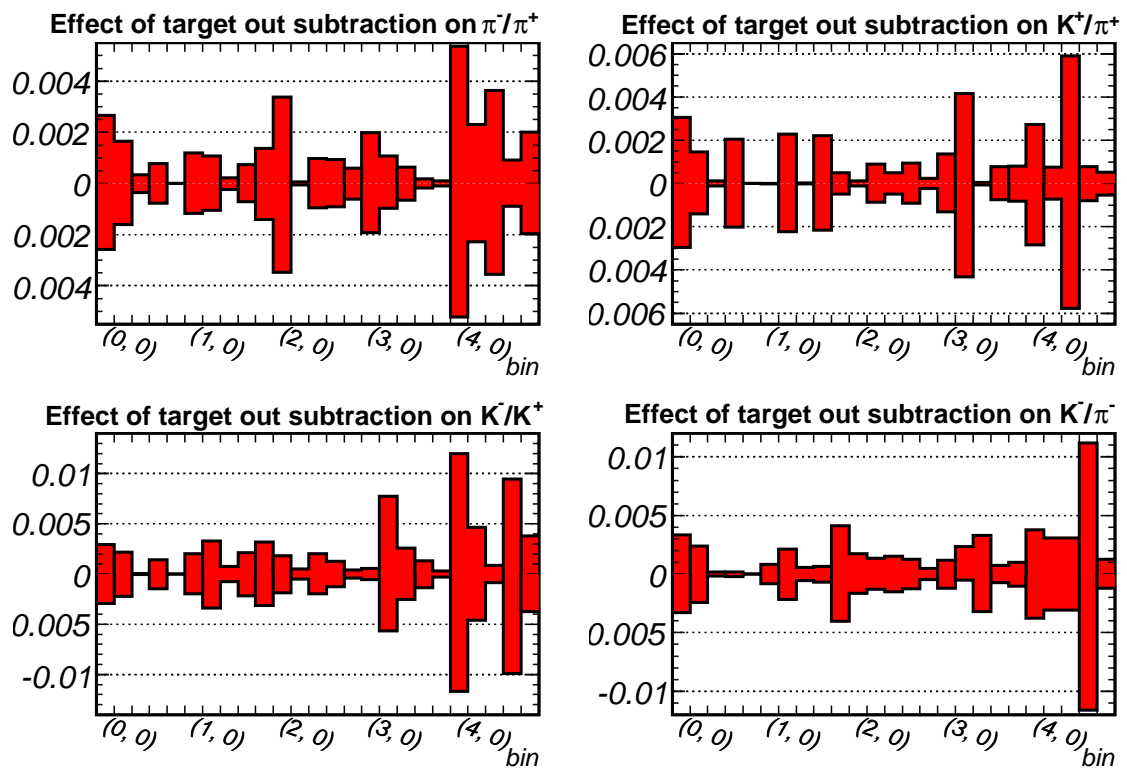


Figure 9.20: Effect on the ratio from 5% change in target out scale factor.

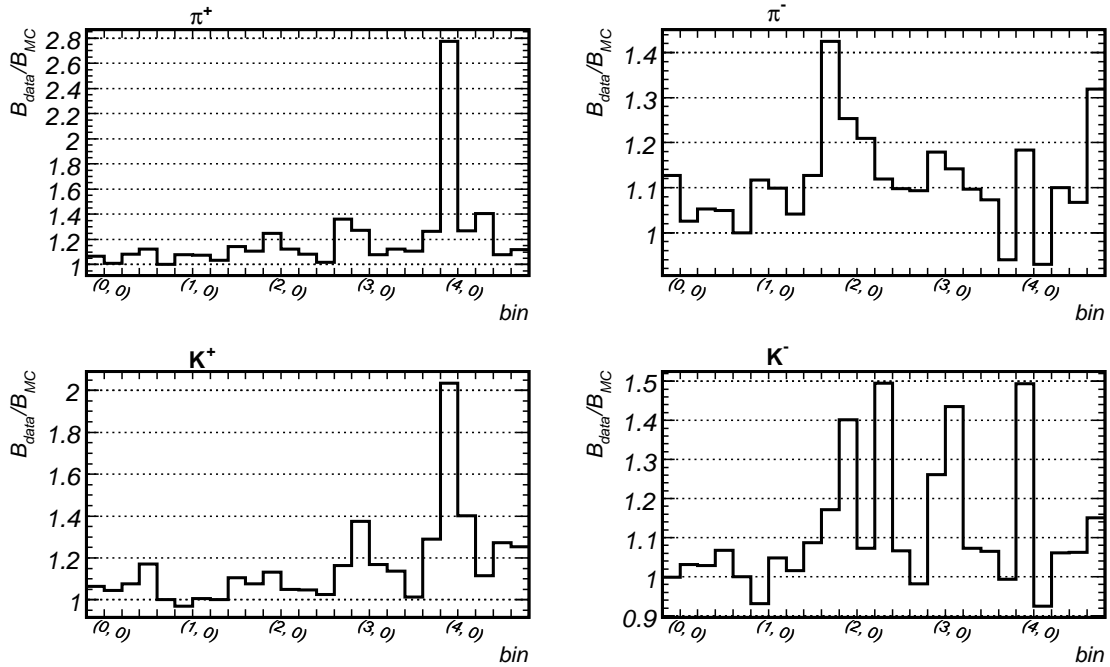


Figure 9.21: Data/Monte Carlo background ratio. In most bins, agreement between data and Monte Carlo is 10% or better. Bin (4, 0) has the largest proton background and is not well modeled by the Monte Carlo.

(kaon) background in those bins where pion (kaon) occupancy is non-zero. The ratio of data/Monte Carlo background, plotted in Figure 9.21, shows that in general the amount of background is larger in data than in Monte Carlo. The ratio would be 1 (within statistical error) if detector modeling is very accurate, and the relative numbers of protons, kaons, and pions are correct in the Monte Carlo. Since particle ID distributions are narrower in the Monte Carlo than in the data, one expects the ratio to be larger than 1.

To judge the sensitivity of measured ratios to background modeling, we increase and decrease $(1 - o)$ in the bins where we expect to find signal. The factor by which background is changed for each particle species is derived from the ratio of data/MC backgrounds, and is set to be at least 1.1 (the average of background ratios over all (p_z, p_T) bins). We then plot the difference from ratios computed with nominal occupancy using Equation 9.4. Results shown in Figure 9.22 are consistent with expectations. The effect on the π^-/π^+ ratio is small, since pion signal has little background. The larger effect on the K^-/K^+ ratio stems in part from low statistics. By far the largest effect of background modeling is on the K^\pm/π^\pm ratios. The reason is that the level of background under the

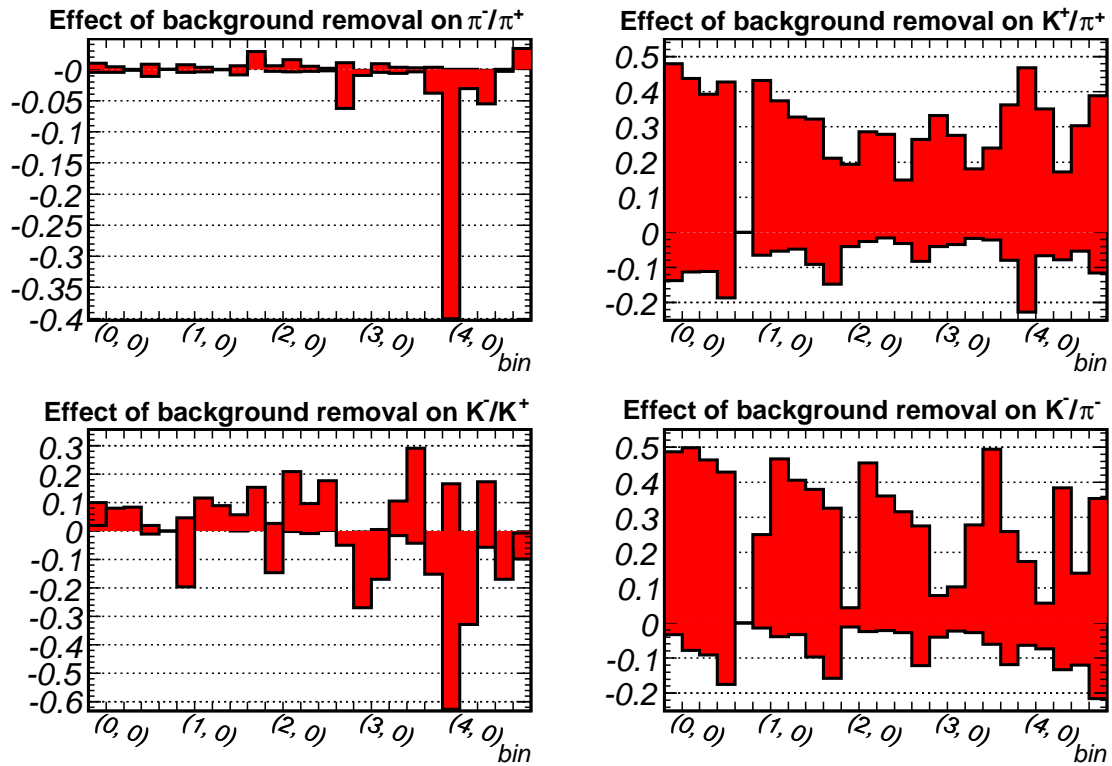


Figure 9.22: Systematic error from background subtraction. See text for explanation.

kaon peaks is significantly higher than under the pion peaks. Thus, decreasing $(1 - o)$ by 10% can boost the ratio by up to 50%.

Chapter 10

Results

10.1 Production Ratios

Equipped with Monte Carlo corrections and errors described in the previous chapter, we derive the ratios plotted in Figure 10.1 and listed in Tables 10.1, 10.2, 10.3, and 10.4. The ratios of like charges are consistent with FLUKA-06 predictions. However we find the predicted π^-/π^+ and K^-/K^+ ratios are higher by as much as 50% than the ratios derived in this measurement. The tendencies in both this measurement and FLUKA predictions are to decrease the π^-/π^+ and K^-/K^+ ratios with increasing p_z and increase the ratios with increasing p_T , although with different slopes.

10.2 Comparison to Existing Data

Results presented here compare well with the existing data sets (see Figures 10.2 and 10.3). For comparison, we define x_F using the proton mass. The π^-/π^+ ratio in our highest momentum bin (60-90 GeV/c) is significantly higher than the ratios derived from existing data. At this time, the reason for this discrepancy is not known.

It is also interesting to compare this measurement to the BMPT parametrization of 400 GeV/c protons on beryllium target[6]. Despite the fact that proton momentum is much higher, the parametrization does a good job describing behavior of ratios. The only exception is that in the parametrization π^-/π^+ ratio is independent of p_T . This measurement and the ratio from NA49 indicates that this is not exactly so in the highest p_T bin, which is not surprising as the model was derived using data with $p_T \leq 0.5$ GeV/c.

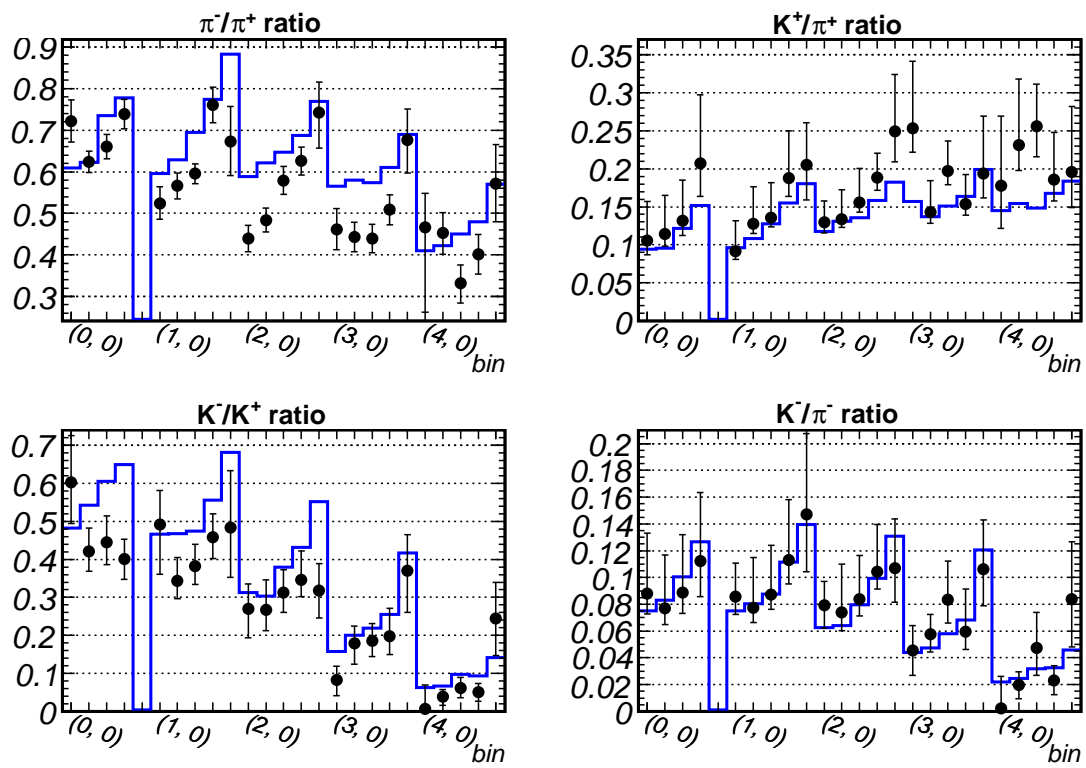


Figure 10.1: Measured ratios compared to particle production simulated with FLUKA-06 on 2% carbon target

Bin	p_z (GeV/c) p_t (GeV/c)		π^-/π^+	Errors in percent					
				Statistical	Total systematic	MC Correction	Trigger efficiency	Target out subtraction	Background modeling
(0, 0)	21.9	0.13	$0.722^{+0.051}_{-0.050}$	5.2	$+4.8$ -4.7	4.6	$+0.4$ -0.4	$+0.3$ -0.3	$+1.0$ -0.5
(0, 1)	21.9	0.30	$0.624^{+0.025}_{-0.025}$	3.7	$+1.7$ -1.7	1.5	$+0.6$ -0.5	$+0.2$ -0.2	$+0.4$ -0.5
(0, 2)	21.9	0.50	$0.661^{+0.029}_{-0.029}$	3.9	$+2.0$ -2.0	1.9	$+0.7$ -0.7	$+0.0$ -0.0	$+0.0$ -0.1
(0, 3)	22.0	0.74	$0.739^{+0.035}_{-0.036}$	4.4	$+1.9$ -2.1	1.7	$+0.4$ -0.3	$+0.1$ -0.1	$+0.9$ -1.1
(1, 0)	27.1	0.13	$0.524^{+0.039}_{-0.039}$	4.9	$+5.7$ -5.6	5.3	$+1.7$ -1.5	$+0.1$ -0.1	$+0.8$ -0.5
(1, 1)	27.1	0.30	$0.566^{+0.031}_{-0.031}$	3.8	$+4.1$ -4.0	3.9	$+0.8$ -0.8	$+0.1$ -0.1	$+0.3$ -0.4
(1, 2)	27.2	0.49	$0.595^{+0.024}_{-0.024}$	3.8	$+1.4$ -1.4	1.3	$+0.6$ -0.6	$+0.0$ -0.0	$+0.0$ -0.0
(1, 3)	27.3	0.75	$0.761^{+0.043}_{-0.043}$	4.0	$+3.9$ -4.0	3.8	$+0.5$ -0.4	$+0.1$ -0.1	$+0.6$ -0.9
(1, 4)	27.5	1.08	$0.673^{+0.084}_{-0.082}$	11.8	$+4.2$ -3.0	3.0	$+0.5$ -0.4	$+0.1$ -0.1	$+2.9$ 0.0
(2, 0)	35.6	0.13	$0.439^{+0.032}_{-0.032}$	6.2	$+3.8$ -3.7	3.7	$+0.2$ -0.1	$+0.3$ -0.3	$+0.6$ -0.3
(2, 1)	35.5	0.30	$0.483^{+0.029}_{-0.028}$	4.4	$+4.0$ -3.7	3.6	$+0.7$ -0.7	$+0.0$ -0.0	$+1.6$ -0.4
(2, 2)	35.6	0.50	$0.579^{+0.034}_{-0.033}$	4.5	$+3.7$ -3.6	3.6	$+0.8$ -0.7	$+0.1$ -0.1	$+0.6$ -0.3
(2, 3)	35.6	0.76	$0.626^{+0.034}_{-0.034}$	4.5	$+3.0$ -3.0	2.8	$+1.2$ -1.1	$+0.1$ -0.1	$+0.2$ -0.2
(2, 4)	36.0	1.19	$0.743^{+0.073}_{-0.086}$	9.3	$+3.0$ -6.8	2.6	$+1.0$ -0.9	$+0.1$ -0.1	$+1.1$ -6.2
(3, 0)	48.6	0.13	$0.462^{+0.050}_{-0.050}$	8.9	$+6.1$ -6.1	5.8	$+1.7$ -1.4	$+0.2$ -0.2	$+0.0$ -1.0
(3, 1)	48.9	0.30	$0.443^{+0.036}_{-0.036}$	6.4	$+5.1$ -5.0	4.8	$+1.3$ -1.1	$+0.1$ -0.1	$+1.0$ -0.5
(3, 2)	49.2	0.50	$0.439^{+0.034}_{-0.034}$	6.5	$+4.4$ -4.4	4.4	$+0.5$ -0.4	$+0.1$ -0.1	$+0.4$ -0.6
(3, 3)	48.8	0.76	$0.509^{+0.036}_{-0.036}$	5.9	$+3.9$ -3.9	3.6	$+1.6$ -1.5	$+0.0$ -0.0	$+0.3$ -0.4
(3, 4)	49.0	1.25	$0.676^{+0.075}_{-0.079}$	10.1	$+4.4$ -5.8	4.4	$+0.2$ -0.3	$+0.0$ -0.0	$+0.4$ -3.8
(4, 0)	69.6	0.13	$0.467^{+0.082}_{-0.204}$	17.2	$+3.8$ -40.3	3.8	$+0.3$ -0.3	$+0.5$ -0.5	$+0.0$ -40.1
(4, 1)	69.1	0.30	$0.452^{+0.049}_{-0.051}$	10.5	$+2.8$ -4.2	2.6	$+1.1$ -1.4	$+0.2$ -0.2	$+0.0$ -3.1
(4, 2)	68.1	0.49	$0.332^{+0.044}_{-0.047}$	12.9	$+2.8$ -6.2	2.8	$+0.1$ -0.1	$+0.4$ -0.4	$+0.0$ -5.5
(4, 3)	68.8	0.77	$0.402^{+0.047}_{-0.047}$	11.4	$+2.9$ -2.9	2.9	$+0.1$ -0.1	$+0.1$ -0.1	$+0.0$ -0.3
(4, 4)	70.7	1.33	$0.572^{+0.094}_{-0.092}$	15.8	$+4.6$ -3.2	3.1	$+0.6$ -0.5	$+0.2$ -0.2	$+3.4$ 0.0

Table 10.1: π^-/π^+ production ratio and errors. Listed p_z and p_t are computed with π^+ spectrum.

Bin	p_z (GeV/c) p_t (GeV/c)		K^-/K^+	Errors in percent					
				Statistical	Total systematic	MC Correction	Trigger efficiency	Target out subtraction	Background modeling
(0, 0)	21.9	0.13	$0.602^{+0.123}_{-0.107}$	15.5	$+13.4$ -8.9	8.8	$+0.6$ -0.6	$+0.3$ -0.3	$+10.0$ 0.0
(0, 1)	21.9	0.30	$0.421^{+0.062}_{-0.052}$	11.1	$+9.8$ -5.5	5.5	$+0.3$ -0.3	$+0.3$ -0.2	$+8.1$ 0.0
(0, 2)	21.9	0.50	$0.445^{+0.069}_{-0.058}$	11.4	$+10.6$ -6.4	6.4	$+0.5$ -0.4	$+0.0$ -0.0	$+8.5$ 0.0
(0, 3)	22.0	0.74	$0.400^{+0.053}_{-0.052}$	10.5	$+8.0$ -7.8	7.7	$+0.3$ -0.7	$+0.1$ -0.1	$+2.1$ -1.0
(1, 0)	27.1	0.13	$0.491^{+0.090}_{-0.130}$	16.2	$+8.6$ -20.9	7.3	$+0.3$ -0.3	$+0.2$ -0.2	$+4.7$ -19.6
(1, 1)	27.1	0.30	$0.343^{+0.062}_{-0.047}$	12.0	$+13.3$ -6.5	6.4	$+0.7$ -0.7	$+0.3$ -0.3	$+11.6$ 0.0
(1, 2)	27.2	0.49	$0.382^{+0.058}_{-0.047}$	11.6	$+9.9$ -4.4	4.4	$+0.3$ -0.4	$+0.1$ -0.1	$+8.9$ 0.0
(1, 3)	27.3	0.75	$0.458^{+0.061}_{-0.055}$	10.3	$+8.6$ -6.4	6.3	$+0.8$ -0.8	$+0.2$ -0.2	$+5.7$ -0.0
(1, 4)	27.5	1.08	$0.483^{+0.150}_{-0.130}$	25.6	$+17.5$ -8.5	8.4	$+1.1$ -1.1	$+0.3$ -0.3	$+15.3$ 0.0
(2, 0)	35.6	0.13	$0.270^{+0.066}_{-0.077}$	21.2	$+12.2$ -18.8	11.5	$+2.9$ -2.6	$+0.2$ -0.2	$+2.7$ -14.7
(2, 1)	35.5	0.30	$0.267^{+0.078}_{-0.055}$	15.5	$+24.8$ -13.3	13.3	$+0.7$ -0.6	$+0.1$ -0.1	$+21.0$ -2.0
(2, 2)	35.6	0.50	$0.312^{+0.060}_{-0.052}$	14.4	$+12.9$ -8.6	8.5	$+0.7$ -0.8	$+0.2$ -0.2	$+9.7$ -0.9
(2, 3)	35.6	0.76	$0.346^{+0.076}_{-0.044}$	12.3	$+18.0$ -3.3	3.3	$+0.6$ -0.5	$+0.1$ -0.1	$+17.7$ 0.0
(2, 4)	36.0	1.19	$0.318^{+0.071}_{-0.073}$	21.3	$+6.4$ -8.1	5.9	$+2.4$ -2.2	$+0.0$ -0.0	$+0.0$ -5.0
(3, 0)	48.6	0.13	$0.083^{+0.035}_{-0.042}$	37.0	$+21.1$ -34.0	19.6	$+7.8$ -6.3	$+0.1$ -0.1	$+0.0$ -27.0
(3, 1)	48.9	0.30	$0.179^{+0.045}_{-0.055}$	23.3	$+10.2$ -19.7	10.0	$+1.2$ -1.0	$+0.8$ -0.6	$+0.6$ -16.9
(3, 2)	49.2	0.50	$0.186^{+0.045}_{-0.041}$	20.0	$+14.2$ -9.6	9.3	$+1.2$ -1.5	$+0.3$ -0.3	$+10.6$ -1.6
(3, 3)	48.8	0.76	$0.197^{+0.074}_{-0.047}$	20.9	$+31.2$ -11.8	11.0	$+0.5$ -0.4	$+0.1$ -0.1	$+29.2$ -4.3
(3, 4)	49.0	1.25	$0.370^{+0.095}_{-0.110}$	24.3	$+7.7$ -16.9	7.7	$+0.6$ -0.7	$+0.0$ -0.0	$+0.0$ -15.1
(4, 0)	69.6	0.13	< 0.069						
(4, 1)	69.1	0.30	$0.038^{+0.019}_{-0.023}$	48.6	$+13.6$ -35.4	13.0	$+3.9$ -3.2	$+0.5$ -0.5	$+0.0$ -32.8
(4, 2)	68.1	0.49	$0.061^{+0.027}_{-0.026}$	39.8	$+20.6$ -12.3	10.6	$+2.9$ -2.4	$+0.1$ -0.1	$+17.4$ -5.7
(4, 3)	68.8	0.77	$0.050^{+0.023}_{-0.024}$	44.3	$+9.2$ -19.3	9.1	$+0.3$ -0.3	$+0.9$ -1.0	$+0.0$ -17.0
(4, 4)	70.7	1.33	$0.245^{+0.095}_{-0.098}$	37.2	$+11.2$ -15.0	11.2	$+1.3$ -1.5	$+0.4$ -0.4	$+0.0$ -9.9

Table 10.2: K^-/K^+ production ratio and errors. Listed p_z and p_t are computed using π^+ spectrum.

Bin	p_z (GeV/c) p_t (GeV/c)		K^+/π^+	Errors in percent					
				Statistical	Total systematic	MC Correction	Trigger efficiency	Target out subtraction	Background modeling
(0, 0)	21.9	0.13	0.105 ^{+0.052} _{-0.018}	8.8	+48.3 -15.0	5.9	+0.8 -0.7	+0.3 -0.3	+48.0 -13.8
(0, 1)	21.9	0.30	0.114 ^{+0.051} _{-0.016}	6.1	+44.3 -12.8	6.0	+0.9 -0.8	+0.1 -0.1	+43.8 -11.3
(0, 2)	21.9	0.50	0.132 ^{+0.053} _{-0.020}	6.5	+39.9 -13.3	7.3	+0.3 -0.3	+0.0 -0.0	+39.3 -11.2
(0, 3)	22.0	0.74	0.207 ^{+0.091} _{-0.043}	6.1	+43.4 -20.0	7.2	+0.3 -0.3	+0.2 -0.2	+42.7 -18.6
(1, 0)	27.1	0.13	0.091 ^{+0.040} _{-0.010}	8.5	+43.4 -7.6	3.4	+1.8 -1.6	+0.0 -0.0	+43.2 -6.6
(1, 1)	27.1	0.30	0.128 ^{+0.049} _{-0.013}	6.1	+37.8 -7.8	5.6	+0.4 -0.4	+0.2 -0.2	+37.4 -5.4
(1, 2)	27.2	0.49	0.136 ^{+0.046} _{-0.012}	6.3	+33.1 -6.2	3.8	+1.2 -1.1	+0.0 -0.0	+32.8 -4.7
(1, 3)	27.3	0.75	0.188 ^{+0.063} _{-0.024}	6.1	+32.8 -11.0	6.2	+0.1 -0.1	+0.2 -0.2	+32.2 -9.2
(1, 4)	27.5	1.08	0.205 ^{+0.056} _{-0.046}	16.1	+21.8 -15.8	5.8	+0.1 -0.2	+0.0 -0.0	+21.0 -14.7
(2, 0)	35.6	0.13	0.129 ^{+0.028} _{-0.014}	9.5	+19.6 -4.8	2.5	+0.2 -0.3	+0.0 -0.0	+19.4 -4.1
(2, 1)	35.5	0.30	0.133 ^{+0.039} _{-0.010}	6.9	+28.6 -3.2	1.6	+0.6 -0.6	+0.1 -0.1	+28.6 -2.7
(2, 2)	35.6	0.50	0.155 ^{+0.045} _{-0.012}	7.1	+28.0 -3.1	2.4	+1.4 -1.3	+0.1 -0.0	+27.8 -1.6
(2, 3)	35.6	0.76	0.189 ^{+0.032} _{-0.017}	6.8	+15.7 -5.9	4.9	+0.7 -0.6	+0.1 -0.1	+14.9 -3.2
(2, 4)	36.0	1.19	0.249 ^{+0.075} _{-0.040}	12.4	+27.2 -10.2	6.0	+0.7 -0.7	+0.0 -0.0	+26.5 -8.2
(3, 0)	48.6	0.13	0.253 ^{+0.089} _{-0.031}	10.4	+33.5 -6.6	3.2	+3.1 -4.1	+0.1 -0.1	+33.2 -4.0
(3, 1)	48.9	0.30	0.143 ^{+0.042} _{-0.015}	8.7	+27.9 -5.5	4.3	+0.5 -0.4	+0.4 -0.4	+27.6 -3.4
(3, 2)	49.2	0.50	0.197 ^{+0.040} _{-0.018}	8.5	+18.3 -3.0	2.3	+0.8 -1.0	+0.0 -0.0	+18.1 -1.8
(3, 3)	48.8	0.76	0.153 ^{+0.039} _{-0.015}	9.0	+24.0 -3.1	1.9	+1.1 -0.9	+0.1 -0.1	+23.9 -2.2
(3, 4)	49.0	1.25	0.194 ^{+0.076} _{-0.032}	14.0	+36.4 -8.6	3.4	+0.6 -0.6	+0.1 -0.1	+36.2 -7.9
(4, 0)	69.6	0.13	0.178 ^{+0.091} _{-0.056}	17.9	+48.2 -25.9	10.8	+4.8 -6.2	+0.3 -0.3	+46.8 -22.7
(4, 1)	69.1	0.30	0.231 ^{+0.087} _{-0.034}	11.9	+35.5 -8.5	4.8	+1.5 -2.0	+0.1 -0.1	+35.1 -6.7
(4, 2)	68.1	0.49	0.256 ^{+0.056} _{-0.040}	12.9	+17.7 -8.9	3.6	+1.6 -1.9	+0.6 -0.6	+17.2 -7.8
(4, 3)	68.8	0.77	0.186 ^{+0.062} _{-0.028}	13.8	+30.6 -6.2	3.0	+0.9 -0.8	+0.1 -0.1	+30.4 -5.3
(4, 4)	70.7	1.33	0.196 ^{+0.086} _{-0.047}	20.2	+39.2 -12.7	5.0	+1.3 -1.2	+0.1 -0.1	+38.8 -11.6

Table 10.3: K^+/π^+ production ratio and errors. Listed p_z and p_t are computed with π^+ spectrum.

Bin	p_z (GeV/c) p_t (GeV/c)		K^-/π^-	Errors in percent					
				Statistical	Total systematic	MC Correction	Trigger efficiency	Target out subtraction	Background modeling
(0, 0)	21.9	0.13	$0.088^{+0.045}_{-0.015}$	13.7	$+49.6$ -10.1	9.4	$+1.1$ -1.0	$+0.3$ -0.3	$+48.7$ -3.4
(0, 1)	21.9	0.30	$0.077^{+0.040}_{-0.012}$	10.1	$+50.7$ -12.0	9.2	$+0.5$ -0.6	$+0.3$ -0.2	$+49.8$ -7.8
(0, 2)	21.9	0.50	$0.089^{+0.043}_{-0.016}$	10.2	$+47.6$ -14.2	10.9	$+0.0$ -0.0	$+0.0$ -0.0	$+46.3$ -9.2
(0, 3)	22.0	0.74	$0.112^{+0.051}_{-0.026}$	9.6	$+44.6$ -21.3	12.3	$+0.1$ -0.1	$+0.0$ -0.0	$+42.9$ -17.5
(1, 0)	27.1	0.13	$0.086^{+0.025}_{-0.013}$	14.6	$+25.6$ -5.1	4.9	$+0.4$ -0.4	$+0.1$ -0.1	$+25.1$ -1.4
(1, 1)	27.1	0.30	$0.077^{+0.038}_{-0.011}$	11.0	$+47.3$ -8.6	7.6	$+0.3$ -0.3	$+0.2$ -0.2	$+46.7$ -4.0
(1, 2)	27.2	0.49	$0.087^{+0.037}_{-0.011}$	10.5	$+41.0$ -7.0	6.2	$+0.2$ -0.2	$+0.1$ -0.1	$+40.5$ -3.3
(1, 3)	27.3	0.75	$0.113^{+0.045}_{-0.018}$	9.2	$+38.9$ -12.7	8.1	$+0.4$ -0.4	$+0.1$ -0.1	$+38.0$ -9.8
(1, 4)	27.5	1.08	$0.147^{+0.060}_{-0.043}$	23.1	$+33.7$ -17.9	8.4	$+0.5$ -0.5	$+0.4$ -0.4	$+32.7$ -15.7
(2, 0)	35.6	0.13	$0.079^{+0.018}_{-0.017}$	20.0	$+9.7$ -8.7	8.3	$+2.5$ -2.2	$+0.2$ -0.2	$+4.3$ -1.1
(2, 1)	35.5	0.30	$0.074^{+0.036}_{-0.013}$	14.5	$+46.8$ -11.1	10.8	$+0.6$ -0.5	$+0.1$ -0.1	$+45.5$ -2.4
(2, 2)	35.6	0.50	$0.084^{+0.033}_{-0.013}$	13.3	$+36.7$ -7.2	6.9	$+0.2$ -0.2	$+0.2$ -0.2	$+36.0$ -2.2
(2, 3)	35.6	0.76	$0.104^{+0.035}_{-0.013}$	11.2	$+31.8$ -5.1	4.2	$+0.1$ -0.1	$+0.1$ -0.1	$+31.6$ -2.8
(2, 4)	36.0	1.19	$0.107^{+0.037}_{-0.025}$	19.7	$+28.2$ -13.3	5.4	$+0.7$ -0.6	$+0.0$ -0.0	$+27.6$ -12.2
(3, 0)	48.6	0.13	$0.045^{+0.019}_{-0.018}$	36.6	$+18.5$ -17.2	16.6	$+2.0$ -1.8	$+0.1$ -0.1	$+7.8$ -4.1
(3, 1)	48.9	0.30	$0.058^{+0.015}_{-0.013}$	22.5	$+11.4$ -5.4	4.9	$+0.4$ -0.3	$+0.2$ -0.1	$+10.3$ -2.3
(3, 2)	49.2	0.50	$0.083^{+0.029}_{-0.017}$	19.2	$+28.8$ -7.9	6.8	$+2.5$ -2.9	$+0.3$ -0.3	$+27.8$ -2.8
(3, 3)	48.8	0.76	$0.059^{+0.032}_{-0.013}$	19.8	$+50.1$ -10.2	8.1	$+0.1$ -0.1	$+0.1$ -0.1	$+49.4$ -6.1
(3, 4)	49.0	1.25	$0.106^{+0.037}_{-0.028}$	22.3	$+26.6$ -13.2	5.7	$+0.2$ -0.2	$+0.1$ -0.1	$+25.9$ -11.9
(4, 0)	69.6	0.13	< 0.026						
(4, 1)	69.1	0.30	$0.020^{+0.010}_{-0.010}$	48.3	$+15.7$ -16.3	14.3	$+3.3$ -2.7	$+0.3$ -0.3	$+5.6$ -7.4
(4, 2)	68.1	0.49	$0.047^{+0.027}_{-0.021}$	39.8	$+40.0$ -17.5	11.2	$+1.1$ -1.0	$+0.3$ -0.3	$+38.4$ -13.4
(4, 3)	68.8	0.77	$0.023^{+0.011}_{-0.011}$	43.6	$+17.8$ -16.2	10.8	$+0.4$ -0.3	$+1.1$ -1.2	$+14.1$ -12.0
(4, 4)	70.7	1.33	$0.084^{+0.043}_{-0.036}$	35.0	$+36.9$ -24.0	10.6	$+0.6$ -0.7	$+0.1$ -0.1	$+35.4$ -21.5

Table 10.4: K^-/π^- production ratio and errors. Listed p_z and p_t are computed with π^+ spectrum.

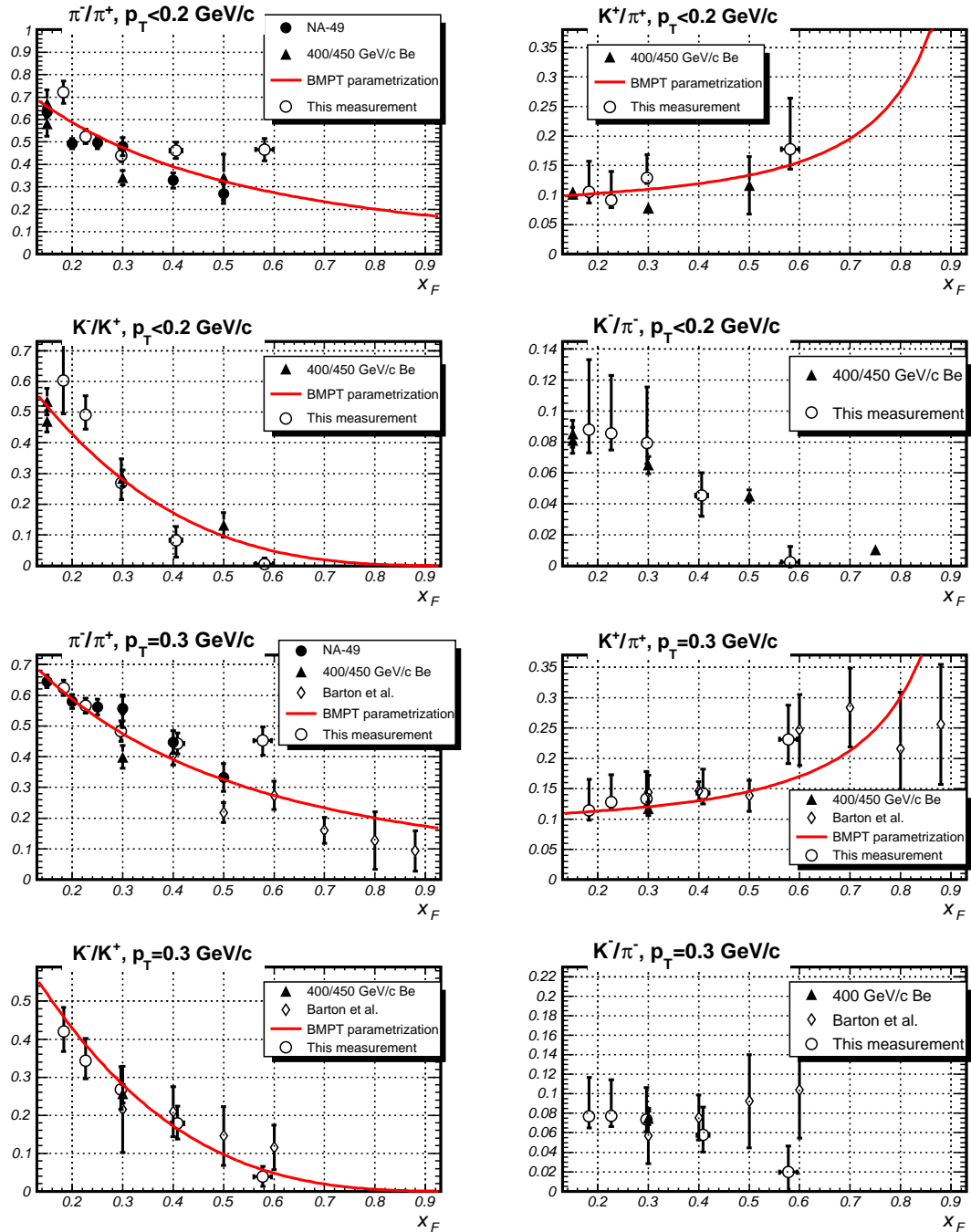


Figure 10.2: Comparison to existing measurements and parametrization of beryllium data.

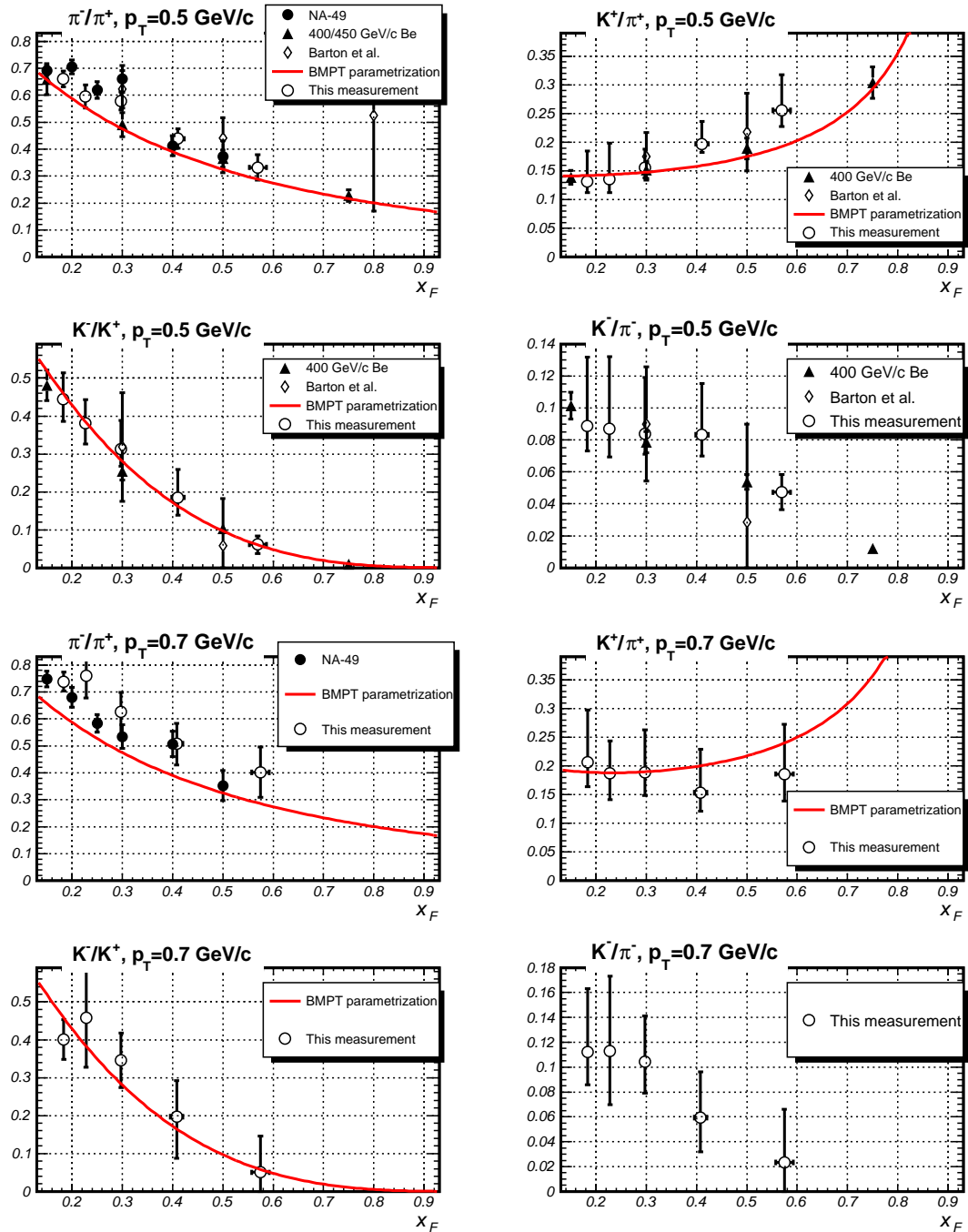


Figure 10.3: Comparison to existing measurements and parametrization of beryllium data.

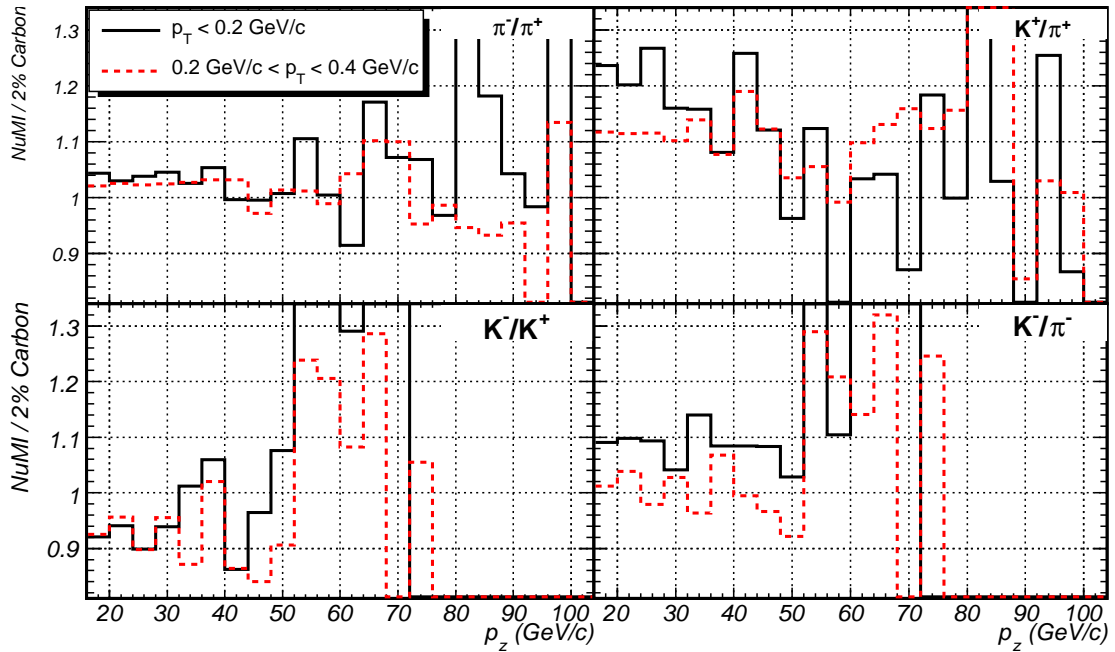


Figure 10.4: Comparison of the ratios on the NuMI target and the 2% target. The NuMI ratios are generated with FLUKA-05, 2% ratios are generated with FLUKA-06.

10.3 Comparison to MINOS Measurements

It is interesting to compare this measurement to the particle production ratios on the NuMI target. Figure 10.4 shows that the thin target ratios and NuMI target ratios predicted by FLUKA are similar to about 10%. This is expected as production of particle at high momenta is dominated by interactions of primary protons with carbon.

MINOS beam systematics group takes advantage of the fact that the MINOS neutrino flux spectrum can be changed significantly by varying the target position with respect to the two focusing horns and the horn currents.[29, 17] Variation of target position with respect to the horns changes longitudinal momentum of focused hadrons and variation of horn currents changes their transverse momentum. The near detector has large neutrino rate, allowing the group to “effectively map out particle production in (x_F, p_T) ” [29].

The ratios derived from the fitted MINOS hadronic spectrum nicely compare to the measurement presented here (see Figure 10.5).

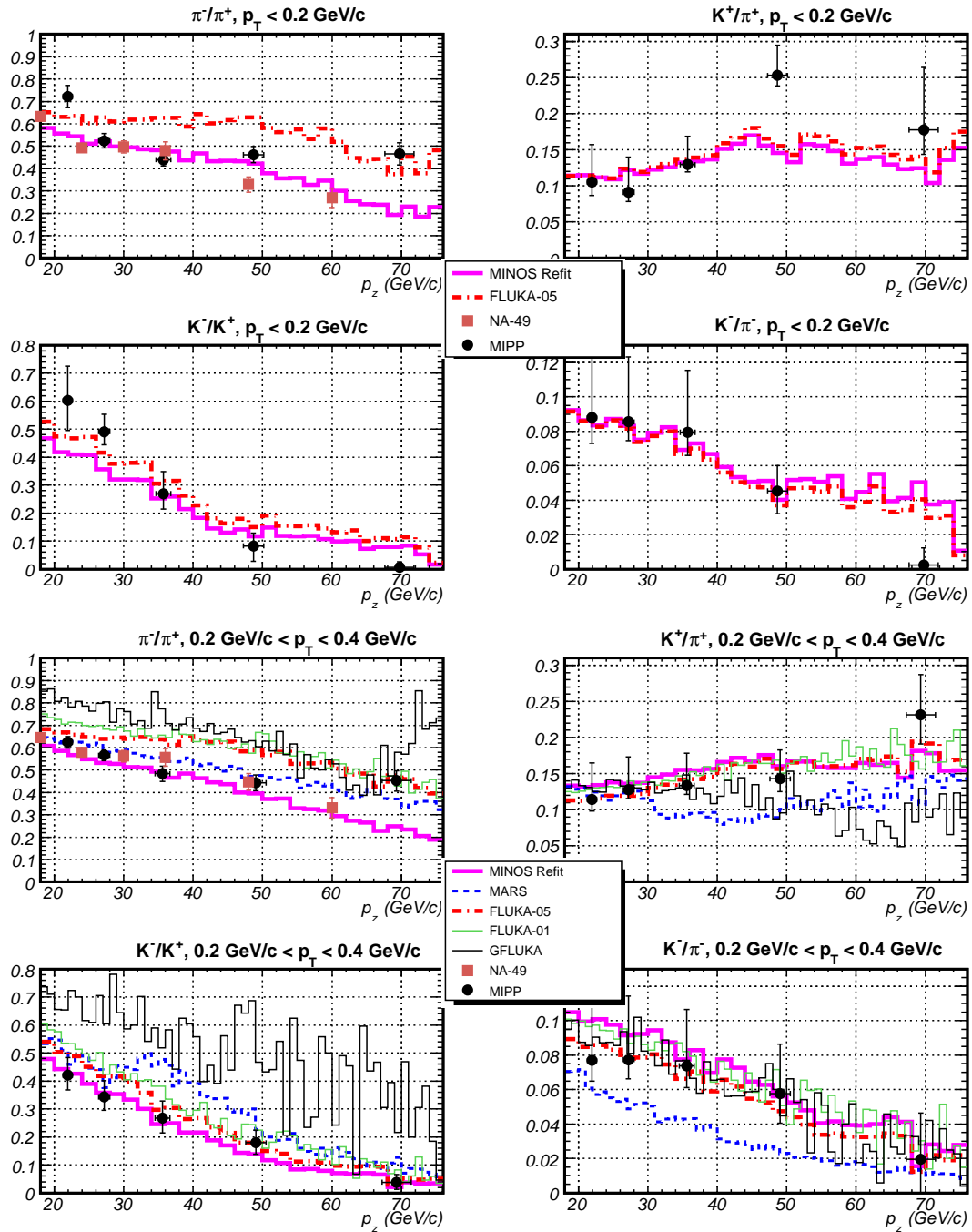


Figure 10.5: Comparison to various Monte Carlo models and MINOS fitted ratios. The Monte Carlo and fitted ratios have been generated with the MINOS target, while the measured ratios come from the thin target data. For models other than FLUKA-05 and MINOS, the ratios are computed for $p_T < 1$ GeV/c only, so they are compared to the bins which have the largest statistics in p_T .

10.4 Discussion and Outlook

We presented the first measurement using the data from the MIPP spectrometer. The precision of the measurement is generally limited by statistics, although at this time our understanding of the background is limited and is a significant source of systematic error, especially for kaons. Better modeling of the RICH response in the Monte Carlo simulation will certainly reduce the systematic errors associated with the measurement.

The measurement is consistent with previously published data, except in the highest momentum bin where we (apparently) find too few π^+ . The bins with high p_z have smaller pion and kaon statistics, therefore good knowledge of background is required to interpret the data correctly. Good agreement is also found between the ratios presented here and the ratios derived from the fitted MINOS pion and kaon spectra.

We do find inconsistencies with the FLUKA-06 Monte Carlo spectrum, especially in the π^-/π^+ ratio. Addressing these discrepancies between the model and existing data will be extremely valuable for present and future neutrino experiments.

Bibliography

- [1] H. W. Atherton et al. Precise measurements of particle production by 400-gev/c protons on beryllium targets. 1980. CERN-80-07.
- [2] D. S. Barton et al. Experimental study of the A-dependence of inclusive hadron fragmentation. *Phys. Rev.*, D27:2580–2599, 1983.
- [3] Gerard Beekmans. *Linux From Scratch Version 4.0-RC1*. Linux From Scratch Project, 2002.
- [4] Fred Bieser, Ron Jones, , and Charles McFarland. Data links for the EOS TPC. *IEEE Trans. Nucl. Sc.*, **38**:335–336, 1991.
- [5] W. Blum and L. Rolandi. *Particle detection with drift chambers*. Springer-Verlag, 1994.
- [6] M. Bonesini, A. Marchionni, F. Pietropaolo, and T. Tabarelli de Fatis. On particle production for high energy neutrino beams. *Eur. Phys. J.*, C20:13–27, 2001.
- [7] C. Bower, N. Graf, M. D. Messier, and J. Paley. The Indiana trigger counter. *MIPP Note*, **55**, 2005.
- [8] R. A. Burnstein et al. HyperCP: A high-rate spectrometer for the study of charged hyperon and kaon decays. *Nucl. Instrum. Meth.*, A541:516–565, 2005.
- [9] M. G. Catanesi et al. Proposal for hadron production measurements using the NA49 detector for use in long-baseline and atmospheric neutrino flux calculations. 2001. CERN-SPSC-2001-017.
- [10] CERN, Geneva, Switzerland. *GEANT – Detector Description and Simulation Tool*, 1993.
- [11] D. C. Christian et al. High rate drift chambers. *Nucl. Instrum. Meth.*, A345:62–71, 1994.
- [12] SPY Collaboration. *Eur. Phys. J. C*, 10:605, 1999.
- [13] Creative Electronic Systems S.A. *CBD 8210 CAMAC Branch Driver*, July 1996.
- [14] M. De Palma et al. A system of large multiwire proportional chambers for a high intensity experiment. *Nucl. Instr. Meth.*, 217:135, 1983.

-
- [15] W.N. English and G.C. Hanna. *Canadian Journal of Physics*, 31:768, 1953.
- [16] C. Alt et al. Inclusive production of charged pions in p+C collisions at 158GeV/c beam momentum. *arXiv:hep-ex/0606028*, 2006.
- [17] D. G. Michael et al. Observation of muon neutrino disappearance with the MINOS detector in the NuMI neutrino beam. *Phys. Rev. Lett.*, 97, 2006.
- [18] G. Rai et al. A TPC detector for the study of high multiplicity heavy ion collisions. *IEEE Trans. Nucl. Sc.*, **37**:56–64, 1990.
- [19] H. Wieman et al. A TPC detector for the study of high multiplicity heavy ion collisions. *Nucl. Phys.*, **A525**:617–620, 1991.
- [20] J. Engelfried et al. The E781 (SELEX) RICH detector. *Nucl. Inst. and Meth.*, **A409**:439–442, 1998.
- [21] J. Engelfried et al. The RICH detector of the SELEX experiment. *Nucl. Inst. and Meth.*, **A433**:149–152, 1999.
- [22] J. Engelfried et al. The SELEX phototube RICH detector. *Nucl. Inst. and Meth.*, **A431**:53–69, 1999.
- [23] K. L. Lee et al. Analog-to-digital conversion using custom CMOS analog memory for the EOS time projection chamber. *IEEE Trans. Nucl. Sc.*, **38**:344–347, 1991.
- [24] A. Fasso', A. Ferrari, J. Ranft, and P.R. Sala. FLUKA: a multi-particle transport code. *CERN 2005-10, INFN/TC_05/11, SLAC-R-773*, 2005.
- [25] A. Fasso', A. Ferrari, S. Roesler, P.R. Sala, G. Battistoni, F. Cerutti, E. Gadioli, M.V. Garzelli, F. Ballarini, A. Ottolenghi, A. Empl, and J. Ranft. The physics models of FLUKA: status and recent developments. *Computing in High Energy and Nuclear Physics Conference*, 2003.
- [26] Y. Fukuda et al. Evidence for oscillation of atmospheric neutrinos. *Phys. Rev. Lett.*, 81:1562–1567, 1998.
- [27] <http://www.linuxfromscratch.org>.
- [28] Stuart A. Kleinfelder. A 4096 cell switched capacitor analog waveform storage integrated circuit. *IEEE Trans. Nucl. Sc.*, **37**:1230–1236, 1990.
- [29] Sacha Kopp, Žarko Pavlović, Patricia Vahle, and Rustem Ospanov. Constraining the beam neutrino mc flux using the minos nd data. minos-doc-2965, April 2007.
- [30] A. Lebedev. Chamber tuning and alignment. *MIPP Note*, 129, 2007.
- [31] Valeri Lebedev. <http://fnal.gov/optim>.

- [32] J. B. Lindsay, C. Millerin, J. C. Tarlé, H. Verveij, and H. Wendler. A fast and flexible data acquisition system for multiwire proportional chambers and other detectors. *Nucl. Inst. and Meth.*, **156**:329–333, 1978.
- [33] MINER ν A Collaboration. The MINER ν A technical design report, 2006.
- [34] The MiniBooNE collaboration. A search for electron neutrino appearance at the $\delta m^2 \sim 1 \text{ eV}^2$ scale. *arXiv:hep-ex/0704.1500*, 2007.
- [35] N. Mokhov. MARS code system. <http://www-ap.fnal.gov/MARS/>.
- [36] M. Nakamura, D.A. Landis, and G. Rai. Low power shaper amplifier for the EOS TPC detector. *IEEE Trans. Nucl. Sc.*, **38**:50–52, 1991.
- [37] J. Paley, R. Soltz, P.D. Barnes, M. Heffner, J. Klay, and D. Miller. MIPP TPC reconstruction. *MIPP Note*, 129, 2006.
- [38] Anna Peisert and Fabio Sauli. Drift and diffusion of electrons in gases: a compilation. Technical Report 84-08, CERN, July 1984.
- [39] S.F.Biagi. Magboltz 2. <http://ref.web.cern.ch/ref/CERN/CNL/2000/001/magboltz>.
- [40] S.F.Biagi. Monte Carlo simulation of electron drift and diffusion in counting gases under the influence of electric and magnetic fields. *Nucl. Inst. and Meth.*, A421:234–240, 199.
- [41] Ron Soltz. Private communication.
- [42] M. Starič and P. Krizan. An iterative method for the analysis of Cherenkov rings in the HERA-B RICH. *Nucl. Inst. and Meth.*, A 433:279–285, 1999.
- [43] H. Wieman and the EOS Collaboration. Heavy ion reaction measurements with the EOS TPC (looking for central collisions with missing energy). In *Proceedings of the Tenth Winter Workshop on Nuclear Dynamics (Snowbird, Utah)*, January 14-21, 1994.
- [44] Xihong Yang. *Centrality dependence of strangeness production in proton-nucleus collisions at AGS energies*. PhD thesis, Columbia University, 2000.